ELECTRIC FIELD DEPENDENT OPTOELECTRONIC NATURE OF InGaN/GaN QUANTUM STRUCTURES AND DEVICES

A THESIS
SUBMITTED TO THE DEPARTMENT OF ELECTRICAL AND ELECTRONICS ENGINEERING
AND THE GRADUATE SCHOOL OF ENGINEERING AND SCIENCE
OF BILKENT UNIVERSITY
IN PARTIAL FULLFILMENT OF THE REQUIREMENTS
FOR THE DEGREE OF
DOCTOR OF PHILIOSOPHY

By
Emre Sarı
December 2012

I certify that I have read this thesis and that in my opinion it is fully adequate, in scope and in quality, as a thesis for the degree of Doctor of Philosophy.

_____

Assoc. Prof. Hilmi Volkan Demir (Supervisor)

I certify that I have read this thesis and that in my opinion it is fully adequate, in scope and in quality, as a thesis for the degree of Doctor of Philosophy.

_____

Prof. Ömer Morgül

I certify that I have read this thesis and that in my opinion it is fully adequate, in scope and in quality, as a thesis for the degree of Doctor of Philosophy.

_____

Assist. Prof. Ali Kemal Okyay

I certify that I have read this thesis and that in my opinion it is fully adequate, in scope and in quality, as a thesis for the degree of Doctor of Philosophy.

_____

Assoc. Prof. Dönüş Tuncel

I certify that I have read this thesis and that in my opinion it is fully adequate, in scope and in quality, as a thesis for the degree of Doctor of Philosophy.

_____

Assoc. Prof. Hamza Kurt

Approved for the Graduate School of Engineering and Science:

_____

Prof. Levent Onural

Director of Graduate School of Engineering and Science

ABSTRACT

ELECTRIC FIELD DEPENDENT OPTOELECTRONIC NATURE OF InGaN/GaN QUANTUM STRUCTURES AND DEVICES

Emre Sarı
Ph.D. in Electrical and Electronics Engineering
Supervisor: Assoc. Prof. Hilmi Volkan Demir

December 2012

In the past two decades we have been witnessing the emergence and rapid development of III-Nitride based optoelectronic devices including InGaN/GaN light-emitting diodes (LEDs) and laser diodes with operation wavelengths ranging from green-blue to near-UV. These InGaN/GaN devices are now being widely used in applications important for lighting, displays, and data storage, collectively exceeding a total market size of 10 billion USD. Although InGaN/GaN has been studied and exploited very extensively to date, its field dependent nature is mostly unknown and is surprisingly prone to quite unexpected behavior due to its intrinsic polarization property. In this thesis, we report our systematic study on the electric field dependent characteristics of InGaN/GaN quantum structures and devices including modulators and LEDs. Here we present our comparative study of electroabsorption in polar c-plane InGaN/GaN multiple quantum wells (MQWs) with different built-in polarization induced electrostatic fields. Analyzing modulator structures with varying structural MQW parameters, we find that electroabsorption grows stronger with decreasing built-in electrostatic field strength inside the well layer, as predicted by our theoretical model and verified by our experimental results. To further explore the field dependent optoelectronic nature of c-plane grown InGaN/GaN quantum structures, we investigate radiative carrier dynamics, which is of critical importance for LEDs. Our time and spectrum resolved

photoluminescence measurements and numerical analyses indicate that the carrier lifetimes, the radiative recombination lifetimes, and the quantum efficiencies all decrease with increasing field. We also study the physics of electroabsorption and carrier dynamics in InGaN/GaN quantum heterostructures grown intentionally on nonpolar a-plane of the wurtzite crystal structure, which are free of the polarization-induced electrostatic fields. We compare these results with the conventional c-plane grown polar structures. In the polar case, we observe blue-shifting absorption profile and decreasing carrier lifetimes with increasing electric field. In the nonpolar case, however, we observe completely the opposite: a red-shifting absorption profile and increasing carrier lifetimes. We explain these observations in the context of basic physical principles including Fermi's golden rule and quantum-confined Stark effect. Also, we present electroabsorption behavior of InGaN/GaN quantum structures grown using epitaxial lateral overgrowth (ELOG) in correlation with their dislocation density levels and in comparison to steady state and time-resolved photoluminescence measurements. The results reveal that ELOG structures with decreasing mask stripe widths exhibit stronger electroabsorption performance. While keeping the ELOG window widths constant, compared to photoluminescence behavior, however, electroabsorption surprisingly exhibits the largest performance variation, making the electroabsorption the most sensitive to the mask stripe widths. This thesis work provides significant insight and important information for the optoelectronics of InGaN/GaN quantum structures and devices to better understand their field dependent nature.

Keywords: Optoelectronics, III-Nitrides, semiconductors, modulators, LEDs.

ÖZET

InGaN/GaN KUVANTUM YAPILARININ VE AYGITLARININ ELEKTRİK ALANA BAĞLI OPTOELEKTRONİK DOĞASI

Emre Sarı
Elektrik ve Elektronik Mühendisliği Bölümü Doktora
Tez Yöneticisi: Doç. Dr. Hilmi Volkan Demir
Aralık 2012

Geride bıraktığımız 20 yılda, çalışma dalgaboyları yeşilden yakın morötesine değişen InGaN/GaN tabanlı ışık yayan diyotlar (LED'ler) ve lazer diyotlar gibi III-Nitrür tabanlı optelektronik aygıtların ortaya çıkışına ve hızlı bir şekilde gelişimine şahit olduk. Bu InGaN/GaN tabanlı aygıtlar artık görüntü, veri saklama ve aydınlatma gibi birçok alan için önem arz ediyor ve toplamda 10 milyar Amerikan dolarının üzerinde bir pazar büyüklüğü oluşturuyor. Bu InGaN/GaN yapıları şimdiye kadar yoğun olarak araştırılmış ve incelenmiş olsa da elektrik alana bağlı doğası çoğunlukla bilinmemektedir; kendinden kutuplu olma özelliği sebebiyle beklenmeyen davranışlar göstermeye eğilimlidir. Bu tez çalışmasında InGaN/GaN kuvantum yapılarının ve bunları içeren kipleyici ve LED gibi aygıtların elektrik alana bağlı özelliklerini incelediğimiz sistematik çalışmalarımızı sunmaktayız. Farklı yapısal özelliklere sahip çoklu kuvantum kuyusu (MQW) içeren kipleyici yapılarını inceleyerek, teorik modelimizle ve deneysel sonuçlarımızla uyumlu şekide, kendinden polarizasyon sebepli elektrik alan şiddeti azaldıkça elektrosoğrulmanın güçlendiğini bulduk. c-düzlemine büyütülmüş InGaN/GaN kuvantum yapılarının elektrik alana bağlı optoelektronik doğasını daha derinlemesine incelemek için LED'ler için kritik önem arz eden ışınımsal taşıyıcı dinamiğini inceledik. Zaman ve tayf çözünümlü fotoışıma ölçümlerimiz ve sayısal analizlerimiz taşıyıcı ömürlerinin, ışınımsal

taşıyıcı ömürlerinin ve kuvantum verimliliklerinin hepsinin artan elektrik alan ile azaldığını gösterdi. Ayrıca wurtzite kristal yapısının polarizasyon sebepli elektrik alan içermeyen, polar olmayan, a-düzlemine büyütülen InGaN/GaN kuvantum yapılarının elektrosoğrulma ve taşıyıcı dinamiği ile ilgili fiziğini çalıştık. Buradan elde ettiğimiz sonuçları geleneksel olarak kullanılan c-düzlemine büyütülen polar yapılarla karşılaştırdık. Polar durumda artan elektrik alan ile maviye kayan soğrulma profili ve azalan taşıyıcı ömrü gözlemledik. Polar olmayan durumda, öte yandan, tamamen tersi olduğunu gösterdik: kırmızıya kayan soğrulma profili ve artan taşıyıcı ömürlerini bulduk. Bu gözlemlerimizi Fermi'nin altın kuralı ve kuvantum-kısıtlamalı Stark etkisi gibi temel fiziksel prensiplerle açıkladık. Ayrıca epitaksiyel yatay üst-büyütme (ELOG) tekniği kullanılarak dislokasyon yoğunluğu ile bağıntılı olarak InGaN/GaN kuvantum yapılarının elektrosoğrulma davranışını inceledik ve sabit hal ve zaman çözünürlüklü fotoışıma ölçümleriyle karşlaştırdık. Sonuçlarımız ELOG maske çizgi genişliğinin azalmasıyla elektrosoğrulmanın güçlendiğini gösterdi. ELOG pencere genişliğini sabit tutarken elektrosoğrulma performansı, ilginç bir biçimde, fotoışıma performansına göre daha çok değişim gösterip, elektrosoğrulmayı maske çizgi genişliğine daha hassas hale getirdi. Bu tez, InGaN/GaN kuvantum yapılarının ve aygıtlarının optoelekroniğinin, elektrik alana bağlı doğasını daha iyi anlaşılması için önemli içgörü ve önemli bilgi içermektedir.

Anahtar Kelimeler: Optoelektronik, III-Nitrürler, yarıiletkenler, kipleyiciler, LED’ler.

Acknowledgements

I would like to take this opportunity to express my gratitude to Prof. Hilmi Volkan Demir, my supervisor and mentor, whose support, motivation and guidance made this thesis work along with other great things possible.

I would like to thank my committee members Prof. Ömer Morgül, Prof. Ali Kemal Okyay, Prof. Dönüş Tuncel and Prof. Hamza Kurt for accepting to be in my thesis jury.

I would like to thank TUBITAK BIDEB for their support from 2211 and 2214 programs.

Last but not the least; I would like to thank my friends and family for always being there especially to my wife, Serpil, whose support and endurance has been the inspiration to finalize this thesis. This thesis is dedicated to her…

Table of Contents

List of Figures

Chapter 1

Introduction

Electronic devices based on silicon microelectronics technology have revolutionized the world we live in. Personal computers, and later mobile communication devices, including tablet computers and smart phones have made a significant impact on our lives. These tools are now much more capable compared to the past, thanks to ever-improving complementary metal-oxide-semiconductor (CMOS) microchip technology based on silicon. As a natural result, the size of electronics market and that of related areas such as telecommunication and information technology have constantly evolved and expanded. Related products and services have become more accessible especially in the last decade since the beginning of the 21st century.

In a similar way, we have been witnessing the emergence, increased interest of research and development, as well as the commercialization and wide usage of optoelectronic devices based on GaN in the same time interval **[1]**. Among those optoelectronic devices, light-emitting diodes (LEDs) with emission wavelengths varying from blue/green to ultraviolet (UV), and laser diodes (LDs) operating in blue and near-UV have achieved the biggest success. Today, we widely use LEDs

for liquid crystal display backlighting as well as traffic signs and white light sources. With the Blu-ray disc technology which utilizes GaN based blue LDs, we can now store more than 100 GB of information into a 12 cm diameter disc.

Among GaN based optoelectronic devices demonstrated thus far, LEDs have achieved the widest usage so far, and are expected to have the most impact, among III-Nitride devices, especially through high efficiency solid state lighting. Currently, lighting consumes more than 20% of electricity produced in the world. US Department of Energy estimates that about US$ 100 Billion saving in energy can be realized by 2020, using 200 lm/W solid-state light sources (which are 20-50 times more efficient than incandescent light sources and 3-4 times more efficient than compact fluorescent lamps) for general lighting **[2]**. More importantly, a vast amount of reduction in carbon emission, many hundreds of million tons per year, can be achieved. Today, in the market, there are products with 165 lm/W luminous efficacies, and R&D records have exceeded 250 lm/W **[3]**. Companies and research institutions are continuing to push the limits of the device performances while reducing the costs associated with the technology.

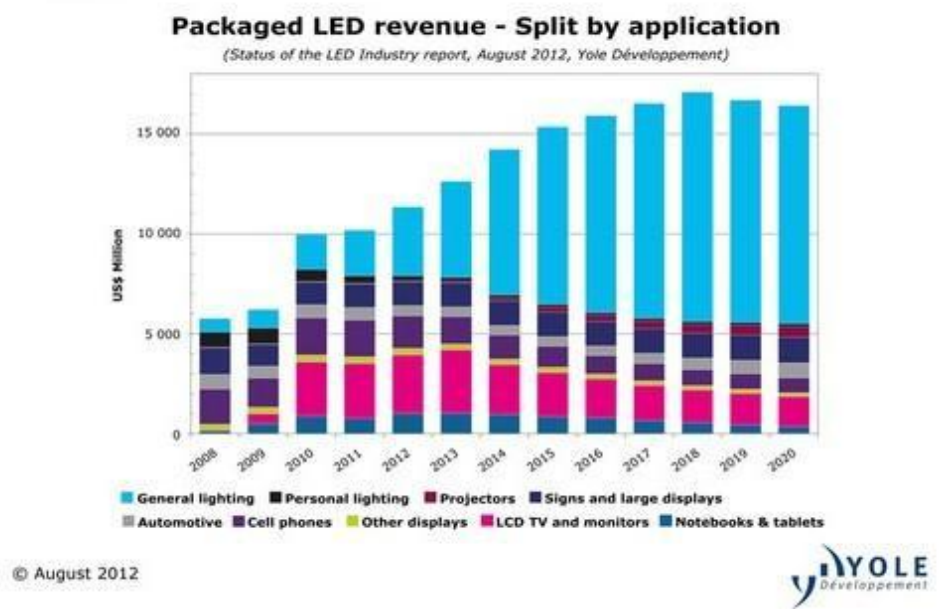

Figure 1. 1 Packaged LED revenues for different applications: Years 2008-2020. Note that the general lighting application is expected to dominate the market. After [4].

Not surprisingly, the economic opportunities are enormous. The overall packaged LED market today is US$ 12 Billion, projected to be US$ 17 Billion by 2018 as shown in Figure 2.1. Although today the market is driven by the demand from the LCD display and general lighting segments equally (comprising more than 50% of the revenues), the general lighting segment is expected to dominate the LED market with its US$ 10 Billion projected share by the year 2018 **[4]**.

Our group has been active in this device platform and contributed to hybrid LED research for high quality lighting in the last 6 years **[5]–[9]**.

This thesis work is on InGaN/GaN quantum structures and devices that house them. In this thesis work, we present our studies on understanding the underpinning physics and improving the performances of electroabsorption modulators and LEDs. We study electroabsorption and electric field dependent carrier dynamics in epitaxial lateral overgrown (ELOG) and conventional polar c-plane structures and nonpolar structures. Furthermore, we present our results on the reduction of droop (the decrease of LED efficiency at high currents) in LEDs through multiple quantum well (MQW) to electron blocking layer (EBL) distance optimization.

In Chapter 2, we present a background on III-Nitride material platform its physical properties, history, and plausible future. We provide information on the crystal structures of III-Nitrides and explicate the polarization effects in their quantum structures, which cause built-in electrostatic fields in quantum well and barrier layers in opposite directions. We continue the background on III-Nitrides by explaining semi polar and nonpolar growth planes which have reduced or zero polarization fields in their quantum heterostructures. Then we explain the widely used growth method for III-Nitrides, metal organic chemical vapor deposition (MOCVD). We also build a background on optoelectronic device physics and through InGaN/GaN based optoelectronic devices demonstrated in the past; we exploit this exciting material and device platform through addressing the issues and gaps in this platform.

In Chapter 3, we present our eptaxial lateral overgrown InGaN/GaN quantum structures and our results on dislocation density dependent electroabsorption. In this work, we study three ELOG samples with different ELOG patterns and a reference sample with no ELOG pattern. Our results deduced from independent experiments (time and spectrum resolved photoluminescence, dislocation density measurements through etch pit formation and electroabsorption) are consistent with each other. Especially, EA performance was superior in the structure with the lowest dislocation density. Also, EA performance was found to be much more sensitive to changes in dislocation densities compared to steady-state PL performance.

In Chapter 4, we present electroabsorption modulators comprising InGaN/GaN quantum structures with different quantum well and barrier thicknesses and materials to study the effect of polarization-induced built-in electrostatic field intensity in the well layers ($\mathbf{E_{well}}$) on the electroabsorption performance. We study three modulator devices with different MQW parameters and thus three different $\mathbf{E_{well}}$ values. Our results show that the best performing device has the lowest built-in electrostatic field intensity inside the well layers ($\mathbf{E_{well}}$). In Chapter 4, we also present the opposite electroabsorption behavior of polar and nonpolar InGaN/GaN quantum structures, with and without polarization induced electrostatic fields in their quantum structures along their growth directions, respectively. We show that c-plane grown polar structures exhibit a blue shifting profile whereas the a-plane grown nonpolar structures exhibit a red shifting absorption profile, quantum-confined Stark effect in the conventional way as in other III-V quantum structures which are free from polarization effects.

We start Chapter 5 by presenting radiative decay kinetics of polar InGaN/GaN quantum structures obtained by spectrum and time resolved PL measurements. We show that quantum efficiency, carrier lifetime and radiative recombination lifetime decrease with increasing external electric field. Furthermore, we present carrier dynamics in polar and nonpolar structures which also behave oppositely.

Our results in this chapter are explained in consistency with Fermi's golden rule and quantum-confined Stark effect.

Finally in Chapter 6, we present our electron blocking layer (EBL) design and its distance optimization to multiple quantum well (MQW) layers for reduced droop. We examine electron and hole concentrations at different parts of the structure to optimize the MQW-to-EBL distance and show that droop reduction is possible through this optimization.

Chapter 2

Background

In this chapter, we provide a background for the rest of the thesis. We start with a short history of III-Nitride materials platform; we provide an outlook for the future of it. We continue with the physical properties with an emphasis on those which are related with the scope of this thesis. These include the crystal structure, polarization effects, non-conventional growth planes and their growth using metal-organic chemical vapor deposition (MOCVD). We continue with basic semiconductor device physics to provide a background on optoelectronic devices. We explain optical processes in semiconductrors, introduce some important definitions, such as carrier lifetimes and quantum efficiency, for our understanding of device performance and operations. We further explain some of the important mechanisms, such as Franz Keldysh effect and quantum-confined Stark effect. We introduce absorption coefficient, again for our understanding of device performance and operation. Also, we briefly introduce APSYS computational tool that we used for our LED simulations. In the next part of this chapter, we review some of the research that has been pursued in III-Nitride optoelectronic device platform. We address the studies that are important for the scope of this thesis, specifically on electroabsorption modulators and LEDs. We explain some of the challenges faced in this platform. We complete this background chapter by conclusions.

2.1 III-Nitrides Background

In this part we give a background on III-Nitrides in a materials perspective: we briefly present their history, address some fundamental physical properties, explain their growth using MOCVD, and their applications with an emphasis on optoelectronic devices.

2.1.1 Short history of III-Nitrides

Since the first successful demonstration of blue light-emitting diode by Nakamura in 1993 **[10]**, there has been a strong and increasing scientific and technological interest in III-Nitride material platform. The research towards achieving III-Nitride based LEDs was pursued at a very small number of institutions at that time mainly due to difficulties to grow these materials **[1]**. The two obstacles that previously hindered researchers to demonstrate blue LEDs were: the growth of high quality GaN films and their p-doping **[1]**. In 1986, Asaki and coworkers showed that it is possible to grow high crystalline quality GaN on sapphire substrates using MOCVD by performing the buffer layer growths at different temperatures **[11]**. By first growing a thin layer of AlN buffer layer at relatively lower temperatures and eventually increasing to higher temperatures, they were able to achieve high crystal quality GaN films on sapphire, despite the relatively high lattice constant mismatch between GaN and sapphire (~15%). According to their description of the buffer layer approach depicted in Figure 2.2, which is still found to be valid, nanoislands of GaN (or AlN) first nucleate on the sapphire substrate (called nucleation layer), and then the nuclei grow in three dimensions until they are sufficiently dense (faulted zone). After the 3D growth, the growth mode is switched to 2D and the material grown on each nucleus coalesce (semi-sound zone). While this coalescence eliminates further vertical propagation of the defects by terminating them laterally, still some of those defects propagate vertically (sound zone). The optimization of the whole buffer layer growth process is very important for device purposes. Typical thickness of the total

buffer layer is about 1 µm. For some applications, however, the thickness of the buffer layer can be further increased in order to decrease defect densities.

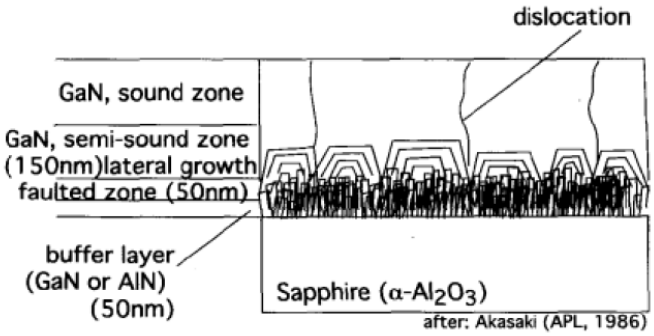

Figure 2. 1 Cartoon showing the cross-section of the high quality buffer layer developed by Akasaki. After [1], [11].

A further improvement in GaN crystal quality as well as the growth rate was achieved through the novel reactor design by Nakamura, the so-called the two flow (TF) MOCVD **[12]**. It was found out that the flow of the reactants toward the substrate was not satisfactory at high growth temperatures (around 1000º C). To circumvent this problem, Nakamura found a relatively simple solution to this problem and introduced a second gas inlet of a nitrogen (N_2) and hydrogen (H_2) mixture perpendicular to the substrate, in order to push the reactants towards it **[12]**. Together with the buffer layer approach, TF-MOCVD enabled researchers to achieve GaN films on sapphire with high crystalline quality.

The second obstacle, p-doping of GaN, is faced primarily due to the fact that GaN is intrinsically n-type due to the nitrogen vacancies **[13]**. This problem was also understood in a better way and ultimately eliminated. This was achieved through choosing the right dopant (Mg), its introduction during the growth (via a precursor gas) and activation afterwards, by annealing at elevated temperatures (700-800º C) **[1]**. It is worth mentioning that Nakamura developed most of the innovations in the area while working at a chemical company called Nichia. Nichia used the advantage of being the first in the industry and dominated the blue and green LED as well as the blue laser diode markets in the early years **[1]**.

Thanks to the advancements in the field (both by industry and academia), today achievable crystal quality and doping level of p-type layers are at satisfactory levels. Lower forward operation voltages (V_f) and higher operation currents (I_0) are achievable in LEDs and LDs. Moreover, with the developments in growth technology, large-scale and automated growth and fabrication equipment and tools have further improved the throughput and yield, reducing the cost/chip as well as cost/lumen/W (in LEDs) dramatically. Today, there are close coupled showerhead and planetary MOCVD reactors (e.g., produced by Aixtron AG) specifically designed for GaN, which can perform the growths with 55 x 2" and 56 x 2" wafers simultaneously, each one uniformly and almost identically. Figure 2.3 shows a picture of a large scale state-of-the-art MOCVD reactor.

Figure 2. 2 CRIUS-II close coupled showerhead MOCVD reactor. A state of the art tool for high throughput GaN growth. After [14].

Despite all the impressive developments and advancements in the area, there are still challenges that need to be addressed both in the device performances and the

costs for improved devices, different device applications and more market penetration **[4]**.

2.1.2 Physical Properties of III-Nitrides

Here we discuss some of the fundamental physical properties of III-Nitride semiconductor materials system. We emphasize the properties that manifest themselves in operation and performance of optoelectronic devices.

Crystal Structure of III-Nitrides

Although zincblende and rocksalt crystal structures are possible in the Group III-Nitride materials system, they predominantly have a wurtzite crystal structure, which is depicted in Figure 2.4. The wurtzite crystal is characterized by two lattice parameters a and c, and comprises alternating close-packed planes of Ga (In or Al) and N atoms in (0001) c-planes, forming an ABAB stacking squence. As a result, the surfaces of the crystals are either of Group III element (Ga-face) or N (N-face) **[15]**. This polarity brings up very interesting quantum effects that will be discussed later in this thesis.

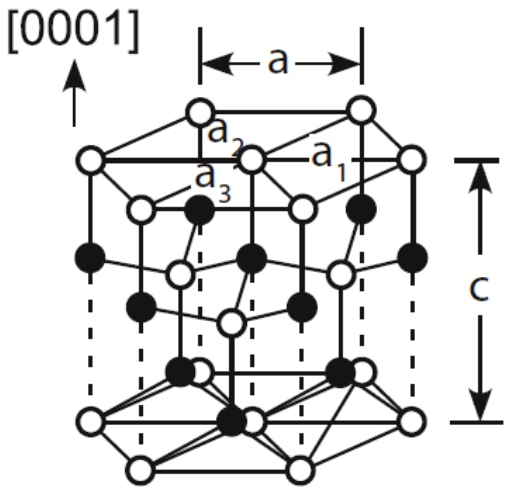

Figure 2. 3 Wurtzite crystal structure of GaN. Open circles indicate Ga atoms, closed circles show N for Ga-face material. After [16].

III-Nitrides are direct bandgap semiconductors, alloys of which ($In_xAl_yGa_{1-x-y}N$, $0 \leq x, y, x+y \leq 1$) can be tuned to have bandgap energies spanning a very wide range of optical spectrum, making them suitable for optoelectronic device

applications ranging from mid-infrared to deep ultraviolet. As we will explain further in the thesis, forming an interface of two semiconductor materials with different bandgap energies, yields a semiconductor heterostructure. Using two or more of such semiconductor heterostructures and placing them very close to each other (by a distance smaller or comparable to the exciton Bohr radius), we can form a quantum well structure and confine electrons and holes in a very close vicinity **[17]**. Through an increase in electron-hole pair recombination and generation rate, such structures usually help improve the performance of devices that utilize light generation and absorption. Quantum structures based on III-Nitride semiconductors are also very useful for these purposes. In fact, LEDs and LDs that we widely use today comprise such quantum heterostructures, that form the active layers of these devices.

Polarization effects in III-Nitrides

III-Nitride quantum structures have a property that makes them further interesting, which is related with their wurtzite crystal structure. Due to the low degree of symmetry and the aforementioned polarity in their wurtzite crystal structure, there exists a polarization field with two components: spontaneous polarization ($\mathbf{P_{sp}}$) and piezoelectric polarization ($\mathbf{P_{pz}}$) **[18]**.

Spontaneous component of the polarization field, $\mathbf{P_{sp}}$, exists in wurtzite and other low crystal symmetry structures and stems from molecular dipoles created by deviations from lattice parameters. Its direction is defined from the metal atom to the nitrogen atom, and thus exists only in c-direction. The spontaneous polarization field intensity is known (theoretically) for GaN, InN and AlN, and therefore can be calculated by simple interpolation for their alloys **[18]**.

Piezoelectric polarization, $\mathbf{P_{pz}}$, on the other hand, is due to the strain field in the material. With large differences in lattice parameters, III-Nitrides give rise to strong piezoelectric polarization fields in multilayered structures such as multiple quantum wells (MQW). In fact, the strain in these layers mostly builds up elastically during reactor's cooling down, after the growth, due to the differences in thermal expansion coefficients of different layers and the substrate.

The direction of $\mathbf{P_{pz}}$ depends on the material being Ga-face or N-face (as $\mathbf{P_{sp}}$) and the material being under tensile or compressive strain **[18]**. So, the direction of $\mathbf{P_{pz}}$ depends on the material below and above, as well. Mathematically, it can be calculated by multiplying the piezoelectric constant tensor of the material (elements calculated by linear interpolation) and the net strain field on the material. As a general rule, AlGaN on relaxed (or thick) GaN is under tensile strain and $\mathbf{P_{sp}}$ and $\mathbf{P_{pz}}$ have the same direction, whereas InGaN on relaxed GaN is under compressive strain and $\mathbf{P_{sp}}$ and $\mathbf{P_{pz}}$ have the opposite direction.

The discontinuity of the net polarization field ($\mathbf{P = P_{sp} + P_{pz}}$) throughout a quantum heterostructure causes a sheet charge formation, sign of which depends on the vector difference of the net polarization fields in the two consecutive layers **[18]**. In multilayer structures including multiple quantum well (MQW) structures, the polarization effect manifests itself as a net built-in electrostatic field, $\mathbf{E_{well}}$ or $\mathbf{E_{barrier}}$, with an alternating direction in well and barrier layers. For a periodic multiple quantum well structure, the strength of $\mathbf{E_{well}}$ or $\mathbf{E_{barrier}}$, are described by Equations (2.1) and (2.2) below **[18]**:

$$E_{tot}^{well} = E_{sp}^{well} + E_{pz}^{well} = \frac{\left(P_{sp}^{barrier} + P_{pz}^{barrier}\right) - \left(P_{sp}^{well} + P_{pz}^{well}\right)}{\varepsilon_{well} + \frac{d_{well}}{d_{barrier}}\varepsilon_{barrier}} \tag{2.1}$$

$$E_{tot}^{barrier} = E_{sp}^{barrier} + E_{pz}^{barrier} = \frac{\left(P_{sp}^{well} + P_{pz}^{well}\right) - \left(P_{sp}^{barrier} + P_{pz}^{barrier}\right)}{\varepsilon_{barrier} + \frac{d_{barrier}}{d_{well}}\varepsilon_{well}} \tag{2.2}$$

Using relevant materials parameters, we can calculate the energy band diagram of such a quantum zig-zag structure as in Figure 2.5.

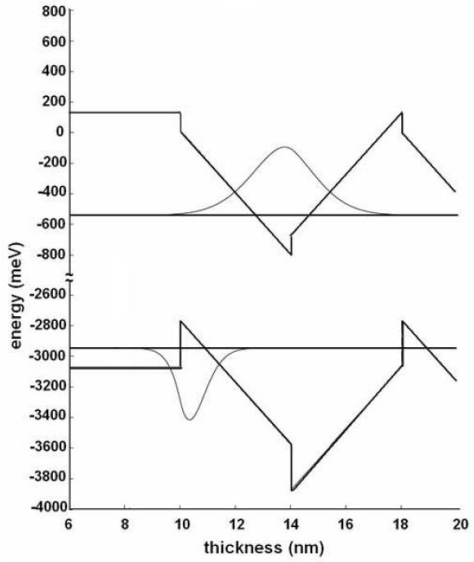

Figure 2. 4 Representative band diagram calculated for an $In_{0.15}Ga_{0.85}N$/GaN quantum structure, here the quantum well and barrier thicknesses are 4 nm.

In Equations (2.1) and (2.2), it is assumed that the potential build-up in the MQW structure due to polarization effect is zero **[18]**. Obviously, that would not be the case when some external electric field is applied to the structure. The external electric field would then be vectorially added to the built-in field in the well and barrier layers. For a typical blue LED with typical quantum well and barrier thicknesses, the built-in electrostatic field inside the quantum well is estimated to be about 300 V/μm, which is a very large, making this effect significant, reducing the probability of electron-hole recombination for light generation **[19]**. Moreover, for applications requiring larger InN molar ratios in the quantum well layers (to reduce the bandgap of quantum well material) the polarization induced electrostatic field strength in the quantum well layers increases (reducing the electron-hole overlap), since the polarization field is more discontinuous in the interfaces of the quantum wells. This means that polarization effect is more pronounced in green LEDs compared to blue or near UV LEDs. This is one of the main reasons for the lower efficiency of longer wavelength device structures in the III-Nitride optoelectronics.

As mentioned earlier and seen in the Equations (2.1) and (2.2) above, the direction of $\mathbf{E_{well}}$ or $\mathbf{E_{barrier}}$ are different. Such electrostatic fields in well and

barrier layers with alternating signs, cause MQW structures to have a zig-zag potential profile **[19]** rather than a square-like one, which is the case for other III-V MQW structures, such as those based on GaAs or InP. This property is one of the main differences between III-Nitrides and other III-V's as far as the scope of this thesis is concerned.

Nonpolar and Semipolar III-Nitrides

It is very much desirable to achieve polarization-free III-Nitride films, since the electrons and holes would not be separated with the built-in electrostatic fields, and thus excitons would not be ionized in the quantum structures of such films. This is especially important in devices for longer wavelength operation (e.g., green and red) since the polarization induced built-in electrostatic fields are stronger. The growth of such films and structures is possible by changing the growth plane to so-called non-polar planes of wurtzite structure that are perpendicular to the polar c-plane. As indicated in the Figure 2.6 below, a-$(11\bar{2}0)$ and m-$(1\bar{1}00)$ planes are possible options for non-polar growth of III-Nitrides **[20]**.

The first attempts to grow GaN on its non-polar planes were not successful and it was impossible to achieve a working device performance due to their low crystal quality **[21]**. Several substrate materials were studied to achieve high crystal quality non-polar GaN material. In one of the first successful attempts, Craven *et. al.* reported device-quality a-plane GaN on r-plane sapphire **[22]** and a-plane SiC **[23]**. However, the threading dislocation densities were still high (~10^{10} cm^{-2}). Among the proposed methods to further reduce the dislocation densities and improving materials quality were growing a thick (~100μm) buffer layer **[24]**, epitaxial lateral overgrowth **[22], [25]** and using a high temperature nucleation layer **[26]**.

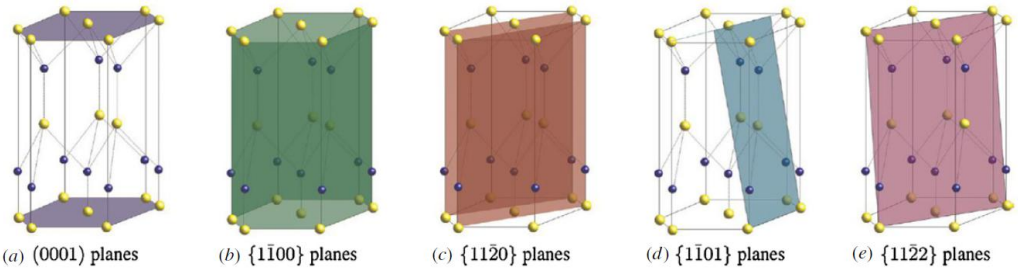

Figure 2. 5 (a) Polar, (b) and (c) nonpolar and (d) and (e) semipolar planes of wurtzite GaN crystal structure. Ga atoms are represented by yellow atoms and nitrogen atoms are represented by blue balls. After [20].

It is also possible to grow GaN on other planes that are in between the polar and non-polar planes, which are called semipolar planes. Two of the most popular semipolar planes are $(10\bar{1}1)$ and $(11\bar{2}2)$. In these cases, the built-in electrostatic fields are reduced but they are not zero. Some of these planes are given in Figure 2.6.

Although there are additional difficulties on the growth of such materials in their semipolar planes **[20]**, LEDs **[27]–[29]** and LDs **[30]** based on semi-polar GaN have been successfully demonstrated. Due to the reduced or eliminated polarization effect in their quantum heterostructures, optoelectronic devices grown on non- and semi-polar planes are of special interest to scientific community and the industry.

2.1.3 Growth of III-Nitrides

Although there are several other methods available for III-Nitride materials growth, such as molecular beam epitaxy (MBE), hydride vapor phase epitaxy (HVPE) and their derivations (e.g., plasma-assisted MBE), metal organic chemical vapor deposition (MOCVD) or metal organic vapor phase epitaxy (MOVPE) is the most popular growth method both in the industry and research, mainly due to its high throughput and good control of growth rates **[1]**. Regardless the method, c-plane growth is found to be more convenient and thus more studied and better understood compared to nonpolar and semipolar plane growth. Moreover, although there are studies on methods for obtaining free-standing GaN substrates from melt, they have not been as popular as anticipated

due to difficulties (requiring pressures up to 10 atm and temperatures up to 1500ºC) as well as small maximum achievable area and cost **[31]**. As a result, heteroepitaxy (growth on a non-native substrate) has almost become a must. Among the substrates available in the market are sapphire (Al_2O_3) popular for III-Nitride based optoelectronic devices (e.g., LEDs and LDs), and silicon carbide (SiC) for electronic devices (high electron mobility transistors) **[14]**. Using silicon as a substrate material brings a lot of advantages, especially in the cost side, and companies are working towards using silicon instead of Al_2O_3 and SiC. In all of our studies, we used sapphire substrates and performed the growth using MOCVD.

MOCVD growth of III-Nitride epitaxy

Chemical vapor deposition (CVD) is a general term used to describe a growth process which involves reaction of molecules in gas form (called precursors) and their decomposition into solid form, usually onto a substrate **[32]**. It does not imply resultant layer being crystalline, amorphous or polycrystalline. The term metalorganic (or organometallic) refers to the class of compounds used as the precursor material. Each molecule contains a metal atom and organic ligands (e.g., methyl [CH_3] or ethyl [C_2H_6]) attached to it. For III-Nitride MOCVD, the metalorganic compounds act as the Group III source, whereas ammonia (NH_3) acts as the nitrogen source. The metalorganic compounds used for AlN, InN and GaN and their alloys ($Al_xIn_yGa_{1-x-y}N$) are trimethylaluminum (TMAl), trimethylindium (TMIn) and trimethylgallium (TMGa). For the layers that require controlled and low growth rate (especially InGaN/GaN multiple quantum well layers), usually triethylgallium (TEGa) is used instead of TMGa. The basic chemical equation describing the GaN deposition process is as follows:

$$Ga(CH_3)_3(v) + NH_3(v) \rightarrow GaN(s) + 3CH_4(v) \qquad (2.3)$$

Although the above chemical reaction seems very simple, the MOCVD growth process is highly complex and hard to understand completely. Toward understanding the MOCVD growth process better, improving it and ultimately

achieving superior performing devices, researchers performed empirical studies of important parameters such as growth temperature, pressure, V/III ratio and mass flow rates **[32], [33]**. As a result of these studies, three different growth regimes were identified. These are, mass transport limited regime, desorption limited regime and surface kinetically limited regime. MOCVD growth of GaN is usually performed in the mass transport limited regime in which growth is limited by the mass transport of the Group III precursor to the growth interface. This regime occurs at a very wide temperature range (600ºC - 1000ºC) and the growth rate usually increases with temperature due to increasing diffusion rate, providing growth rate tunability as well as the ability to grow different alloys that require different growth temperatures **[34]**.

Special care has to be taken for InGaN/GaN layers, in order to obtain optoelectronic devices with good electrical and optical characteristics. This is mainly because high efficiency optoelectronic devices usually require, among other things, high quality quantum well layers with uniform thickness and abrupt interfaces. Moreover, dislocations (which form non-radiative recombination centers and reduce the quantum efficiency) in these layers should be avoided. Another reason for this necessity is because the growth of InGaN layers is difficult compared to GaN. The growth temperature of InGaN layers should be low (<850ºC), due to the low dissociation temperature of InN. Several reports on the observation of In droplets are available in the literature. On the other hand, decomposition of ammonia (NH_3) is much less efficient at such low temperatures, because of the high kinetic barrier for breaking *N-H* bonds **[34]**. This tradeoff brings up difficulties for finding a suitable growth window; however, with good growth optimization, it is possible to grow high quality device layers with good reproducibility.

The crystalline quality of the device layers (p- and n-layers and MQWs) also highly depends on the crystalline quality of the layers underneath, especially the buffer layer. Therefore, crystal quality of the buffer layer directly affects the device layers on top of it. The crystalline quality of bulk layers is usually

inspected by X-ray diffraction measurements. Generally speaking, the ω-scans of the (002) and (102) reflection rocking curves are narrower for high crystalline quality samples. It was identified that (002) relates to the screw dislocations whereas (102) relates to the edge type dislocations **[35], [36]**.

2.2 Optoelectronic Devices Background

In this chapter, we describe the physics and operation principles of some of the optoelectronic devices with a particular concentration in electroabsorption modulators and light emitting diodes (LEDs). We start from semiconductor device physics, describe some fundamental physical concepts and effects that are especially related with operation and performance of the devices of interest. Building on the semiconductor physics concepts introduced in the earlier parts, we study the optoelectronic devices in more detail. We provide information on the simulation software package that we use for LEDs called APSYS.

2.2.1 Optical processes in semiconductors

In this part, we summarize processes concepts of optical absorption and spontaneous emission, which are related with the operation principles of LEDs, LDs and electroabsorption modulators.

In semiconductors, optical absorption refers to the process of generation of an exciton, bound charge carrier (electron+hole) pair in response to an incident photon. In the case of most semiconductors and devices, electron-hole pair generation occurs by raising an electron from a valence band state to a conduction band state, both of which essentially have the same momentum **[37]**. The process can be described by Figure 2.7:

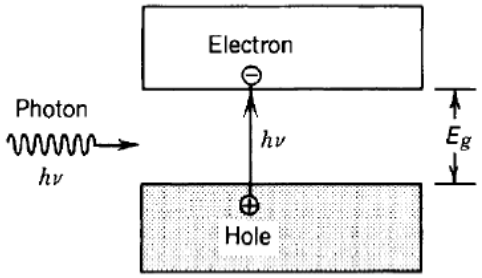

Figure 2. 6 Interband (band-to-band) absorption (carrier generation) in a semiconductor. An electron in the valence band is raised to another state in the conduction band by a photon. After [37].

This type of "vertical" transition with momentum conservation describes a direct transition, which is the case for direct bandgap semiconductors like GaAs, GaN, as well as their alloys with other direct semiconductor materials. Moreover, the transition between the conduction and valence bands (rather than within either of the bands) describes an interband (or band-to-band) transition. Here in this thesis, we concentrate on interband transitions in InGaN/GaN quantum structures since the devices we will introduce rely on them. Also, as mentioned earlier, since III-Nitrides are direct bandgap semiconductors, the processes we describe in this thesis work involve direct transitions.

Such transitions might require electron-hole pair generation or recombination. Carrier generation is the process of an electron moving from valence band to the conduction band, with the energy obtained from the absorption of an incoming photon. Electron-hole pair recombination is the opposite of the generation process, and an injected electron is moved from conduction band to valence band and the excess energy is released either as a photon or a phonon emitted from the semiconductor if the process is radiative and as phonon if it is non-radiative. The energy of the emitted photon is determined by the energy difference of initial and final electron states, and either of these states can be an impurity-related luminescent center. InGaN/GaN based LEDs rely on band-to-band transitions; however, impurity-related luminescent center emissions also exist. If the excess energy is transferred to a phonon nonradiatively, it is dissipated as lattice

vibrations and converted to heat. Figure 2.8 summarizes some of the most important optical processes in semiconductors that we described above.

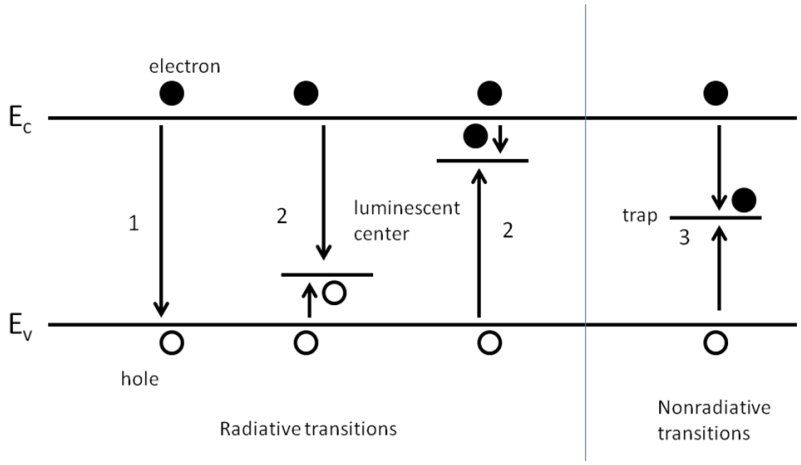

Figure 2. 7 Interband (band-to-band) recombination mechanisms. Reproduced after [1].

Band-to-band radiative recombination or stimulated emission is given in process 1 and it is the main mechanism for LEDs. Although radiative recombination through luminescent centers (process 2) is possible in semiconductors, the photons produced by this mechanism do not contribute to useful light for InGaN/GaN LEDs. As mentioned before, nonradiative transitions should be avoided as far as light emitting devices are concerned **[1]**.

There are a few definitions that are helpful for our understanding of optical processes in semiconductors and devices that rely on them. One definition is the internal quantum efficiency, η_{int}. The internal quantum efficiency is the ratio of the number of photons emitted inside the semiconductor to the number of carriers that undergo recombination. In other words, it is the probability that a given recombination is radiative **[38]**.

The rates of radiative and nonradiative recombination can be described by inverse of the corresponding lifetimes, τ_r^{-1} and τ_{nr}^{-1}. Through Fermi's golden rule, the rate of radiative recombination is proportional to the probability of finding an electron and a hole in the same vicinity, which mathematically and quantum mechanically is the squared overlap integral of electron and hole wavefunctions **[39]**. The total

recombination rate τ^{-1} would be the summation of the two rates. Then internal quantum efficiency, η_{int}, can be calculated as the ratio of τ_r^{-1} and τ^{-1}.

$$\eta_{\text{int}} = \frac{\tau_r^{-1}}{\tau^{-1}} = \frac{\tau}{\tau_r} = \frac{\tau_{nr}}{\tau_{nr} + \tau_r} \tag{2.4}$$

Obviously, the efficiency of an LED depends on the internal quantum efficiency of the active material used **[38]**. Therefore, understanding the radiative and nonradiative recombination lifetimes (τ_r and τ_{nr}) is of special importance for our understanding of optoelectronic devices, especially LEDs.

2.2.2 Electroabsorption in semiconductors

When external electric field is applied to semiconductors, their optical absorption spectra change, this is known as electroabsorption. There are two main mechanisms of electroabsorption: the first one is Franz-Keldysh effect, which is seen in bulk semiconductors, and the other is quantum-confined Stark effect (QCSE), which is seen in quantum structures.

Franz-Keldysh Effect

Franz-Keldysh effect (FKE) **[40], [41]** appears in bulk semiconductors in which the optical absorption occurs at photon energies equal to or larger than the bandgap of the semiconductor material. When an external electric field is applied across a bulk semiconductor material, the conduction and valence band potential profile become tilted in the energy band diagram. Assisted by an absorbed photon, an excess electron in the valence band can tunnel into the conduction band. In the absence of the external electric field, such transition would not be possible. Another explanation of the same phenomenon is through an eigenstate approach, which is mathematically simpler. Consider an electron in a bulk semiconductor, in the presence of an external electric field in z-direction. The Schrödinger equation then becomes the following:

$$\left[-\frac{\hbar}{2m_e}\frac{\partial^2}{\partial z_e^2}+V_e-eE_{ext}z\right]\psi_e(z_e)=E_c\psi_e(z_e) \tag{2.5}$$

The solutions to this equation are the Airy functions, which take the form of oscillatory functions for positions of z where the energy eigenvalue $E_c > V_e - eE_z$ and decaying functions otherwise (within the bandgap) as depicted in Figure 2.9 below.

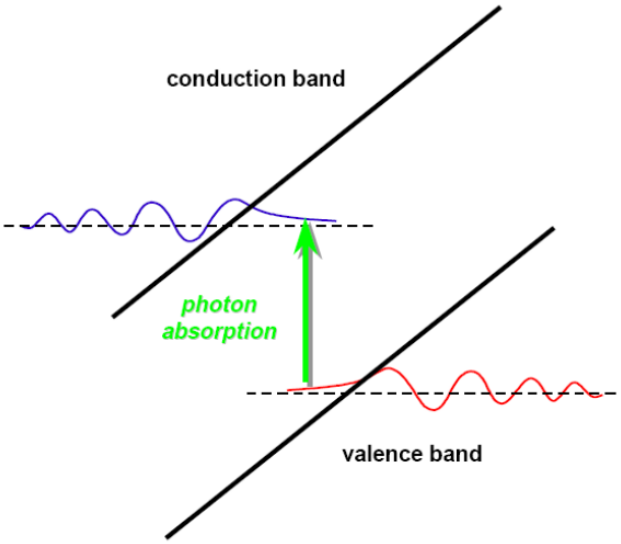

Figure 2. 8 Schematic representation of Franz Keldysh effect. Courtesy of Prof. David Miller.

The same procedure can be followed for the holes and again eigenfunctions of decaying behavior can be found. It can be predicted through this observation that, application of an external electric field can induce absorption below its bandgap energy, making it absorbing where it is initially transparent. In other words, absorption edge, the wavelength in which the absorption starts, shifts to longer wavelengths (lower photon energies) with the external electric field application. This is especially useful for modulators, by which we can control the absorption level of light. Such devices based on other III-V semiconductors have been thoroughly studied and used in relevant applications **[42]–[45]**.

Quantum-confined Stark effect

Similar to Franz-Keldysh effect, quantum-confined Stark effect (QCSE) describes electroabsorption, but this time in quantum structures. In optoelectronics, there are many important and useful outcomes of using quantum structures (e.g., quantum wells, wires or dots) instead of bulk material. Since the carriers are confined in one or more directions, strong excitonic effects can be exhibited. QCSE is one of such strong effects.

In quantum-confined Stark effect, similar to FKE, absorption edge redshifts with the external electric field perpendicular to the quantum well layers **[42]**. The mechanism is depicted in Figure 2.10 for an infinite quantum well structure.

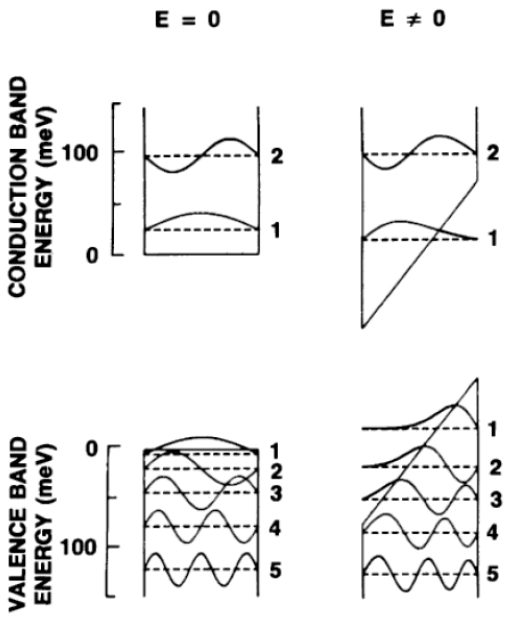

Figure 2. 9 Electron and hole states in an infinite quantum well with zero external electric field and non-zero electric field. Courtesy of Prof. David Miller.

There are a couple of remarks to consider in this visual description of QCSE:

First, electron and hole are pulled in different directions by the electric field and electron and hole wavefunctions overlap less compared to the zero external electric field case. This is an important observation, since the rate of a transition between such states is known to be directly proportional to the squared overlap

integral of electron and hole wavefunctions $\left|\langle e|h\rangle\right|^2$ through Fermi's golden rule **[39]**. Moreover, previously forbidden transitions are allowed for the non-zero external electric field case, since the states are not orthogonal anymore. We will discuss the implications of this observation further in Chapter 5.

As a second remark, the transition energy between electron and hole states is smaller in non-zero external electric field case, indicating a redshift of absorption edge, as in the case of FKE. Representative experimental absorption spectra of an AlGaAs/GaAs multiple quantum well structure at different external electric field levels (perpendicular to the MQW) are given in Figure 2.11.

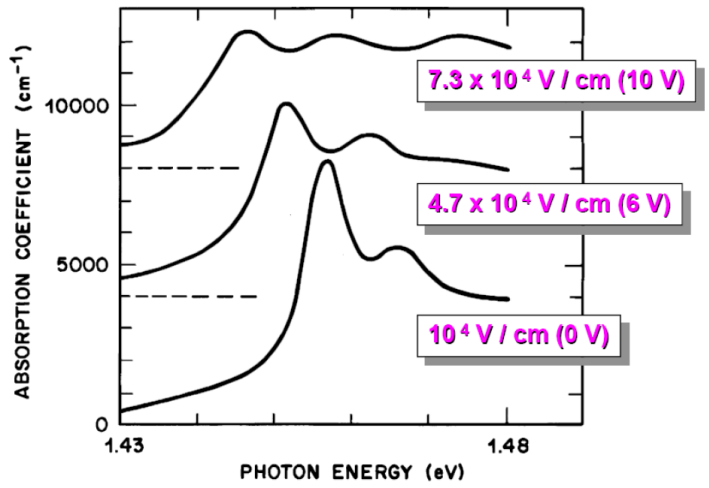

Figure 2. 10 Optical absorption spectra for AlGaAs/GaAs quantum well structure for various electric fields applied perpendicular across quantum well layers measured at room temperature. The spectra are shifted vertically to dashed levels for clarity. Courtesy of Prof. David Miller.

It is seen clearly that exciton peaks are shifted to lower energies and become weaker with increasing external electric field. The explanation for that comes from the fact that the electron and hole are separated form each other. As a result, the probability of finding an electron and hole in the same vicinity decreases; and consequently, excitonic absorption decreases.

QCSE has been widely studied and exploited in relevant applications, mostly in GaAs and InP platform **[43]–[45]** and recently successful demonstrations were

made in SiGe platform **[46]**. All these applications were in the infrared region of the optical spectrum. As we will describe in the next parts, we have demonstrated InGaN/GaN based quantum electroabsorption modulators and studied their underlying physics for better understanding.

Absorption coefficient

Absorption coefficient (denoted as α) is another important physical quantity for our understanding of optical properties of materials, especially semiconductors. In most of the materials, optical absorption can be formally explained as an exponential attenuation of photon flux that passes through the material, characterized by a characteristic absorption coefficient (with units in cm^{-1}). For a device in which photons are absorbed and converted to electron-hole pairs, and electron-hole pairs are collected in the external circuit, such as photodetectors and electroabsorption modulators, the absorption coefficient can simply be related to measurable quantities with the following equation:

$$\alpha = -\frac{1}{d}\ln\left(1 - \frac{i_p}{P_0 \lambda}\frac{1.24}{\zeta(1-R)}\right) \tag{2.6}$$

Here in this equation d is the thickness of the absorbing medium, i_p is the photocurrent, P_0 is the optical power in Watts, λ is the wavelength in μm, ζ is the ratio of electron-hole pairs that successfully contribute to photocurrent and R is the Fresnel power reflectance. By using absorption coefficient, performance and underlying physics of electroabsorption modulators can be studied easily.

2.2.3 LED Model Used

For our LED studies, we used a finite element analysis based simulation package called APSYS (Advanced Physical Models of Semiconductor Devices). APSYS is capable of modeling current-voltage characteristics, and many important parameters such as optical power and spectrum, carrier distributions and band diagrams at various current injection levels. The results deduced from APSYS simulations are very helpful for our understanding of LED operation and possible ways to improve its performance.

2.3 III-Nitride Optoelectronic Devices

In this part, we review some of the research work performed in III-Nitride optoelectronic devices field. We start with early work on InGaN/GaN based LEDs and address important achievements, and continue with InGaN/GaN based electroabsorption modulators.

2.3.1 InGaN/GaN based visible LEDs

As mentioned earlier, the first demonstrations of III-Nitride based optoelectronic devices were InGaN/GaN based LEDs, which were demonstrated in early 1990s by Shuji Nakamura of then Nichia Corporation. In the early demonstrations of InGaN/GaN based blue LEDs **[1]**, the forward voltage, V_f, (defined as the voltage at a driving current of 20 mA) was as high as 10 V and the optical output power level was as low as about 0.125 mW (again, at I=20 mA). A few years after the first demonstrations, the improvements in the device performance were impressive; V_f was reduced down to 3.6 V and the achieved output power levels were as high as 4 mW **[10], [47], [48]**. These developments were mainly due to the improvements in the p-doping levels, crystal quality and control on InGaN deposition. Moreover, the latter enabled researchers to extend the operation wavelength range of the LEDs to longer wavelengths, to about 525 nm, which corresponds to green.

Electron blocking layers in LEDs

In the early days of InGaN/GaN based blue LEDs and LDs, a critical improvement in their performance was made through inserting an electron blocking layer (EBL) on top of the multiple quantum well structure, preventing the electron overflow from the active region. The electron overflow in these devices was identified as a major problem because of large electron leakage due to larger diffusion constant of electrons compared to holes, and poor hole injection into the active region due to low hole mobility in III-Nitrides.

The EBL is usually composed of p-AlGaN with a typical AlN ratio of 20% and a thickness of 10-20 nm. A representative band diagram (neglecting polarization induced electrostatic fields in MQW) of an InGaN LED with an EBL is shown in Figure 2.12 below.

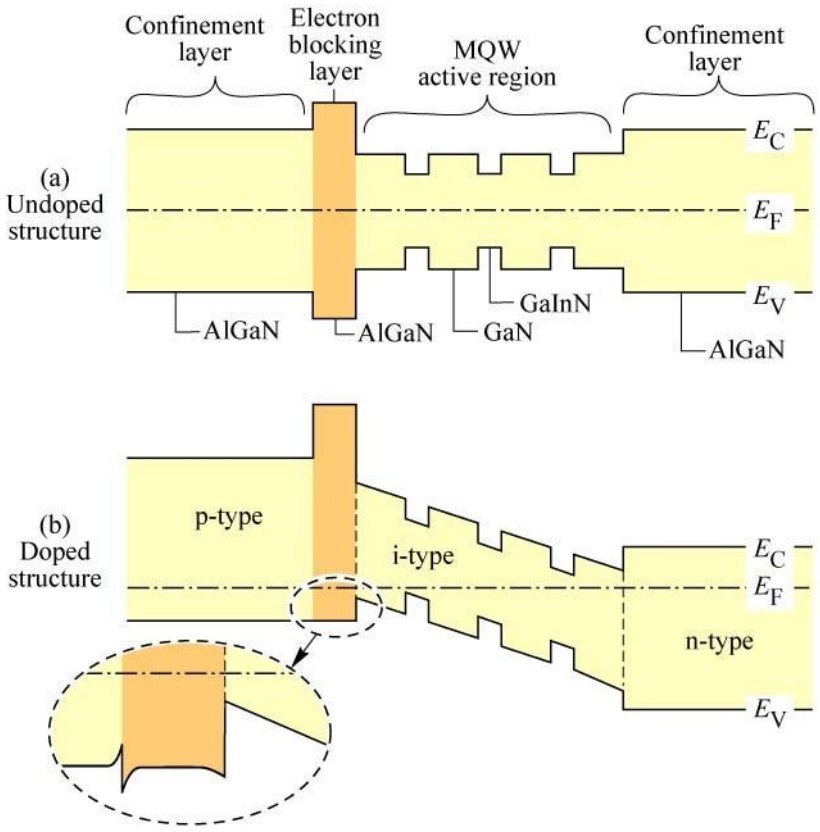

Figure 2. 11 Band diagrams of two LEDs incorporating (a) an undoped AlGaN EBL and (b) a p-doped AlGaN EBL. After [38].

The Figure 2.12(a) illustrates that the undoped AlGaN EBL acts as a barrier to current flow in both conduction band and valence band. In Figure 2.12(b), valence band edge is smoothed out by the p-doping of the EBL. However, as shown in the inset of the same figure, where the valence band is shown in more detail, there exists a potential spike and notch at the EBL and p-layer interface. It is necessary for holes to tunnel through the potential spike for their injection into the active region and ultimately radiative recombination with electrons. This is an unwanted effect for the incorporation of holes into the active layer. Despite that, today, EBLs are widely used in LEDs and LDs.

Efficiency droop in LEDs

For most applications that LEDs are used such as general lighting, it is necessary to obtain high optical power output levels. In order to achieve high optical power levels, it is necessary to operate LEDs at high current injection levels, another solution would be to increase the number of chips used and/or increase the area of each chip, but those would increase the cost per chip and cost per lumen. For typical sized devices (e.g., 300 μm × 300 μm), the driving currents of more than 350 mA are usually necessary. However, the efficiency of LEDs is the highest at much lower current levels (<50 mA). For larger current levels, the efficiency monotonically decreases. This decrease is called *efficiency droop* **[49]**. In Figures 2.13(a) and 2.13(b), we present LED efficiency *vs.* current and light output *vs.* current (inset) curves of a typical LED with droop and an LED with no droop. For the typical LED, the LED power deviates from the ideal linear increase with increasing current.

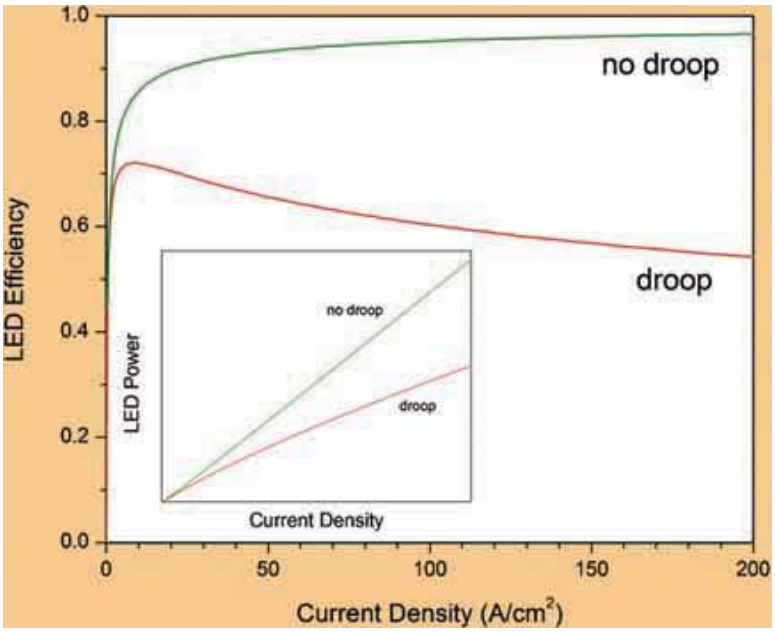

Figure 2. 12 LED efficiency *vs.* current and LED power *vs.* current (inset) curves of a typical LED with droop and ideal LED with no droop. After [49].

This problem is known to be stronger in LEDs that operate at longer wavelengths (e.g., green LEDs) and is not related with thermal rollover effect. For that reason it is sometimes referred to as *non-thermal rollover*. Despite the physical

mechanisms that lead to the efficiency droop are still under discussion **[49]–[51]**, several methods to reduce this effect (such as using polarization-matched MQW or p-doped barriers) have been proposed **[52]–[54]**. Recent research has shown that AlGaN electron blocking layers with typical thickness and alloy ratios are not satisfactory for solving the efficiency droop problem, mainly due to being unable to completely prevent electron leakage from the active region, and prohibiting hole injection into the active region, simultaneously. Several novel EBL designs have been proposed in order to relieve this effect and droop levels; here we will refer to such one study by Zhang, *et. al*. **[55]**. In this work, the droop level of a blue LED with an AlGaN/GaN superlattice EBL with a gradual Al mole fraction was analyzed. The results were compared with a traditional EBL with 20% AlN mole fraction, and another superlattice with constant AlN mole fraction as depicted in Figure 2.14 below.

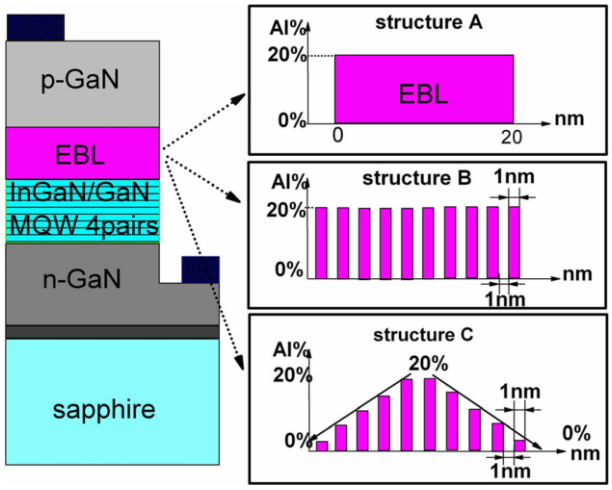

Figure 2. 13 The Schematics illustrating three structures studied in Ref. [56]: (a) the conventional structure with constant AlN molar ratio of 20% (structure A) , (b) the normal superlattice structure with constant AlN molar ratio of 20% (structure B) and (c) the gradual superlattice structure with triangular AlN molar ratio (0-20-0%) (structure C). After [56].

The structures were analyzed using APSYS; band diagrams of the structures indicating quasi-Fermi levels (a) to (c) and electron and hole concentrations (d) to (f) are given in Figure 2.15 below.

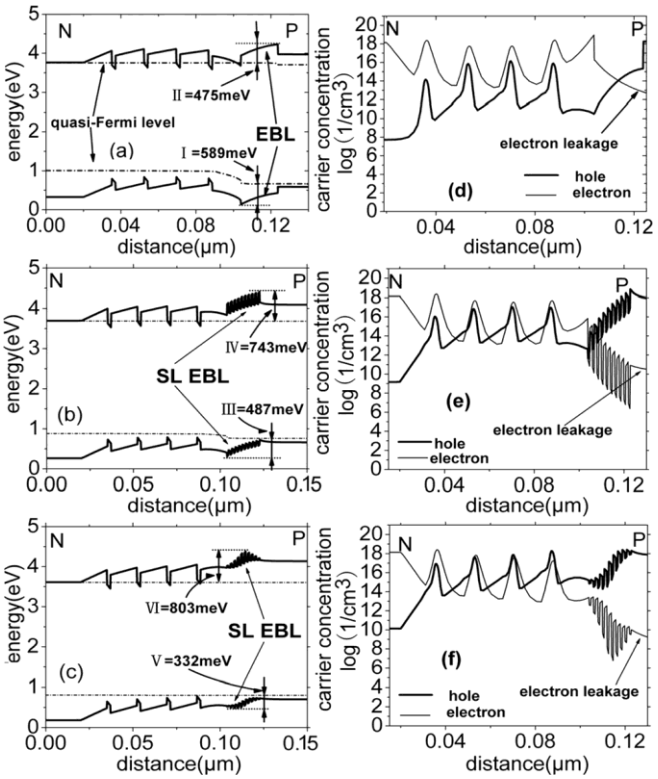

Figure 2. 14 Band diagrams and carrier concentrations of structures A, B and C at the current density of 200 A/cm^2. After [56].

As seen in Figure 2.15, the effective potential height for holes in structure A is the highest and the same for electrons is the lowest among the three. As a result, the electron leakage is the highest and hole incorporation in quantum well regions is the lowest for structure A. In structure C, however, the electron leakage is slightly lower than that of structure B, and electron and hole concentrations in the quantum well regions are much more balanced. In the internal quantum efficiency *vs.* current density curves given in Figure 2.16, we can clearly see this effect. According to the simulation results, structure C shows the highest maximum IQE and lowest droop level (12% with 400 A/cm^2), whereas structure B with constant Al mole fraction superlattice EBL and structure A traditional EBL exhibit droop levels of 16% and 69%, respectively.

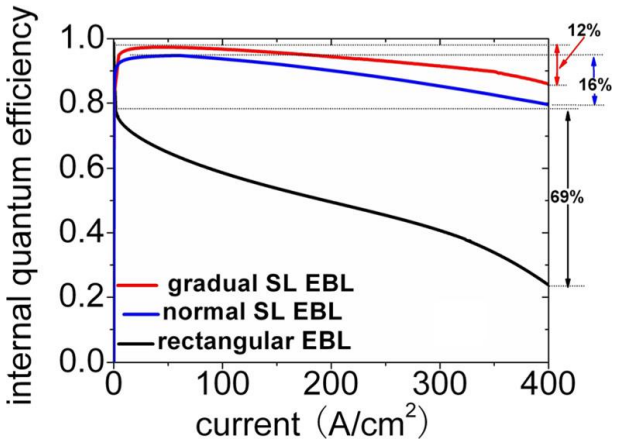

Figure 2. 15 Dependence of internal quantum efficiency (or LED efficiency) on the current density showing droop levels for the structures. After [56].

Further reduction of efficiency droop is necessary for high current operation and ultimately larger market penetration of InGaN/GaN LEDs. Novel EBL designs are expected to pave the way towards these goals. In this thesis work, we will address the droop problem in LEDs and try to further improve device performances in this respect, through device and bandgap engineering.

2.3.2 InGaN/GaN based electroabsorption modulators

As mentioned throughout this chapter, optoelectronic devices based on InGaN/GaN quantum structures have found several important applications in critical areas such as lighting and data storage. They are expected to replace their older counterparts due to several advantages they offer. However, what III-Nitride material platform can offer is not limited to these applications. Aiming at expanding such applications, we previously demonstrated InGaN/GaN based electroabsorption modulators (EAMs) operating at the visible part of optical spectrum **[57]**. EAMs that operate in the blue wavelength range (λ~440 nm) were proposed as a chip scale solution for direct optical clock injection into Si CMOS microchips using Si based photodetectors **[58]** fabricated with the same technology.

From physics point of view, EAMs based on III-Nitride quantum structures render a very interesting property due to polarization-induced electrostatic fields, in the context of quantum-confined Stark effect. As a result of our transfer matrix

method based simulation results, which are shown in the Figure 2.17 below, when the external electric field is applied in opposite direction to the built-in polarization-induced electrostatic field inside the quantum well layers, the transition energy of electron and hole increases and, as a result, the absorption edge shifts to higher photon energies and, thus, to shorter wavelengths (i.e., blueshifts). Moreover, the overlap of electron and hole wavefunctions increases with the external electric field.

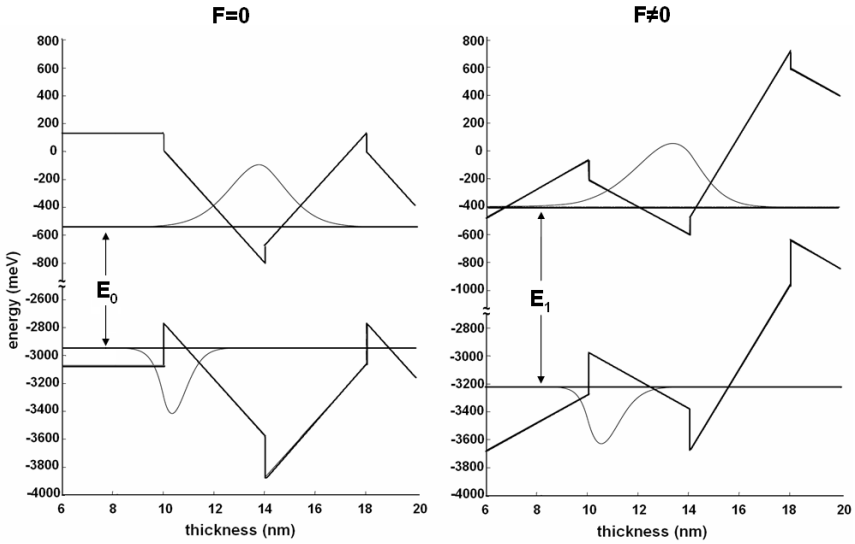

Figure 2. 16 Energy band diagrams of an InGaN/GaN quantum structure for zero external electric field case and non-zero external electric field case. After [57].

We designed our electroabsorption modulators comprising of InGaN/GaN quantum structures with a target operation wavelength of 425 nm and performed MOCVD growth and fabrication steps accordingly. As a result of our experiments, we also observed blueshifting absorption edge with the external electric field, in agreement with our simulation results and demonstrated reversed quantum-confined Stark effect (r-QCSE) as in Figure 2.18 below.

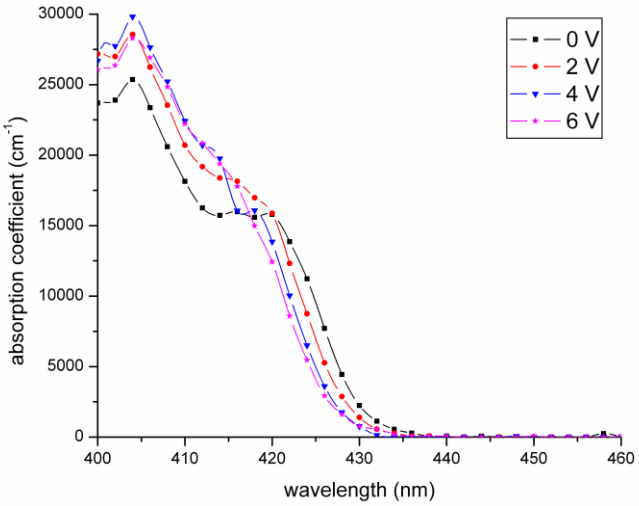

Figure 2. 17 Absorption spectra of our EAM at 0-6 V levels. The absorption edge shows a clear blueshift with increasing external electric field. Reproduced after [57].

Moreover, we achieve absorption coefficient change values as large as 6000 cm^{-1} with a voltage swing of 0 to 6 V, as seen in Figure 2.19, where we present the absorption coefficient changes with respect to the 0 V absorption curve.

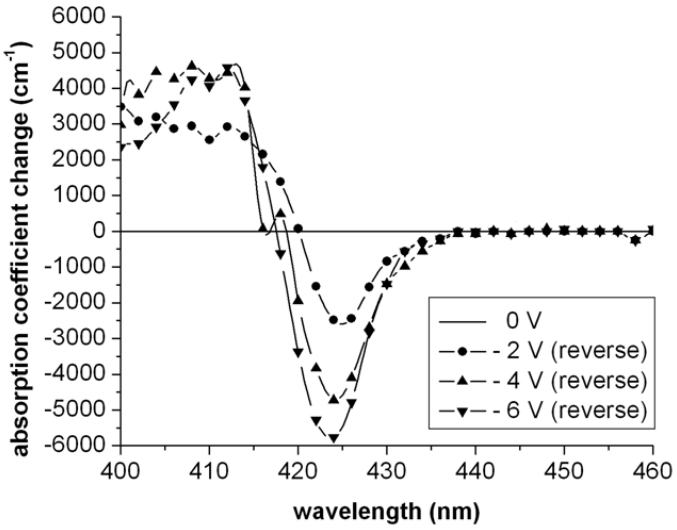

Figure 2. 18 Absorption coefficient change with respect to 0 V absorption curve. After [57].

Electroabsorption modulators based on InGaN/GaN quantum heterostructures are promising candidates for the generation of optical clocking signals in the blue wavelength range, where Si based photodetectors can be operated at high speeds with high responsivity. Understanding the underlying physics of these devices is

essential to improving device performances and pursuing other possible applications in related areas of communication and sensor technologies. In this thesis work, building upon our earlier work presented above, we further study InGaN/GaN quantum structures for the electric field dependence of their optoelectronic properties.

2.4 Summary

In summary, we provided background information for III-Nitride materials, optoelectronic devices, specifically LEDs and EAMs based on InGaN/GaN quantum structures. We introduced polarization-induced electrostatic fields in III-Nitride quantum structures and addressed several consequences of this effect. Moreover, we explained MOCVD growth of III-Nitrides and mentioned several research activities in this aspect.

Chapter 3

Epitaxial Lateral Overgrown InGaN/GaN Quantum Structures

This chapter is based on the submitted publication "*Dislocation density dependent electroabsorption in epitaxial lateral overgrown InGaN/GaN quantum structures*" Emre Sari, Lee Woon Jang, Jong Hyeob Baek, In Hwan Lee, Xiao Wei Sun, and Hilmi Volkan Demir**.**

In this chapter, we describe our study on InGaN/GaN quantum structures grown using epitaxial lateral overgrowth (ELOG). We performed electroabsorption (EA) measurements together with steady state photoluminescence (PL) and time-resolved PL (TRPL) and found the results to be in correlation with their dislocation density levels. Our results show that ELOG structures with low dislocation densities exhibit stronger EA performance, with a maximum EA enhancement factor of 4.8 compared to the reference without ELOG. Also, while keeping the growth window widths constant, compared to the PL intensity levels, EA exhibits larger sensitivity to the dislocation density, which decreases with decreasing ELOG mask stripe widths leading to larger EA. Our analyses further reveal that the EA performance as well as the essential parameters of PL spectra

(peak position, width and intensity) together with photoluminescence lifetimes follows similar trends with the dislocation densities.

3.1 Introduction

Epitaxial lateral overgrowth, which is based on the selective area growth, is one of the most powerful techniques for the reduction of threading dislocation densities, thus enabling substantial improvement in the crystal quality of GaN material system **[59]**. Under proper conditions, ELOG results in smooth surfaces with low defect densities by blocking propagation of the defects underneath the hard mask, usually defined by Si_3N_4 or SiO_2 on a GaN template. This involves lateral growth over the mask, hence preventing the defects from propagating to the surface and leading to a surface with significantly fewer defects for the growth of subsequent layers **[60]**. ELOG can also be applied for multiple times for further improvement in crystal quality. A schematic representation of the ELOG process is given in Figure 3.1 below.

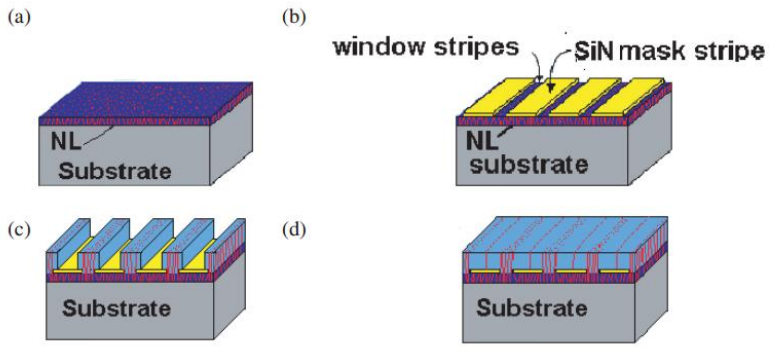

Figure 3. 1 Schematic of one-step ELOG process. After [60].

As investigated by several groups to date, ELOG has proven to be a successful method to improve GaN material quality as well as the performance of resulting optoelectronic devices including LEDs **[61]** and LDs **[62]** when grown on polar **[63]**, semipolar **[64]** and nonpolar **[65]** directions of their crystals. ELOG-LEDs with embedded micro-mirror arrays have also been demonstrated to further improve the light extraction efficiency **[66]**.

In terms of understanding the underpinning physical mechanisms, electroabsorption offers a unique means to explore and understand physics of semiconductor structures. This is especially the case for quantum-confined structures, which exhibit electroabsorption exceptionally stronger than their bulk counterparts through quantum-confined Stark effect (QCSE) **[42]**. Electroabsorption modulators that utilize QCSE have found applications in telecommunications in the last few decades, e.g., in data coding **[45]** and optical switching **[67]**. Most of these studies involved InP/GaAs material system, and the operation wavelength of these devices has therefore been typically in the mid-infrared part of the electromagnetic spectrum. On the other hand, electroabsorption modulators based on III-Nitride quantum structures, which operate in the blue **[57]** and ultraviolet **[68]** region of the electromagnetic spectrum, were also demonstrated. These find applications in optical clock injection directly into silicon chips **[58]** and none-of-sight communications **[69]**. However, electroabsorption in InGaN/GaN quantum structures grown on ELOG-GaN has not been studied.

Here in this part of the thesis, we report electroabsorption performance of epitaxial lateral overgrown InGaN/GaN quantum structures, combined with their steady-state and time-resolved photoluminescence properties, and correlate our results with the dislocation density levels. In this study, we employ a set of four epi-structures, three of which are designed to contain systematically varying ELOG mask stripe widths while the last one is used as a reference sample without ELOG.

3.2 Experiments, results and discussion

Our epitaxial structures were grown using metal-organic chemical vapor deposition (MOCVD). After the growth of 5 µm thick u-GaN templates on single side polished sapphire substrates, we deposited and defined SiO_2 stripe patterns all in $\langle 1\bar{1}00 \rangle$ direction. The width of the SiO_2 stripe masks was 4, 7 and 10 µm, whereas that of the unmasked window regions was kept constant at 4 µm for the three samples containing ELOG stripe patterns. No patterning was used for the

fourth sample, which serves as the reference. We followed a standard single-step ELOG procedure **[59]**. The lateral growth time was sufficiently long for each of our samples to completely coalesce in the middle-top part of the mask regions. After the coalescence, we changed the growth mode to vertical growth to obtain 2 µm thick Si doped n-type GaN layer ($N_{Si} \approx 4 \times 10^{18}$ cm^{-3}) and InGaN/GaN multiple quantum well (MQW) structure with 5 pairs of well and barriers having thicknesses of 2.5 and 7.5 nm, respectively. After the growth of the MQW, we continued with Mg-doped 150 nm thick p-GaN layer ($N_{Mg} \approx 6 \times 10^{17}$ cm^{-3}) and completed the epi-samples. In Figure 3.2 we present a cartoon showing the cross-section of an exemplary ELOG sample.

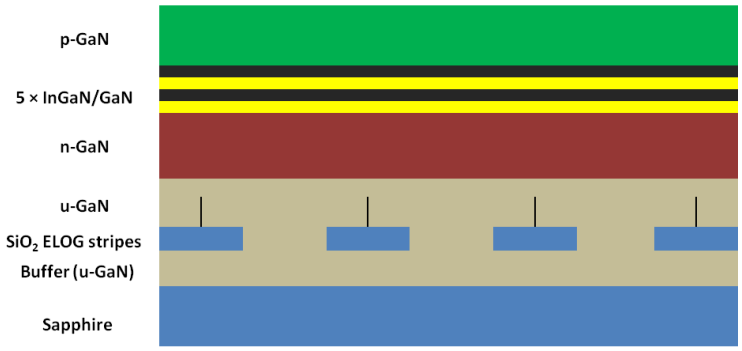

Figure 3. 2 Cartoon showing the cross-section of an ELOG sample before device fabrication. The lines on top of the SiO_2 ELOG stripes represent coalescence walls.

Device Fabrication

We fabricated devices using these ELOG and reference epi-samples utilizing standard photolithography, mesa etching and metallization procedures. The fabrication and subsequent characterization of the devices were performed under the same conditions, all with identical settings and parameters. The mesa size of the resulting devices is 300 µm × 300 µm. These devices allowed us to apply external bias and extract photocurrent for electroabsorption study (in the case of reverse biasing).

We start the fabrication of our devices by cleaning our samples through soaking them in acetone and isopropanol in an ultrasonic bath. After drying them using a

nitrogen gun, we spin-cast the photoresist (AZ 5214 at 4000 rpm for 50 s) and then softbake at 110°C for 55 s on a hotplate. Using a mask aligner and photomask, we follow a positive photolithography procedure and expose our samples by UV light (Hg arc lamp) at ~150 mJ exposure energy per cm^2 as depicted in Figure 3.3. Then we develop our samples using AZ 400K (1:4) for 1 min and rinse them in de-ionized water. As seen in Figure 3.4, the parts of photoresist that are exposed to UV light get dissolved in the developer solution, while the parts that are not exposed to UV remain. When necessary, we follow a postbake procedure (typically 2 min at 110°C on a hotplate) to harden the photoresist.

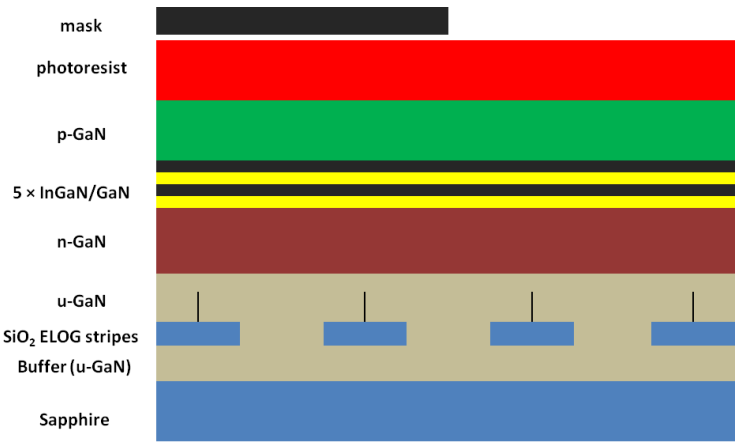

Figure 3. 3 Photolithography procedure: mask is placed on the sample which was previously coated with photoresist, and UV light is then applied.

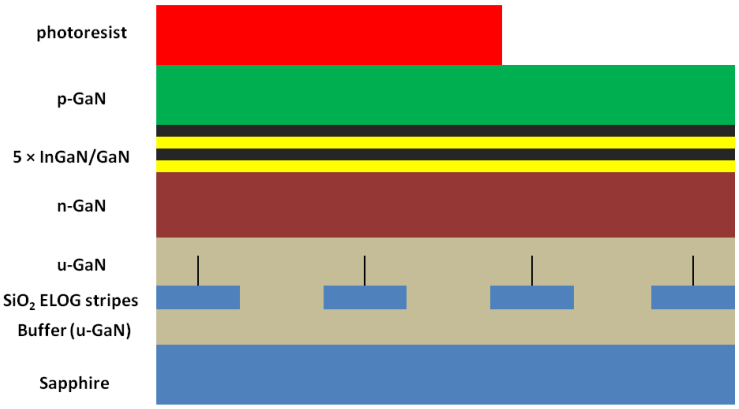

Figure 3. 4 Sample after photolithography and subsequent development.

After this step, our samples are ready for etching. We perform a chlorine based (for our case, dichlorodifluoromethane, CCl_2F_2) reactive ion etching (RIE) procedure for this fabrication step. We immediately clean the photoresist that stays on the sample using acetone and isopropanol after the etching and form the mesa as in Figure 3.5.

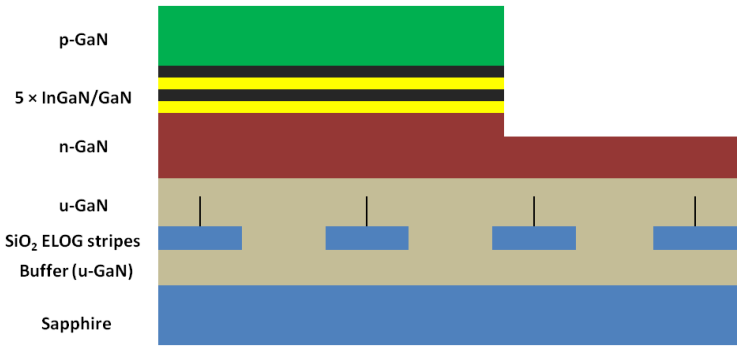

Figure 3. 5 Sample after mesa etching procedure (using RIE) and cleaning of the photoresist. The sample is etched down to n-GaN layer.

Different than the metallization step, we perform the lithography of p- and n-contacts in an image reversal fashion. For image reversal photolithography, we first expose our samples to UV light of ~60 mJ exposure energy per cm^2, with the mask features aligned properly using alignment marks near the corners of each sample. Subsequently, we do the reversal bake of 110°C for 2 min on a hotplate. After the reversal bake, we perform the flood exposure with the same exposure energy (~150 mJ) and the development with the same duration (1 min). Following the negative photolithography process, we perform metallization and lift-off procedures, respectively. As in Figure 3.6, we first deposit n-contacts using thermal or e-beam evaporation and use Ti/Al/Ti/Au with 10 nm / 100 nm / 10 nm / 100 nm thicknesses. Since the total thickness of the metals (~220 nm) is much thinner than the thickness of the photoresist (1.4 µm), the acetone attacks and dissolves the photoresist and lifts the metal coating where we do not want the metal to be deposited. For ohmic contact formation, we anneal the sample typically around 550 °C for 5 min in a N_2 environment using rapid thermal

annealing (RTA). We follow the same procedure for p-contacts and p-pads as illustrated in Figure 3.7. For p-contact, we sputter indium-tin oxide (ITO) with 100 to 150 nm of thickness and anneal it at 250°C for 15 min. For p-pads, seen in Figure 3.8, we use Ti/Au with 10 nm / 100 nm of thicknesses and perform no annealing.

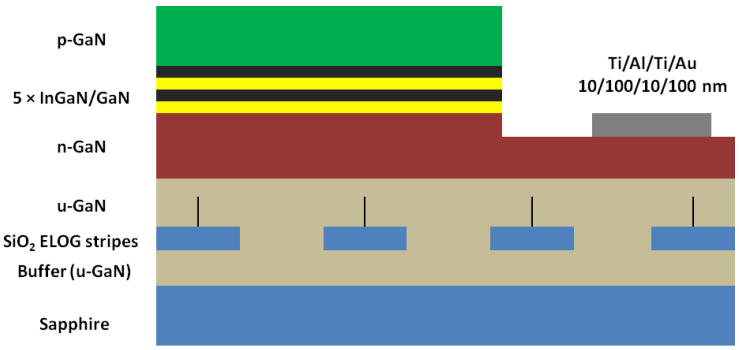

Figure 3. 6 Sample after n-contact deposition and annealing.

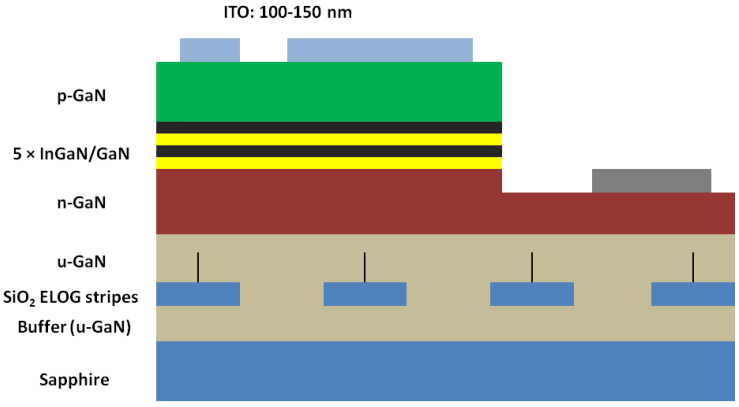

Figure 3. 7 Sample p-contact deposition and annealing.

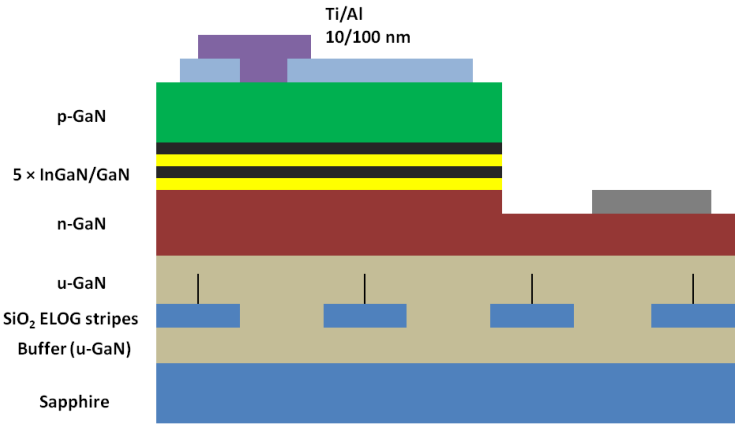

Figure 3. 8 Sample after p-pad deposition. Sample is ready for test.

In Figure 3.9, we present a micrograph of a fabricated device. This particular structure has 4 μm mask and window widths. Here, the reverse C-shaped metal is n-contact and the C-shaped metal is p-pad and the dark square is ITO p-contact.

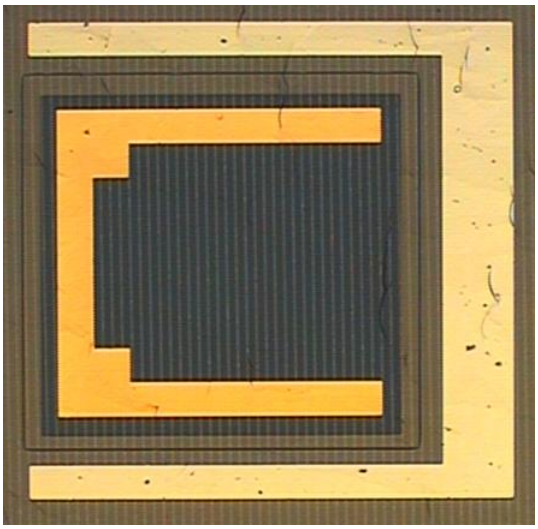

Figure 3. 9 Micrograph of a fabricated device comprising 4 μm mask and window widths

Materials Characterization

Following the MOCVD ELOG growth of our samples, we measured the dislocation densities through forming etch pits using wet etching and investigating scanning electron microscopy (SEM) images presented in Figures 3.10(a)–(d). Our analyses show that the etch pit density for the reference sample

was the highest and that of the ELOG sample with 4 μm wide stripes was the lowest, with the respective values of 3.25×10^8 and 0.88×10^8 cm^{-2}. The etch pit densities of the other ELOG structures with 7 and 10 μm wide stripes were 1.84×10^8 and 1.58×10^8 cm^{-2}, respectively **[70]**.

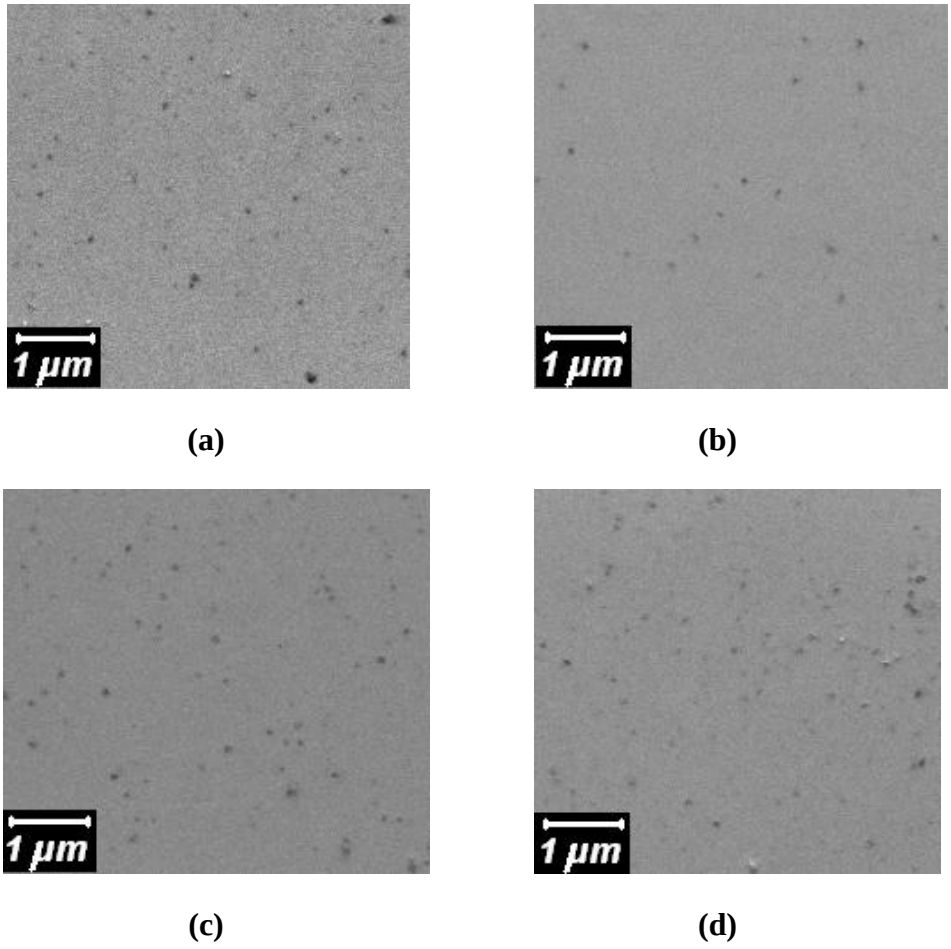

Figure 3. 10 Representative parts of the analyzed SEM images of the top surface of our epi-structures after etch pit formation: (a) reference sample, and ELOG samples with (b) 4 μm, (c) 7 μm, and (d) 10 μm wide stripes. After [70].

In addition, we performed PL measurements using our setup containing a He-Cd laser at 325 nm, an optical microscope with a high magnifying power (100×) objective lens and a motorized stage, a monochromator, and a broadband photodetector. We carefully set the position and spot size (~2 μm) of the incoming laser beam properly such that all photons that contribute to the PL signal come from the low dislocation density region of the epitaxy. PL spectra

corresponding to the reference sample and the ELOG samples are given in Figures 3.11(a)–(d).

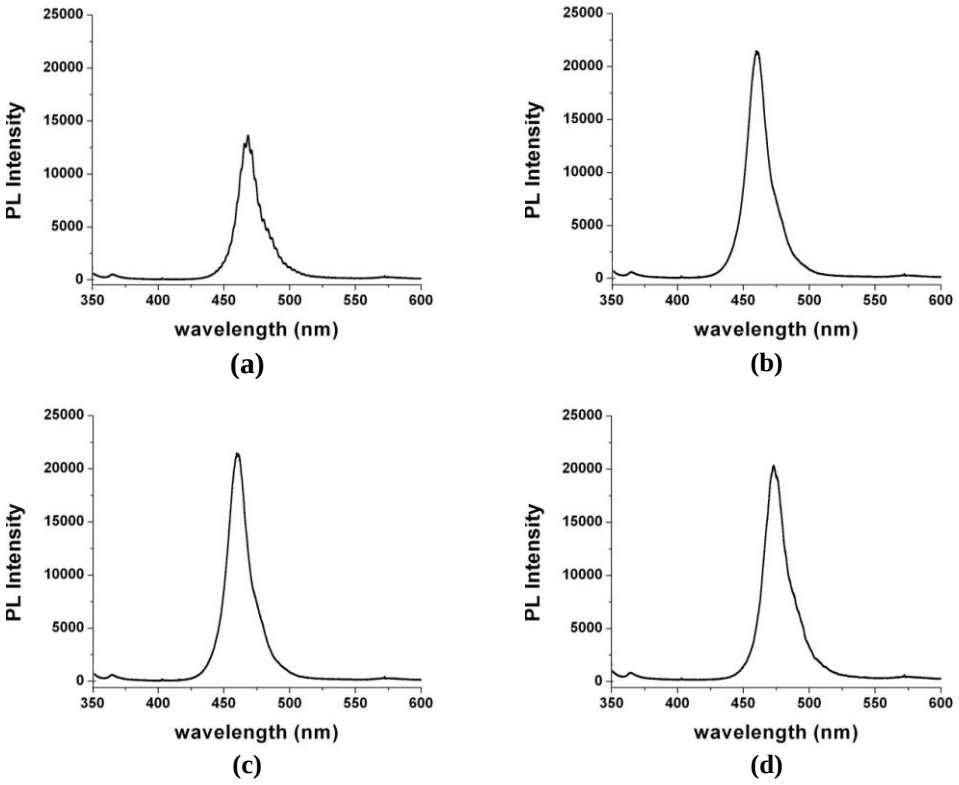

Figure 3. 11 PL spectra of (a) reference sample, and ELOG samples with (b) 4 µm, (c) 7 µm and (d) 10 µm wide stripes. After [70].

As a result of our PL measurements, we found that the PL peak emission wavelengths (λ_{PL}) were in the range of 466 ± 7 nm. This confirms that the levels of InN incorporated in the well regions of the MQW layers were similar to each other. Specifically, the structure with 4 µm wide stripes emit at the shortest wavelength, λ_{PL}, with the highest peak intensity, I_{PL}. Moreover, the FWHM of the PL spectra, $\Delta\lambda_{PL}$, was the lowest for the reference sample (18.47 nm), and very close to the sample with 4 µm stripes (18.53 nm). These results indicate that the reference sample exhibits the weakest photoluminescence. (All important parameters of these PL spectra, which will later be discussed again and compared with other characterization results, are further summarized in Figures 3.15(a), 3.15(c) and 3.15(e) **[70]**.

Moreover, we performed TRPL measurements for studying the carrier generation rate in the quantum structures. We used PicoQuant TRPL setup comprising an InGaN-based laser diode operated at 375 nm in pulsed mode, with the monochromator center wavelength set at 466 nm in the photon collection side, for all of the samples. The details on the TRPL measurements and the setup will further be provided in Chapter 5, where we will discuss electric field dependent carrier lifetimes in InGaN/GaN quantum structures.

We fit the decay curves with three exponentials to obtain the minimum deviation from the actual data and considered the carrier recombination rates, R_i, as the reciprocal of the intensity averaged lifetimes, τ_i^{-1}. We present the experimental TRPL decay curves of the four structures along with their numerical fits in Figure 3.12.

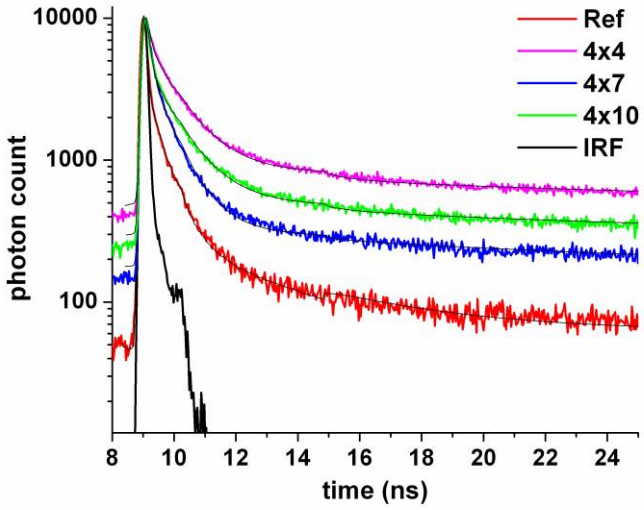

Figure 3. 12 Time-resolved photoluminescence decay profiles of our epitaxial lateral overgrowth structures and the reference sample along with their corresponding fits. The fastest decay profile corresponds to the reference sample due to its higher dislocation density, and thus higher nonradiative recombination rate. After [70].

The extracted recombination rates correlate well with the dislocation density levels in our epi-structures, considering the fact that the dislocations form nonradiative recombination centers, increasing the nonradiative recombination rate and, thus, the overall recombination rate. As a result, the recombination rates, measured using TRPL, should exhibit a similar trend with the dislocation

densities, at least when the dislocation densities are significantly different, which is the case for the reference sample and the ELOG sample with 4 μm wide stripes, as shown in Figures 3.13(a) and 3.13(b). These results are also consistent with the previous theoretical **[71]** and experimental **[72]** studies.

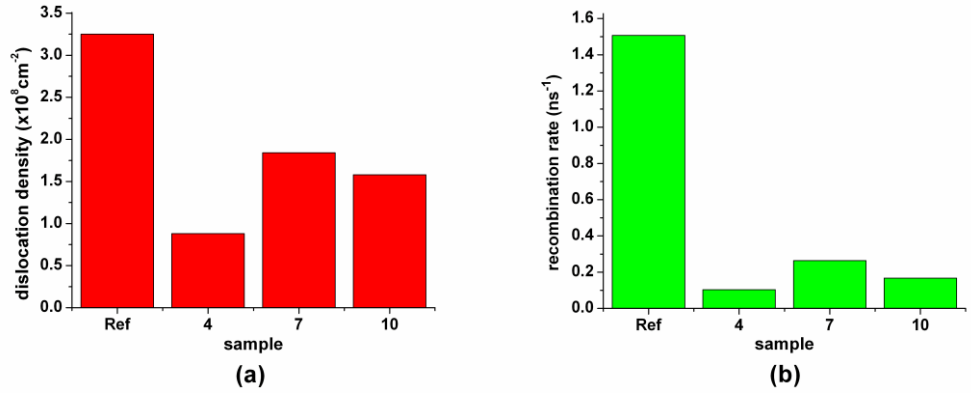

Figure 3. 13 Comparison of (a) dislocation densities measured by SEM analysis and (b) recombination rates of our structures measured by TRPL analysis. After [70].

Device Characterization

We further performed photocurrent measurements at different levels of reverse bias applied across our devices. Our photocurrent setup consists of a Xenon lamp, monochromator, optical chopper, DC power supply and a lock-in amplifier. Using an optical beam spot size of ~200 μm illuminating the device under test, we control the measurement parameters (e.g., wavelength of the incoming light and the bias voltage applied) and read the photocurrent data through a GPIB interface.

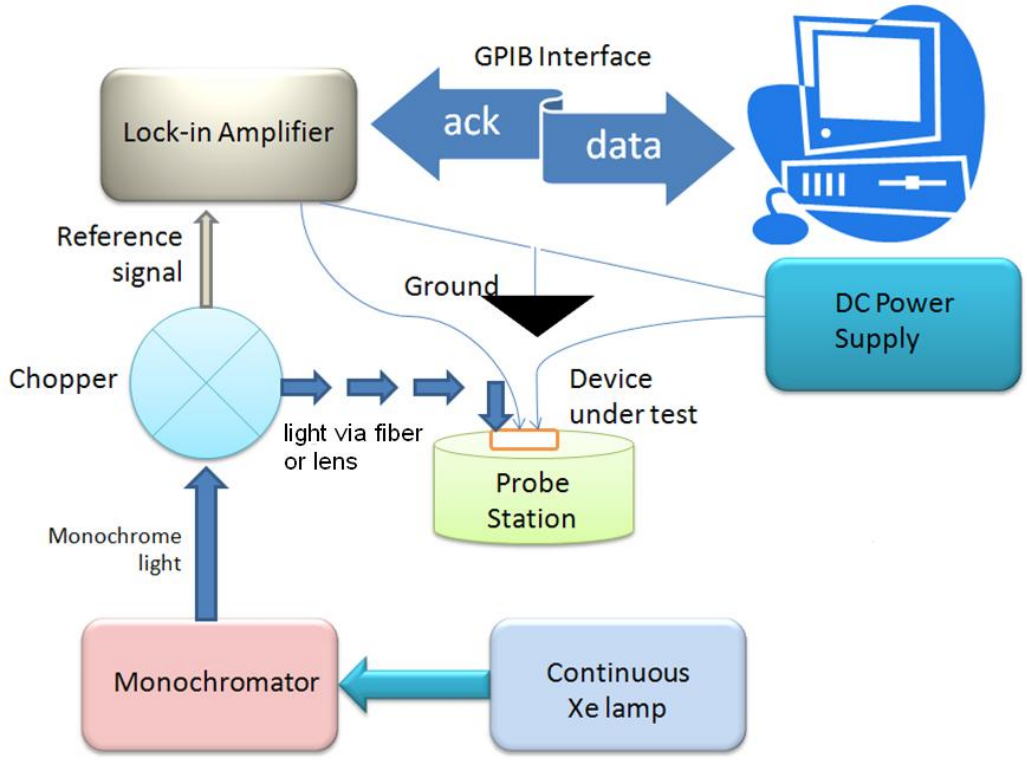

Figure 3. 14 Schematics and flow chart of our photocurrent measurement setup.

Due to the partial compensation of the polarization-induced electrostatic fields inside the well layers by the external electric field, we observed a blue shift of the absorption edge and thus, a decrease in the absorption level around the band edge, with increasing external bias. Such an electroabsorption behavior, called reversed quantum-confined Stark effect, has been observed previously **[57], [73]**. In this study, we consider the photocurrent change at 4 V with respect to 0 V absorption levels, $\Delta i_{ph}(\lambda)$. In the wavelength interval where the blue shift is observed, this gives a figure of merit for comparative electroabsorption performance of these devices. Here, we define the maximum photocurrent change, i.e., $\max[-\Delta i_{ph}(\lambda)]$, over the operating wavelength range, which is related to the electroabsorption performance. Also, the wavelength at which this maximum occurs can be considered as the electroabsorption modulator optimal operating wavelength of the corresponding sample, λ_{EA}. This wavelength where the absorption changes the most via the externally applied electric field is expected to follow the same trend as λ_{PL} for all samples. The related FWHM ($\Delta\lambda_{EA}$) can also be defined as the

operation wavelength range, over which the quantum electroabsorption behavior is observed. This quantum effect should correlate correspondingly with the broadening of the PL emission of our quantum structures, since they both are related to the bound states near the bandgap.

In Figures 3.15(a) and 3.15(b), we show the PL peak wavelength (λ_{PL}) and the maximum absorption change wavelength (λ_{EA}) for our epitaxial lateral overgrowth samples, which are consistent with each other. As seen in Figure 3.15(c) and 3.15(d), $\Delta\lambda_{EA}$ also follows the FWHM of PL emission ($\Delta\lambda_{PL}$). Moreover, the level of maximum photocurrent change with the voltage swing from 4 to 0 V, max[$-\Delta i_{ph}(\lambda)$], and the PL peak intensity levels, I_{PL}, follow a similar trend, except for a small variation in PL intensities of the samples with 7 and 10 μm stripe widths. Also, all these trends correlate well with the carrier lifetimes and the dislocation densities mentioned earlier **[70]**.

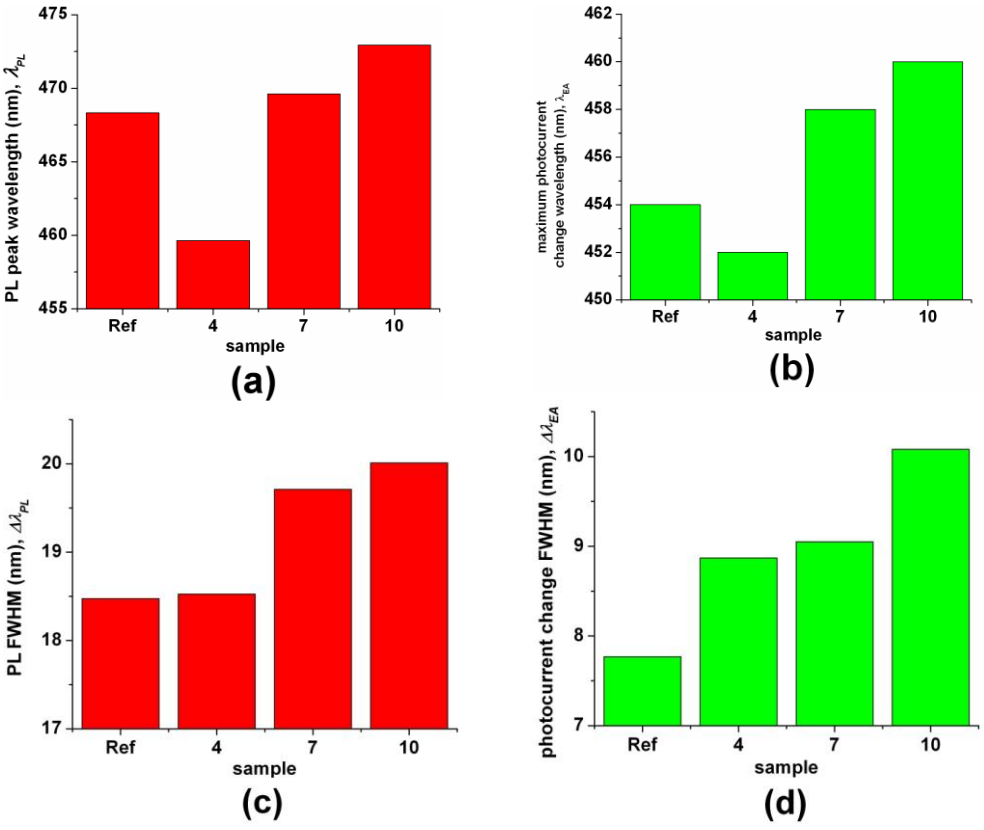

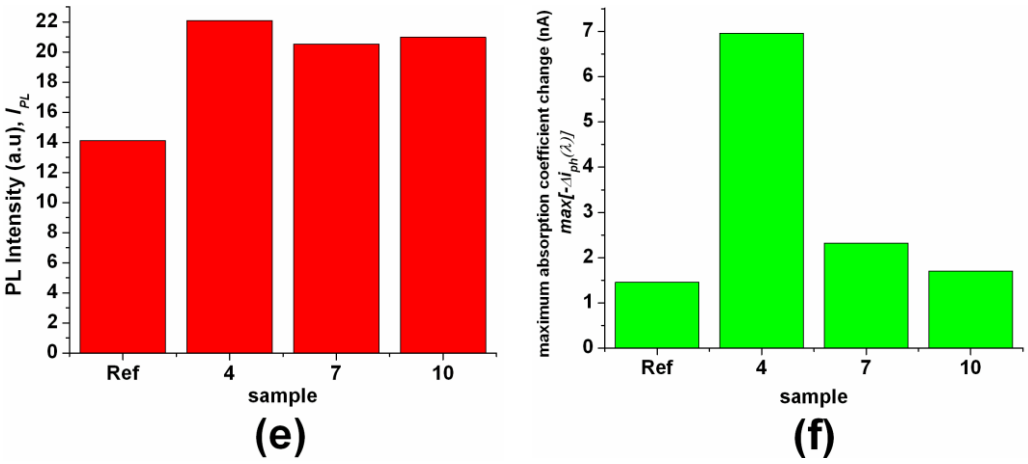

Figure 3. 15 Comparison of similar trends in (a) PL peak wavelengths and (b) maximum photocurrent change (electroabsorption) wavelengths; (c) PL peak FWHMs and (d) electroabsorption FWHMs; and (d) PL peak intensities and (e) maximum photocurrent change among our structures. After [70].

In our experimental measurements, we consistently observe that the lower dislocation density leads to stronger electroabsorption, although this dependence of electroabsorption on dislocation density may not be obvious for those who are more familiar with photoluminescence (e.g., LEDs). As an important remark, our results suggest that the electroabsorption performance of the best performing ELOG structure (4 μm stripe width) is about 3-fold better than its nearest competitor (7 μm stripe width). This performance difference of EA is significantly larger than the ratio of their corresponding PL intensities. Furthermore, this strong electroabsorption is 4.8-fold larger than the Reference sample without ELOG. We attribute the observed strong dependence of electroabsorption performance on dislocation density to higher quality quantum well layers with more uniform thickness and more abrupt interfaces in lower dislocation density samples. Also, considering the fact that strain-induced piezoelectric polarization fields (and thus the total polarization-induced electrostatic fields) inside the well layers bend the conduction and valence bands of the low dislocation density samples more compared to others, they have a narrower effective bandgap, which causes a red shift in the emission and absorption of the c-plane grown polar InGaN/GaN quantum structures. As a result, the 4 μm ELOG sample's shortest emission wavelength can be explained

by its lower amount of the residual strain **[74], [75]**, which is released at the coalescence sidewalls more compared to other samples. Since this sample has more stripes, there are more coalescence sidewalls available per unit area **[70]**.

3.3 Summary

In summary, the electroabsorption performance is found superior for the ELOG InGaN/GaN quantum structures (with 4 μm ELOG mask stripes) because of its higher crystal quality and a lower level of residual strain compared to the reference without ELOG. Electroabsorption performance of this sample is much significantly stronger than those of the others, as compared to the difference measured in their PL intensities. The electroabsorption operation wavelengths are observed to follow closely their PL peak wavelengths; the same is also true for the case of their spectral widths. Here the results deduced from different and independent experiments are found in good agreement. The experimental results also indicate that the electroabsorption performance and simultaneous emission rates follow similar trends with the crystalline quality and the level of strain released in the coalescence sidewalls. ELOG, with reduced levels of dislocation density, offers an effective approach for achieving strong electroabsorption in InGaN/GaN quantum structures.

Chapter 4

Electroabsorption of InGaN/GaN Quantum Structures

In this chapter, we present our work on external electric field dependent optical absorption in InGaN/GaN quantum structures. We start with our comparative study of electroabsorption modulators comprising InGaN/GaN quantum structures with different well and barrier thicknesses and InN molar ratios in the quantum wells. Our results indicate that electroabsorption performances improve with decreasing built-in electrostatic field in the quantum well layers. In the second part of the chapter, we present our work on electroabsorption in polar and nonpolar InGaN/GaN quantum structures. Due to polarization induced electrostatic fields in polar GaN, we observe a blue shift of the absorption edge with increasing external electric field, whereas for nonpolar GaN, we observe a red shift of the absorption edge.

4.1 Comparative study of electroabsorption in InGaN/GaN quantum structures

This section is based on the publication *"Comparative study of electroabsorption in InGaN/GaN quantum zigzag heterostructures with polarization-induced*

electric fields" by E. Sari, T. Ozel, A. Koc, J.-W. Ju, H.-K. Ahn, I.-H. Lee, J.-H. Baek, and H. V. Demir, *Applied Physics Letters* 92, 201105 (2008). Reproduced with permission from American Institute of Physics.

Here, we present a comparative study of InGaN /GaN quantum zigzag structures embedded in p-i-n diode architecture that exhibit blue-shifting electroabsorption in the blue when an electric field is externally applied to compensate for the polarization-induced electric field across the wells. With the polarization breaking their symmetry, the same InGaN/GaN quantum structures redshift their absorption edge when the external field is applied in the same direction as the well polarization. Both computationally and experimentally, we investigate the effects of polarization on electroabsorption by varying compositional content and structural parameters and demonstrate that electroabsorption grows stronger with weaker polarization in these multiple quantum well (MQW) modulators.

An important, distinctive property of III-Nitride quantum heterostructures is the formation of strong polarization when they are grown on the c-plane of their wurtzite crystal structure. Due to the discontinuity of polarization with abrupt compositional changes at the heterointerfaces of such III-Nitride MQWs, large electrostatic fields in alternating directions are induced across the well / barrier pairs. As a result, the band structure of these MQWs yields zigzag potential profiles in conduction and valence bands instead of conventional square potential profiles **[18]**. This substantially alters electric field dependence of optical absorption in III-Nitride MQW structures **[57]**.

Electroabsorption measurements are also essentially informative to understand the underlying physics behind such polar III-Nitride structures. We previously demonstrated a quantum electroabsorption modulator based on InGaN/GaN quantum zigzag structures operating in the blue **[57]** and in the near-ultraviolet **[68]**. In the previous work of our group and others, however, the effect of polarization on electroabsorption in polar InGaN / GaN has not been comparatively studied or systematically investigated.

In this study, we present the design, growth, fabrication, experimental characterization, and theoretical analysis of InGaN/GaN quantum zigzag structures with different levels of polarization-induced electrostatic fields that are set by controlling the alloy content and well-to-barrier width ratio. We comparatively study the effects of polarization-induced electrostatic field on the performance of our quantum electroabsorption modulators and develop a better understanding to design devices for stronger electroabsorption.

For our comparative study, we designed three sets of InGaN/GaN quantum structures incorporated in a p-i-n diode architecture. Among these sets, the structural parameters of their active regions were carefully selected for comparison purposes. These structural parameters include InN concentrations in the quantum well regions and well-to-barrier width ratios. We used a generic p-i-n epitaxial design for these three sets of samples (samples A, B, and C). In our design, we included five quantum well/barrier pairs for all of the structures. Sample A was designed to have an active MQW layer of 2.5 nm/7.5 nm $In_{0.15}Ga_{0.85}N$/GaN quantum well/ barrier structures. Sample B has the same structure with 3nm/4nm $In_{0.15}Ga_{0.85}N$/GaN and Sample C with 3nm/4nm $In_{0.12}Ga_{0.88}N$/GaN. These epistructures were designed to study only the polarization effect varied through these two parameters. Using the design and material parameters of GaN and InN, we calculate built-in electrostatic fields inside the well and barrier layers of samples A, B, and C. Using the equation that relates material and design parameters to polarization-induced electric field across the wells, we set $\mathbf{E_{well}}$ to be -383 V/μm for sample A, -300 V/μm for sample B, and -238 V/μm for sample C, while those across the barriers were set to be 127 V/μm for sample A, 220 V/μm for sample B, and 179 V/μm for sample C.

We grew these epitaxial structures using an MOCVD system on c-plane sapphire substrates. We used exactly the same conditions for the epitaxial growth of all samples except for their active layers. We tuned InN incorporation into the MQW layers by changing the growth temperature and their layer thickness by changing

the growth time of each layer. Detailed growth conditions can be found elsewhere. Following the epitaxial growth, we fabricated diode mesas with electrodes using reactive ion etching, p and n-contact metallization, and annealing steps.

The three samples in this work were all fabricated using our standard semiconductor processes and then characterized under the same conditions. We performed photoluminescence (PL) and double crystal X-ray diffraction (DCXRD) measurements to verify the growth of the desired quantum structures with the intended alloy content and high crystal quality. PL spectra for these samples were obtained using a He–Cd laser at an excitation wavelength of 325 nm. PL peaks at 450, 450, and 425 nm for samples A, B, and C, respectively, verifing the growth of the InGaN quantum wells within 1.5% of the desired InN ratio.

Together with the experimental verification of the structural parameters and the calculated built-in electrostatic fields, we obtained full band diagram of the grown InGaN/GaN quantum zigzag structures, with a potential profile tilting in one direction in the wells and in the other direction in the barriers. We developed a transfer matrix method for the numerical analysis of these quantum structures. Using our computational tool, we computed ground state electron and heavy hole eigenstates and energy eigenvalues along with the squared overlap integral of $\langle e1|h1\rangle$ proportional to the absorption strength under different levels of external electric field. Traditional quantum-confined Stark effect yields only red shift, independent of the direction of the applied electric field.

For all of our samples (samples A, B, and C) with the increasing external electric field, when it is applied in the opposite direction of the polarization-induced electric field across the wells, we computationally prove that the absorption edge blueshifts. In this case, the external field compensates for the internal field in the wells. However, when the external field is applied in the same direction as the polarization in the wells, the same InGaN/GaN quantum structures redshift their absorption edge. The co-observation of these blue and red shifts in the

electroabsorption of the same quantum structures is impossible in nonpolar quantum heterostructures, which are completely indifferent to the direction of the applied field. In the case of such polar III-N quantum heterostructures, the polarization breaks their symmetry and thus, the direction of the applied field matters. Our theoretical results predict absorption coefficient changes with the ratios of 0.4 around λ=450 nm for sample A, 0.53 around λ=440 nm for sample B, and 1.0 around λ=420 nm for sample C with a field swing of 40 V/μm. Therefore, sample C, which features the weakest polarization, is theoretically predicted to exhibit the strongest electroabsorption.

In electroabsorption measurements, by chopping the incident optical beam and monitoring the photocurrent with a lock-in amplifier at the chopping frequency, we observe a blue shift of the absorption edge with the application of reverse bias, which generates an electric field opposite to the polarization induced electrostatic fields in the wells. Figures 4.1–4.3 show optical absorption spectra around the corresponding operating wavelengths for each of the sample (samples A, B, and C, respectively). Additionally, in insets (a) of Figures 4.1–4.3, we present the absorption coefficient change with respect to the 0 V absorption curve for each sample.

Our analysis of absorption coefficient change reveals that we obtain a maximum absorption coefficient change of 288 cm^{-1} at λ=440 nm for sample A, 462 cm^{-1} at λ=434 nm for sample B, and 555 cm^{-1} at λ=422 nm for sample C, which are all obtained by a 0–4 V swing (for a field change of 40 V/μm). These correspond to the relative ratios of 0.52 at 440 nm for sample A, 0.83 at 434 nm for sample B, and 1.0 at 422 nm for sample C.

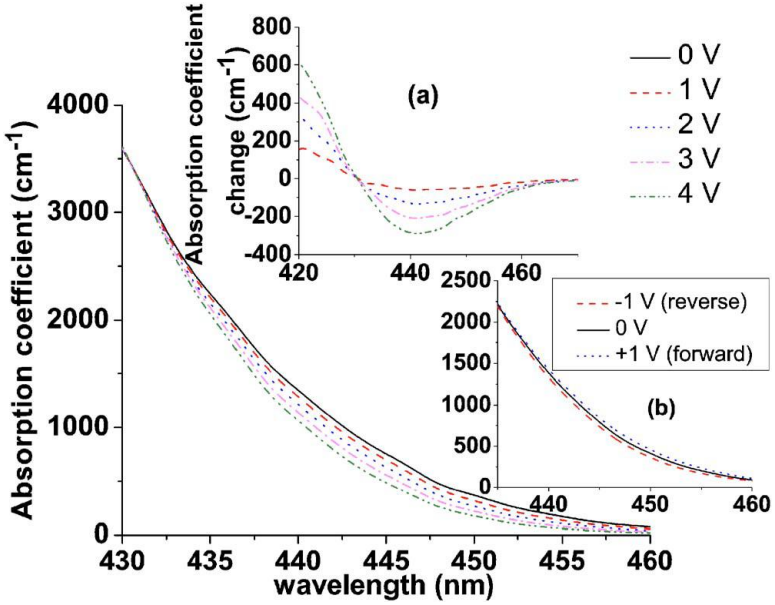

Figure 4. 1 Electroabsorption spectra of sample A under different bias voltages. The inset (a) shows the absorption coefficient change for sample A with respect to the 0 V absorption curve and the inset (b) depicts the absorption spectra of sample A for 0, −1, and +1 V bias voltages. After [19].

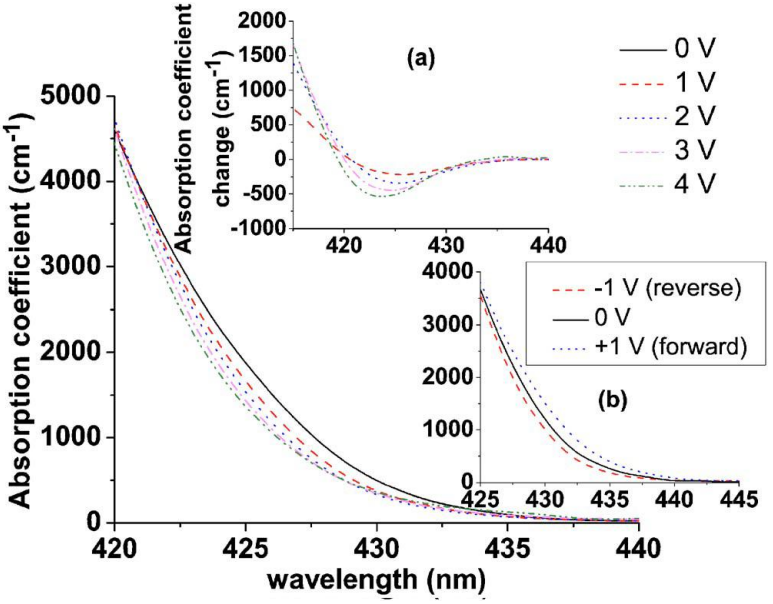

Figure 4. 2 Electroabsorption spectra of sample B under different bias voltages. The inset (a) shows the absorption coefficient change for sample B with respect to the 0 V absorption curve and the inset (b) depicts the absorption spectra of sample B for 0, −1, and +1 V bias voltages. After [19]

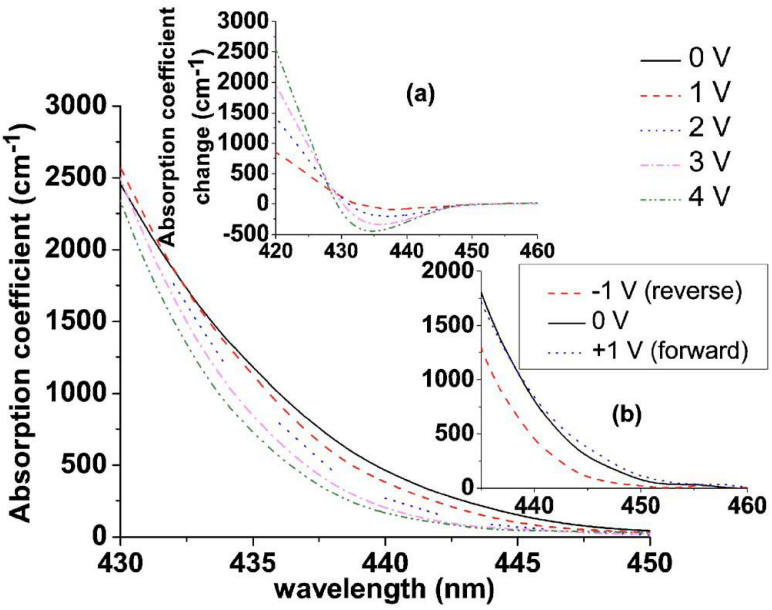

Figure 4. 3 Electroabsorption spectra of sample C under different bias voltages. The inset (a) shows the absorption coefficient change for sample C with respect to the 0 V absorption curve and the inset (b) depicts the absorption spectra of sample C for 0, −1, and +1 V bias voltages. After [19].

These experimental results are in good agreement with our computational results. Experimentally, sample C, which has the weakest polarization, exhibits the largest absorption change, which is in agreement with the theoretical prediction. The electroabsorption improves with decreasing built-in electrostatic field inside the wells. Additionally, insets (b) of the respective electroabsorption figures of samples A–C (Figures 4.1–4.3) also present the absorption curves under 0 V, -1 V (in reverse bias), and 1 V (in forward bias). While the current levels in the forward bias at 1 V and in the reverse bias at -1 V are similar, the electric field generated at 1 V and -1 V is completely opposite in direction. This change in the electric field direction then reverses the shift of the absorption edge from blue shift to red shift. This behavior is unique to polar quantum heterostructures, which is both predicted by our theoretical computations and verified by our experimental characterization.

4.2 Opposite electroabsorption behavior in polar *vs*. nonpolar InGaN/GaN quantum structures

This section is based on the publication *"Opposite carrier dynamics and optical absorption characteristics under external electric field in nonpolar vs. polar InGaN/GaN based quantum heterostructures,"* by E. Sari, S. Nizamoğlu, J.-H. Choi, S.-J. Lee, K.-H. Baik, I.-H. Lee, J.-H. Baek, S.-M. Hwang, and H. V. Demir, Optics Express 19, 5442 (2011). Reproduced with permission from Optical Society of America.

As mentioned in earlier chapters, III-Nitride quantum heterostructure epitaxy (e.g., quantum wells/barriers) exhibits high polarization-induced electrostatic fields, due to the discontinuity of their net polarization fields (i.e., the vector sum of their spontaneous and piezoelectric components) when grown in the so-called "polar" direction on c-plane. In such polar heterostructures, the polarization-induced electric field inside the well region pulls the bound electron and hole in opposite directions. This reduces their wavefunction overlap and in turn reduces their oscillator strength and thus their radiative recombination rate. This makes the polar III-Nitrides less favorable for light generation in device applications including light-emitting diodes and laser diodes. Therefore, it is highly desired to obtain GaN epitaxy on other planes of its unit cell, where there is no polarization discontinuity in quantum well structures. This is, however, technically challenging.

Such polarization-free (nonpolar) planes are m- and a-planes of the GaN's wurtzite crystal **[27]**. To date, many techniques have previously been proposed for obtaining high-quality nonpolar GaN crystals **[22]**. Also, LEDs **[24], [27]** and LDs **[76]–[78]** have been demonstrated using these techniques. Very few of these prior works involved a feasible and efficient process. In a very recent work, Hwang *et al.* **[26]** made it possible to grow a-plane GaN on r-plane sapphire by reducing defect densities through a high temperature nucleation layer process and demonstrated working light-emitting diodes incorporating these nonpolar

InGaN/GaN quantum structures. Metal-organic chemical vapor deposition (MOCVD) technique was used, while avoiding the need for growing on a very thick (>10 μm) GaN template, different than some of the previous studies **[24]**.

The quantum heterostructures studied in this work were epitaxially grown on r-plane and c-plane sapphire substrates, both using MOCVD as described elsewhere, previously **[1], [26]**. They were incorporated in a p-i-n diode architecture, and their n-type layer was on the bottom while their p-type layer was on the top. These epi-structures included two 7 nm thick $In_{0.20}Ga_{0.80}N$ quantum wells separated by a 12 nm GaN barrier in the nonpolar case and five 2.5 nm thick $In_{0.18}Ga_{0.82}N$ quantum wells separated by 7.5 nm GaN barriers in the polar case. Although these multi-quantum well structures are slightly different, they are essentially the same type of uncoupled quantum structures, with their peak photoluminescence emission wavelengths close to each other, both exhibiting strong emission around λ~500 nm. Moreover, for both structures, the electron concentrations throughout the active (multiple quantum well) region were approximately $4x10^{17}$ cm^{-3}. Subsequent to their epitaxial growth, the devices were fabricated in a clean room environment using the same standard lithography, reactive ion etching and metal evaporation/sputtering steps. The devices were then diced and wire-bonded to metal can packages for compact and reproducible device characterization.

The photoluminescence spectra of our quantum structure samples were measured using a He-Cd laser to pump at an excitation wavelength of 325 nm and a spectrometer to collect the emission signal. From these PL spectra, using Gaussian fitting procedure, a peak emission wavelength at 514 nm with a full width at half maximum (FWHM) of 43.1 nm for the nonpolar heterostructure on a-plane and a peak wavelength of 491 nm with a FWHM of 37.5 nm for the polar heterostructure on c-plane were obtained. Their measured photoluminescence and electroluminescence spectra are shown in Figure 4.4 and 4.5, respectively.

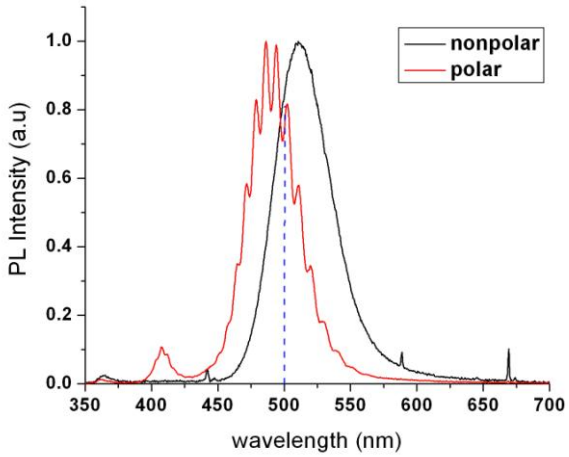

Figure 4. 4 Normalized photoluminescence spectra of our InGaN/GaN based polar and nonpolar quantum heterostructures at room temperature. After [79].

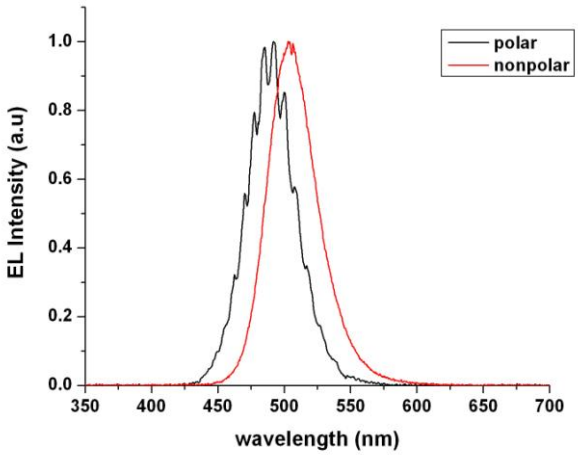

Figure 4. 5 Normalized electroluminescence spectra of our devices based on polar and nonpolar InGaN/GaN quantum heterostructures, both measured at a constant driving current of 20 mA at room temperature. After [79].

We also comparatively investigated the external field dependent optical absorption in our polar and nonpolar InGaN/GaN based devices through photocurrent measurements. We measured the photocurrent both in our polar and nonpolar devices around the wavelength of their absorption edges at different reverse bias levels at room temperature. Here shown in a semilog plot of the photocurrent spectra in Figure 4.6, the polar device exhibits a blue-shifting

absorption edge with the applied field due to reversed quantum-confined Stark effect.

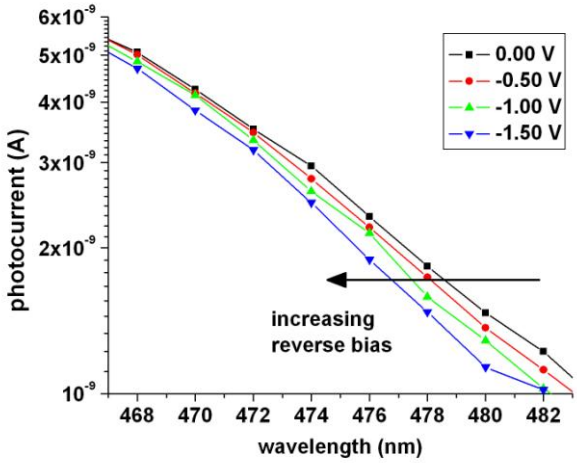

Figure 4. 6 Photocurrent spectra of our device based on polar InGaN/GaN quantum heterostructures. The arrow indicates the blue shift of the absorption edge with the increasing reverse bias. After [79].

In the opposite manner, for the nonpolar structure, we observe a red-shifting trend of the absorption edge, as a result of quantum-confined Stark effect **[42]** that manifests itself as in other III-V systems such as InP/GaAs **[42]–[45]** as in Figure 4.7.

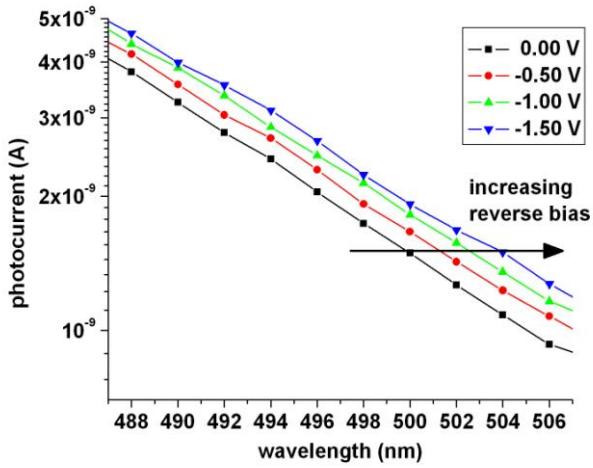

Figure 4. 7 Photocurrent spectra of our device based on nonpolar InGaN/GaN quantum heterostructures. The arrow indicates the red shift of the absorption edge with the increasing reverse bias. After [79].

Due to the narrower bandgap of the quantum well material, here for the nonpolar quantum structures the absorption edge is at longer wavelengths, around λ~500 nm.

In summary, we presented the opposite external electric field dependence of optical absorption characteristics in c-plane grown polar vs. a-plane grown nonpolar InGaN/GaN quantum heterostructures. We showed the blue shift of the absorption edge in polar quantum heterostructures and the red shift of the absorption edge in nonpolar heterostructures. We explained this opposite behavior of electroabsorption in the context of quantum-confined Stark effect.

4.3 Summary

In summary, we presented our works on electroabsorption in InGaN/GaN quantum structures throughout this chapter. We started with our comparative study on electroabsorption in InGaN/GaN quantum structures with three different structural parameters, to set $\mathbf{E_{well}}$ values ranging from -383 V/μm to -238 V/μm. Within the range of these field strengths, we studied its effect on the electroabsorption performance. Our TMM based computational analyses and experimental results were found to be in agreement and show that the electroabsorption performance is superior in the structure with the lowest set $\mathbf{E_{well}}$ strength.

In the second part of this chapter, we examined the opposite electroabsorption behavior of polar and nonpolar InGaN/GaN quantum structures. We showed that absorption edge of polar structures blue shift, whereas that of the nonpolar structures red shift. Quantum-confined Stark effect manifests itself in opposite ways in polar and nonpolar InGaN/GaN quantum structures.

Chapter 5

Electric field dependent carrier dynamics in InGaN/GaN quantum structures

In this chapter, we present our results on carrier dynamics in InGaN/GaN quantum heterostructures in response to the externally applied electric fields. We first investigate the external electric field dependence of radiative recombination lifetimes. We continue with our work on carrier dynamics in polar *vs.* nonpolar InGaN/GaN quantum structures and show that they behave in an opposite manner in response to the external electric field in a way consistent with Fermi's golden rule.

5.1 Electric field dependent radiative carrier dynamics in InGaN/GaN quantum structures

This section is based on the publication *"Electric field dependent radiative decay kinetics of polar InGaN/GaN quantum heterostructures at low fields,*" E. Sari, S.

Nizamoğlu, I-H. Lee, J-H. Baek and H. V. Demir, *Applied Physics Letters* 94, 211107 (2009). Reproduced with permission from American Institute of Physics.

Here, in this part of the thesis, we present our systematic investigation on determining relative changes in radiative recombination lifetimes of polar InGaN/GaN quantum heterostructures in response to the applied electric field. In our study, the external electric field levels that we applied across the quantum structures is in opposite direction to and one order of magnitude less than the calculated polarization-induced built-in electric field inside the quantum well layers ($\mathbf{E_{well}}$ = 190 V/μm). The maximum applied electric field is limited by the photoluminescence (PL) optical output power levels that are detectable in our experimental setup. On the other hand, the applied field is in the same direction and of the same order of magnitude as the polarization field in the barrier layers ($\mathbf{E_{barrier}}$ = 70 V/μm). At these external field levels, our experimental results reveal a decrease in internal quantum efficiencies (QEs), carrier lifetimes, and radiative recombination lifetimes with increasing field, as verified consistently with steady state and transient PL measurements of these polar quantum structures.

For our investigation, we grew an InGaN/GaN quantum heterostructure embedded in a p-i-n diode architecture on c-plane sapphire substrate by using metal-organic chemical vapor deposition. The epitaxial design was developed for a light-emitting diode operating at 448 nm. Its active layers included five periods of 2.5 nm thick $In_{0.15}Ga_{0.85}N$ quantum well and 7.5 nm thick GaN barrier layers grown in the intrinsic region of the epitaxy. Surrounding the intrinsic layer are the n-type (Si:GaN) and p-type (Mg:GaN) layers grown with their targeted doping concentrations of 5×10^{18} and 8×10^{17} cm^{-3} and thicknesses of 2 and 0.2 μm, respectively. This design allows for partially compensating for the polarization-induced electrostatic field inside the well layers in reverse bias operation. For the application of external electric field, standard mesa and electrode fabrication cycles were implemented. Reactive ion etching and metallization steps were followed by dicing and transistor outline (TO) packaging of 300×300 μm^2 devices. For Ohmic contact formation to n-type (bottom) layer 10/200 nm Ti/Al

was used, whereas for p-type (top) layer, a 100 nm thick indium tin oxide (ITO) was used to obtain optically semitransparent windows. These ITO based semitransparent contacts enabled a uniform application of the electric field across the active layers while maintaining a low optical loss for the incident light due to its low background absorption. On top of ITO, a 10/100 nm Ti/Au layers were further used to make strong Au wire bonds to the TO can.

We performed time resolved PL measurements (using PicoQuant PicoHarp 300) at room temperature to determine the electric field dependence of decay kinetics. The optical apparatus consists of a commercially available InGaN/GaN based near-ultraviolet (375 nm) laser diode used in pulsed mode operation, a monochromator, a photomultiplier tube, a high speed photodetector, and controller electronics as depicted in Figure 5.1 below.

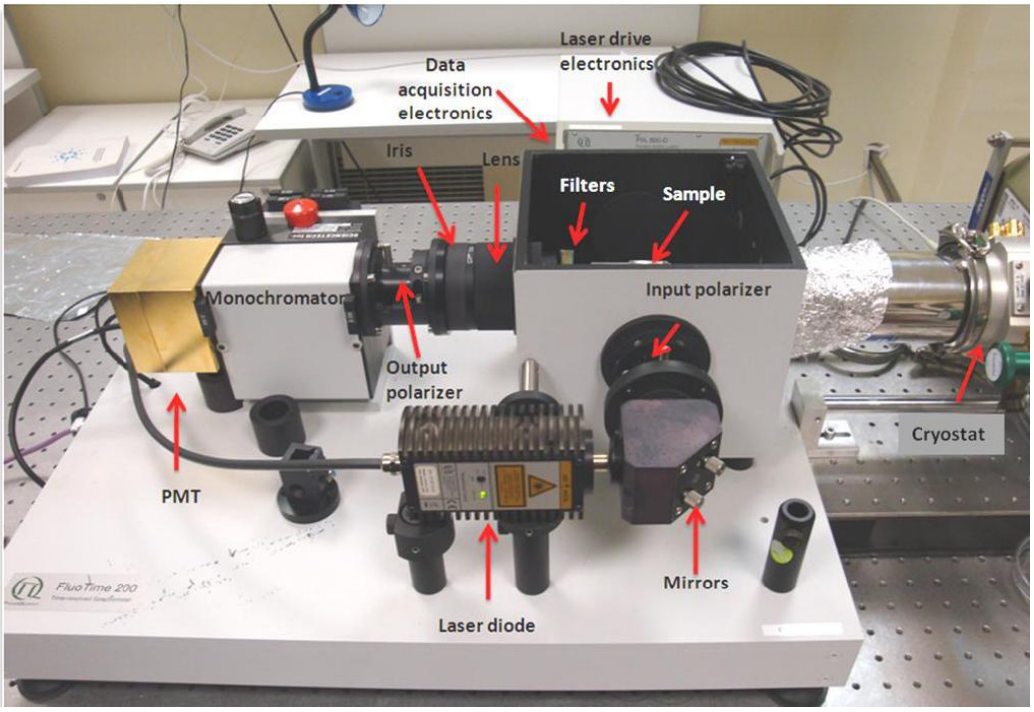

Figure 5. 1 FluoTime 200 TRPL setup at our Lab.

In Figure 5.2 we show the TRPL spectra of our polar InGaN/GaN quantum structure under different levels of externally applied electric field. Here we are interested in the photoluminescence decay of photons whose energies correspond to the transition energy between the electron and hole ground states. This photon

energy is 2.76 eV, corresponding to 448 nm, the peak electroluminescence wavelength.

These experimental photoluminescence decays are numerically further analyzed by deconvolving the input pulse (instrumental response function) and using three best fitting exponential decays in the fluorescence decay analysis software of Pico-Quant (FLUOFIT). This numerical curve fitting procedure leads to the retrieval of intensity-averaged lifetime for our detailed understanding of carrier lifetime (τ) behavior, with a chi-square (χ^2) error 1.0±0.05 for each PL decay at a particular field level. In these analyses, the levels of χ^2 error were sufficiently close to unity to achieve accurate enough representation using triple-exponential decays, each with a single lifetime. In the inset of Fig. 4.4, we present the change of carrier lifetime under 0–1.25 V reverse bias voltages, corresponding to 0–12.5 V/μm electric field swings. The strong electric field dependent decrease of carrier lifetime is in agreement with the previous work of Jho *et al.* **[80]** on carrier dynamics. The rate of change of carrier lifetime monotonically decreases with increasing field from 0.91 ns/V/μm (for 0–2.5 V/μm field swings) to 0.23 ns/V /μm (for 10–12.5 V/μm field swings).

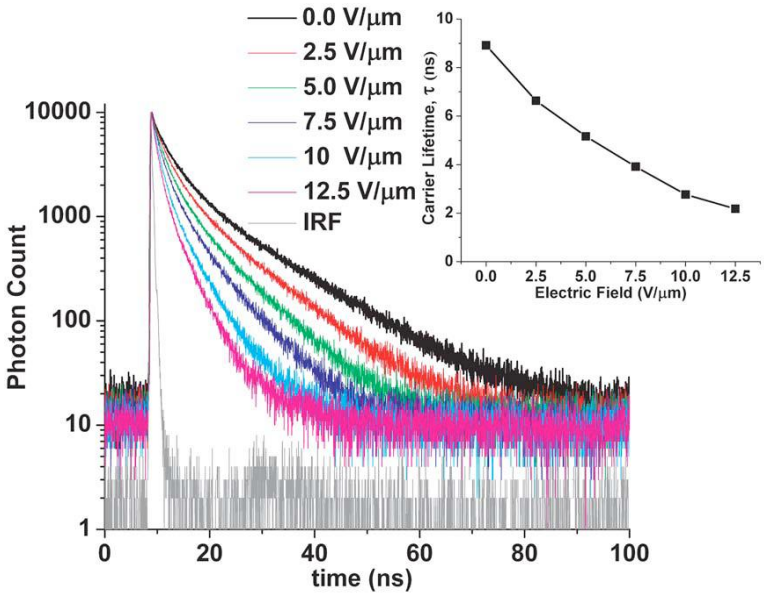

Figure 5. 2 TRPL decay curves of our polar InGaN/GaN quantum heterostructure under different electric field levels. The inset shows the carrier lifetime vs. applied electric field as a result of the TRPL analysis. After [73].

We believe such strong dependence of carrier lifetime on the external electric field originates from its nonradiative component for the most part, due to relatively low QE (< 10%).

The radiative component (τ_r) of the overall PL decay is related to the QE as given in Eq. (5.1). In addition to the carrier lifetime measurements, to determine the electric field dependence of τ_r, we performed steady state PL measurements. This PL characterization was carried out on the same device, under the same external electric field levels, using a continuous-wave He–Cd laser as the excitation source operating at a wavelength of 325 nm and collected via a UV-visible photodetector placed after a high resolution monochromator. Here, since we consider only relative QEs, it is important to make sure that the experimental conditions are identical for different external electric field levels. Also, as apparent from the constant fringe periods in the PL spectra, the refractive index change due to electro-optic effect is insignificant at the applied electric field levels, making it possible to ignore the effect of extraction efficiency on relative QEs in our analyses. Also, since the external electric field builds up across the intrinsic (i) region of our epitaxial structure, it is only the i-region where optical processes are affected by the applied electric field in our experiments. Hence, optical absorption taking place in other layers is assumed to be unaffected from the external field change in our analyses.

$$\mathrm{QE}(E) = \frac{N_e(E)}{N_a} \propto \frac{\tau(E)}{\tau_r(E)}. \tag{4.1}$$

The electric field dependent steady state PL measurement results are given in Figure 5.3. The PL spectra exhibit narrowed linewidths particularly over the longer wavelength part of the spectra shifting with the applied field due to partial compensation of polarization-induced built-in electric field inside the well layers. The normalized PL spectra depicted in Figure 5.4 clearly show this blueshift at the longer wavelengths as a result of the reversed quantum-confined Stark effect.

This is an apparent sign that electric field dependence of transition energy between the ground state electron and hole wavefunctions $\langle e1|H|h1\rangle$ is stronger than those between higher order states. From the definition of QE given in Eq. (5.1), we understand that the QE decreases with decreasing number of emitted photons (N_e) in response to increasing external electric field, assuming that the application of electric field does not change the number of absorbed photons (N_a). This condition is valid at such short excitation wavelengths in the ultraviolet for the low external electric field levels that we use in our characterization. The inset of Figure 5.3 shows the electric field dependence of PL intensity integrated over 440–470 nm corresponding to 2.73±0.09 eV. This energy range we considered in this partial integration spans the transition energy of ground state electron and hole for all electric field values. This shows the relative QE behavior as a function of applied field.

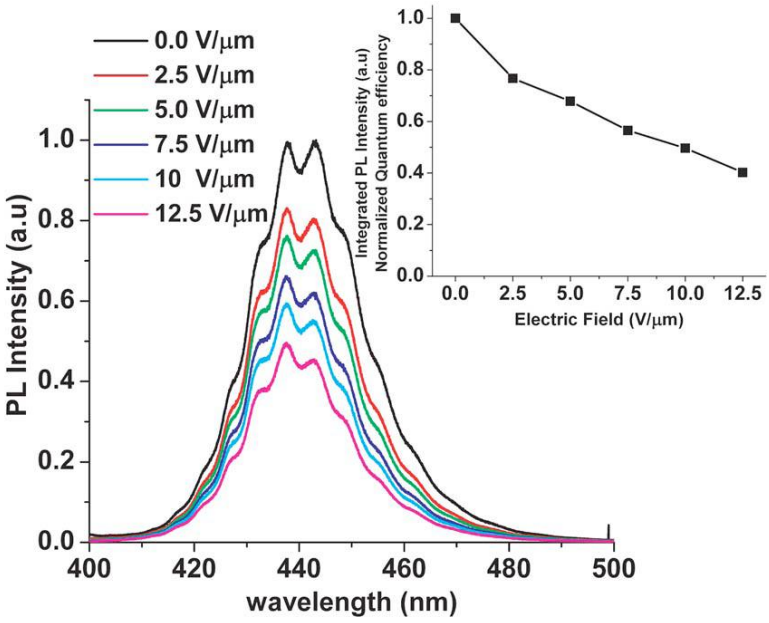

Figure 5. 3 Steady-state PL spectra of our polar InGaN/GaN quantum heterostructure under different electric field levels. The integrated PL intensity for the corresponding electric field level is presented in the inset. After [73].

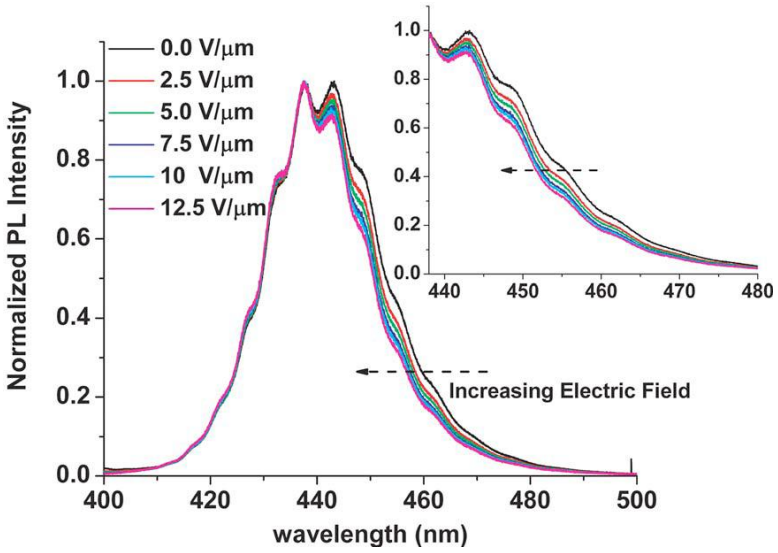

Figure 5. 4 Normalized PL spectra of our polar InGaN/GaN quantum heterostructure under electric field. We observe a narrowing of the spectra along with a blueshift in the longer wavelength region, with a zoom-in presented in the inset for clarity. After [73].

From the relative QE and carrier lifetime measurements, we can deduce relative radiative recombination lifetimes. As shown in Fig. 5.4, τ_r tends to decrease with increasing external electric field. The decrease of radiative recombination lifetime is explained with the overlap integral of electron and hole ground states (calculated using transfer matrix method) that increases with increasing external electric field as given for two of our cases in the inset of Fig. 5.5. This is a result of the reversed quantum-confined Stark effect and Fermi's golden rule **[39]**. Also in Fig. 5.5, we compare the normalized reciprocal of squared overlap integral of calculated electron and hole ground state wavefunctions with our experimental relative τ_r results, both of which show the same trend of change in response to the applied field.

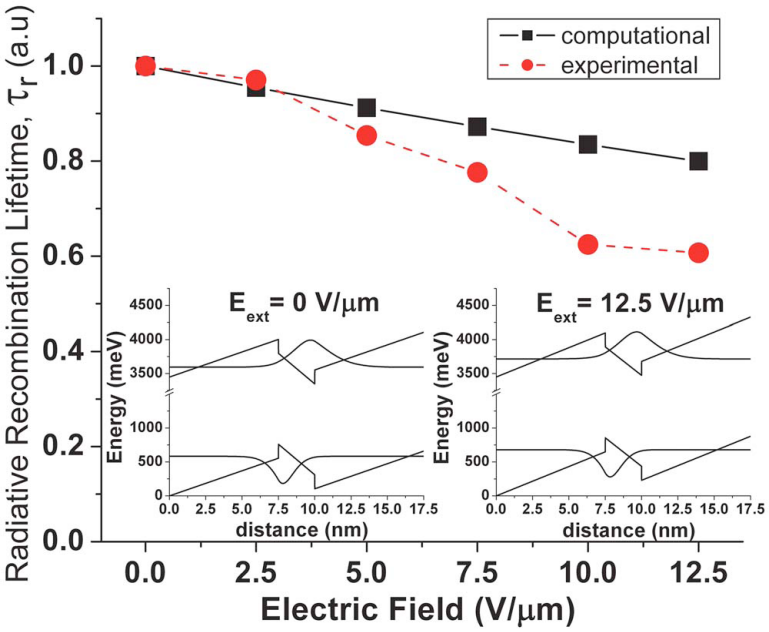

Figure 5. 5 Relative radiative recombination lifetime extracted from TRPL and PL measurements. The inset shows energy band diagrams corresponding electron and hole ground state wavefunctions for the case of 0 V/μm and 12.5 V/μm externally applied electric field. After [73].

In summary, we presented radiative decay kinetics of polar InGaN/GaN quantum heterostructures and its electric field dependence at low applied fields. Our experimental measurements and numerical analyses show that the carrier lifetimes and radiative recombination lifetimes both decrease with increasing external electric field. However, the radiative component demonstrates comparatively a weaker dependence on the electric field, while the overall PL kinetics exhibits stronger electric field dependence. As a result of our study, we qualitatively demonstrate and verify a fundamental physics concept, Fermi's golden rule, to be dependent on external electric field in a polar InGaN/GaN quantum heterostructure.

5.2 Opposite carrier dynamics behavior in polar *vs.* nonpolar InGaN/GaN

This section is based on the publication *"Opposite carrier dynamics and optical absorption characteristics under external electric field in nonpolar vs. polar*

InGaN/GaN based quantum heterostructures," by E. Sari, S. Nizamoğlu, J.-H. Choi, S.-J. Lee, K.-H. Baik, I.-H. Lee, J.-H. Baek, S.-M. Hwang, and H. V. Demir, Optics Express 19, 5442 (2011). Reproduced with permission from Optical Society of America.

In the past, several physically important phenomena were investigated in polar and nonpolar epitaxial materials, e.g., through time-resolved photoluminescence **[81]**, cathodoluminescence **[82]** and differential transmission and reflection measurements **[83]**. Especially related with our current investigation, electric field dependent optical absorption and time- and spectrum-resolved photoluminescence studies were performed in polar structures by our group **[73]** and others **[80]**. However, these analyses, which are fundamentally important for the understanding of operation and performance of various devices, have not been studied in such nonpolar GaN–based quantum heterostructures. Also, a comparative study on their characteristics between nonpolar and polar InGaN/GaN quantum heterostructure epitaxy has not been reported.

In our previous study, we investigated carrier lifetimes in polar InGaN/GaN quantum structures under different levels of external electric field **[73]**. The carrier lifetimes were then shown to decrease strongly with increasing reverse bias in these polar structures **[73]**, also consistent with the previous studies **[80]**. There are at least two reasons behind this observation: One of them is that the reverse bias generates electric field in the opposite direction to polarization-induced field inside the well layer, given that the growth technique is MOCVD and the device architecture is p-i-n, with the p-side on the top. This increasing reverse bias directly shortens radiative component of the carrier lifetime through the increased squared-overlap-integral of electron and hole wavefunctions by Fermi's golden rule. The other reason is the dissociation of excitons through carrier drift, leading to shortened nonradiative component of the carrier lifetime. In an earlier study, we also showed that absorption spectra shift with increasing external electric field in such polar InGaN/GaN quantum heterostructures and demonstrated reversed quantum-confined Stark effect **[57]**. The physical

explanation for this phenomenon is that the energy difference between the electron and hole ground states at which the vertical transition takes place increases with the external electric field that is in the opposite direction to the built-in polarization-induced electrostatic fields inside the well layers. An in-house developed quantum mechanics modeling tool based on transfer matrix method was further used for the physical understanding and simulation of these findings.

In the present work, different than prior works of our group and others, we present a study on the field dependent carrier dynamics of InGaN/GaN quantum heterostructures in nonpolar crystal orientation on a-plane to compare against those in polar orientation on c-plane. In both cases, the quantum structures are housed in the intrinsic region of a *p-i-n* diode, with the p-region on the top. Using these comparative sets of nonpolar *vs.* polar quantum heterostructures, we observe surprisingly a completely opposite behavior in the external electric field dependence of their carrier lifetimes in their respective reverse and forward biases in time-resolved photoluminescence measurements and respective numerical analyses. Our results for the polar, c-plane grown devices are in agreement with the previously reported results, in which decreased carrier lifetime **[80]** was observed with increasing reverse bias voltages.

The quantum heterostructures studied in this part were the same samples as in Section 4.3, where we explained the opposite electroabsorption behavior in polar *vs*. nonpolar InGaN / GaN quantum structures. The carrier lifetimes (τ) of these quantum structures were measured at room temperature using a commercially available time-resolved photoluminescence setup (from PicoQuant GmbH) that contains an InGaN/AlGaN based pump diode laser, emitting at 375 nm and operated in pulsed mode. The experimental conditions were kept the same for both devices. Average and peak intensities of laser excitation were kept at low values, at around 3 and 6 W/cm^2, respectively, to avoid band filling effect and thus evolution of higher energy states. Moreover, at such laser excitation intensity levels, with the given carrier densities in the active region, the effect of Auger

recombination on the carrier lifetimes is insignificant. The measurement setup also consists of a monochromator, a photomultiplier tube and controller electronics. We set the passband center wavelength of the monochromator to 500 nm for both sets of measurements. This wavelength corresponds to a strong emission wavelength for both structures.

In Fig. 5.6, we present the photoluminescence decay time traces of the polar heteroepitaxy on c-plane under different levels of external bias. As a general trend, the photoluminescence first starts to decay faster with stronger electric field as the reverse bias is increased, but then the reverse bias voltages greater than 1.00 V show a diminishing effect. Such a photoluminescence decay behavior modified with the external field application is in conformity with the observations in the previous works of our group **[73]** and Jho *et al*. **[80]** (for the reasons discussed previously). In forward bias, however, the polar epi-structure's decay profile slows down as the voltage is increased to 0.25 V, and then the subsequent decay profiles exhibit an inflection point at a time delay of around 50 ns, seen as an increased time constant of the fast component but as a decrease of the overall transient behavior. The increase of fast (nonradiative) component time constant can be explained by the decreased density of the available trap states near the quantum well region, whereas the decrease of the slow (radiative) component time constant, and thus the overall lifetime, can be attributed to the increased density of electrons and holes in the same region through formation of quasi-Fermi levels. For forward and reverse bias voltages of 1.00-2.00 V, we observe no significant change in their decay profiles.

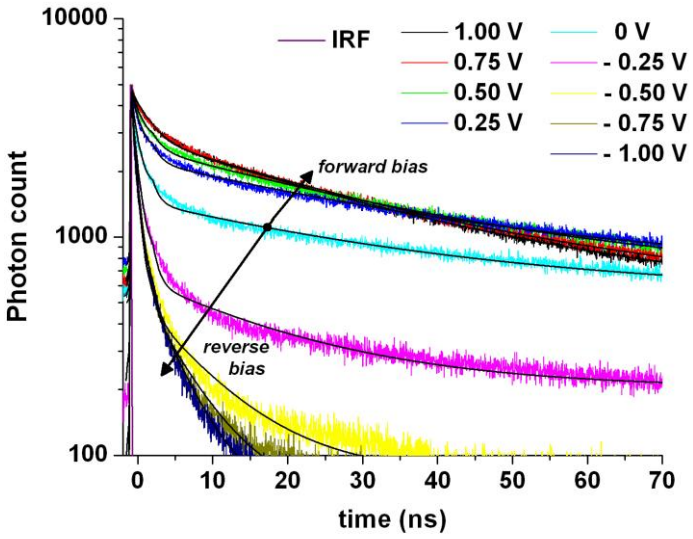

Figure 5. 6 Room temperature time-resolved photoluminescence traces and numerical fits of our device with polar InGaN/GaN quantum heterostructures under different bias levels. After [79].

Similarly, Figure 5.7 shows the photoluminescence decay time traces of nonpolar epitaxy on a-plane with respect to different levels of external electric field. For this set of epi-structure, the electric field dependence is observed to be in the opposite way, where the photoluminescence decays become slower as the external electric field is increased in reverse bias. This results from the reduced overlap integral of electron and hole wavefunctions in the initially nearly square potential well in response to an externally applied electric field. Nevertheless, with increasing reverse bias voltages, the overall time constant of nonradiative component does not decrease as much at low levels of the external electric fields. The nonpolar structure's time-resolved photoluminescence profiles also exhibit faster decays, again opposite to the polar case, as the forward bias voltage is increased (where the lifetimes were measured down to the measurement limit of our optical experimental setup). Again, at such low voltage levels of forward bias, the decreased lifetimes can be explained through compensation of built-in voltage with the external electric field and at some field level, forming an almost perfectly square potential well, which would yield the shortest lifetime.

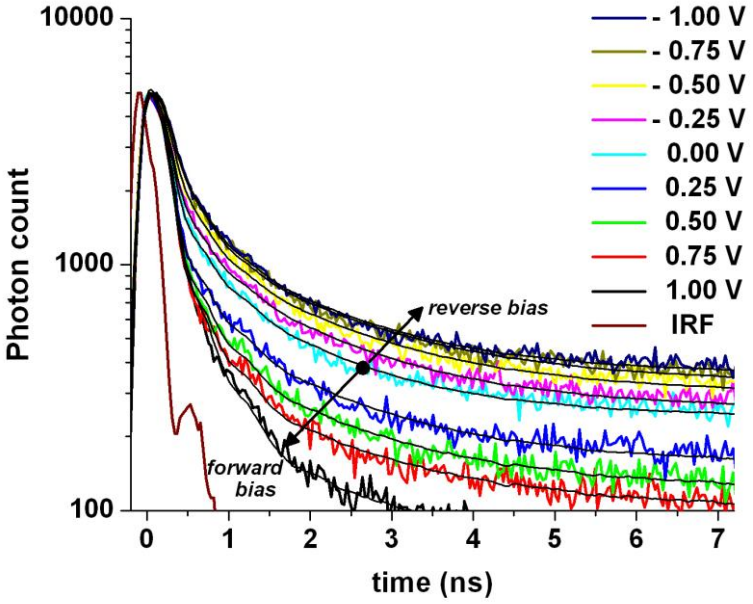

Figure 5. 7 Room temperature time-resolved photoluminescence (RT-TRPL) traces and numerical fits of our device with nonpolar InGaN/GaN quantum heterostructures under different bias levels. After [79].

In our time-resolved analyses, we perform deconvolution of impulse response function (IRF) from the signal and apply a biexponential numerical fitting procedure with low error ($\chi 2$ close to unity) for all decay profiles. We then extract carrier lifetimes (τ) by averaging the time constants, τ_1 and τ_2, with their respective total intensities, i.e., their weights. Thus, the time constants we obtain in this procedure contain information on both slow and fast components of the overall decay profile. The corresponding numerical fits were provided in the decays. From these numerical analyses, we extract the carrier lifetimes as a function of external electric field for both structures as depicted in Fig. 5.8. These analysis results also reveal the opposite behavior in nonpolar vs. polar quantum heterostructures in terms of carrier lifetimes under electric field. Here, we present the lifetimes as a function of externally applied electric fields, rather than voltages, in order to make a meaningful comparison between the two sets of data. Hence, for both structures, we assume that the total voltage drop across the devices is in the depletion regions. We further assume that the depletion widths

are 50 nm, and that they do not change by such low voltage application. With these approximations, we do not lose any generality for our points discussed in here. This opposite behavior could be qualitatively explained by quantum-confined Stark effect and Fermi's golden rule considering the increased vs. decreased squared-overlap integrals of electron and hole wavefunctions (under the assumption that the nonradiative components of the decays would not change with the external electric field within the range of interest) **[42], [57], [73]**.

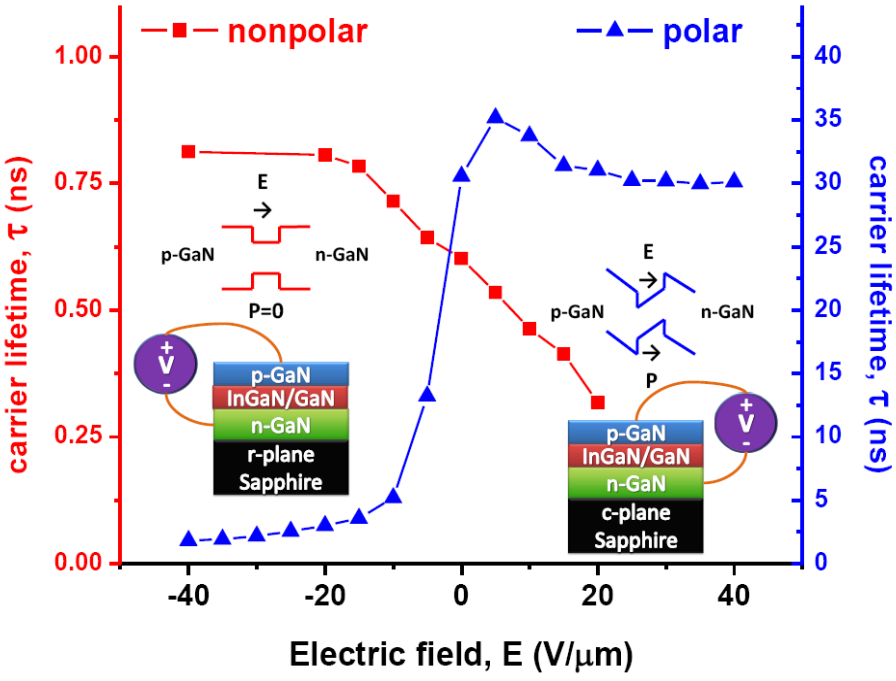

Figure 5. 8 Carrier lifetime (τ) *vs.* external electric field (E) for the polar and nonpolar devices. Note that here E is taken to be positive for the forward bias and negative for the reverse bias. After [79].

In summary, we presented the opposite external electric field dependence of carrier lifetimes in c-plane grown polar *vs.* a-plane grown nonpolar InGaN/GaN quantum heterostructures. We showed using time-resolved photoluminescence measurements that carrier lifetimes decrease with increasing external electric fields in polar quantum epi-structures, whereas the opposite occurs in nonpolar quantum epi-structures. We explained these opposite behaviors in the context of Fermi's golden rule.

5.3 Summary

In this chapter, we presented radiative decay kinetics of InGaN/GaN quantum structures grown on their polar c-planes. Through steady state and time-resolved PL measurements, we identified the external electric field dependence of radiative recombination lifetime, τ_r. We found out that, in our polar structure, radiative recombination lifetime, as well as carrier lifetime and quantum efficiency decrease with increasing electric field.

We further investigated the external electric field dependence of carrier lifetimes in polar *vs.* nonpolar quantum structures with a similar InGaN/GaN quantum structure profile. Through time-resolved PL measurements and subsequent analyses, we showed that carrier lifetimes, τ, decrease in the polar structure and increase in the nonpolar structure.

Our results in this chapter were explained in the context of a fundamental physics phenomenon, Fermi's golden rule.

Chapter 6

Electron Blocking Layers for InGaN / GaN based LEDs with Low Droop

In this chapter, we present our electron blocking layer designs for low efficiency droop. First, we present our superlattice EBL design with a superlinear increase of AlN molar ratio. We further reduce the droop level by optimizing the MQW to EBL distance.

6.1 Introduction

As mentioned earlier, efficiency droop (a.k.a. non-thermal rollover) can be defined as the decrease of LED efficiency with increasing current. For the application areas that require high driving currents (> 350 mA for typical sized LEDs), such as general lighting, this effect is especially critical and need to be reduced through bandgap engineering in order to be applied at current LED fabs in the shortest term.

Several proposals have been made in the last few years towards the reduction of droop effect. Some of these proposals include: using polarization-matched MQW structures **[52]**, p-doped barriers **[54]**, and different well thicknesses **[84]**. However, most of the efforts towards reducing the droop have concentrated on redesigning the electron blocking layer (EBL), since electron overflow from the active regions and hole concentration in quantum well regions are controlled

mostly by the EBL and conventional EBLs (with a constant AlN mole ratio) fail to achieve both at the same time. Until now, some of the proposed EBLs are: ternary InAlN **[85]**, linear graded structure with increasing AlN mole ratio **[86]**, linear graded structure with decreasing AlN mole ratio **[87]**, and superlattice and graded superlattice structures **[56]**. Even not using an EBL at all, was proposed for droop reduction **[88]**. In all of these works, the EBL was placed right above the MQW structure. Here in this thesis work, we propose distance optimized EBLs for the reduction of efficiency droop. Our APSYS simulation results show that LEDs perform better when the EBL's distance from the MQW is optimized compared to the case of directly placing it on top of MQW.

6.2 Designs, Simulations, Results and Discussions

To illustrate our distance optimization idea, we simulated a standard LED comprising an EBL with a different design that was not proposed before. In our design, the EBL is in a superlattice form with a superlinear profile, increasing AlN molar ratio more than a linearly increasing AlN molar ratio, as in Figure 6.1 below. The total thickness of the EBL is 18 nm, and GaN and AlGaN layer thicknesses are 1 nm.

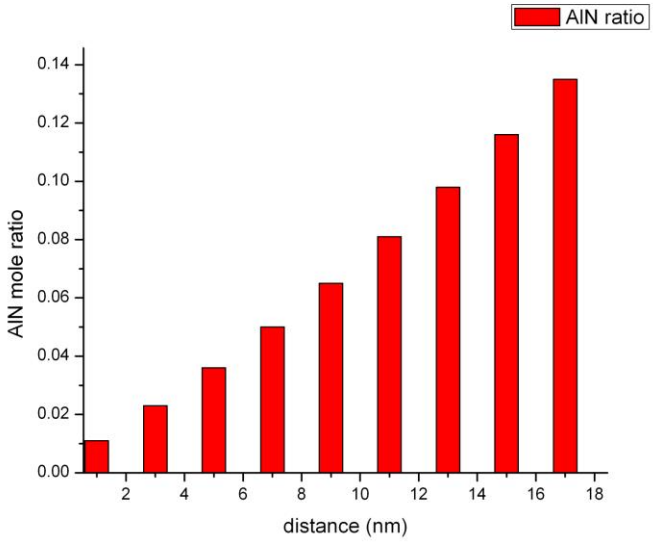

Figure 6. 1 Schematics showing the AlN molar ratio profile of our superlinear superlattice EBL design.

We also performed simulations of the LED structure by changing the distance between MQW and EBL layers with a GaN spacer layer with a thickness of d_1 (nm) placed in between. Moreover, we placed another GaN spacer layer with a thickness of d_2 (nm) between EBL and p-GaN layers in order to keep the total thickness constant. We also performed the simulation of the structures without second spacer layer. For comparison, we simulated the case of no EBL as well. Our resulting LED efficiency vs. current curves are given in Figure 6.2 where the legends show the simulated combinations of d_1 and d_2.

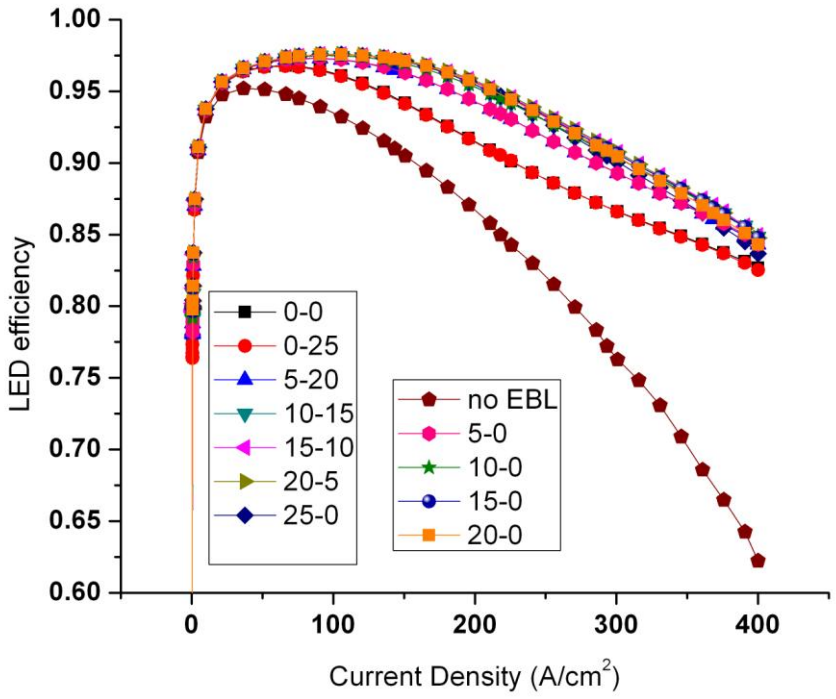

Figure 6. 2 LED efficiency *vs.* current curves of the simulated structures. Our superlinear superlattice EBL design outperforms the structures with no EBL.

As seen in Figure 6.2, all of the simulated LED structures outperform the structure with no EBL in terms of the droop. Their performances are also very close to each other. In order to determine the best performing structure quantitatively we calculated droop levels by subtracting the maximum LED efficiency from the same at 400 A/cm^2. The droop levels of our LED structures are given in Figure 6.3 below.

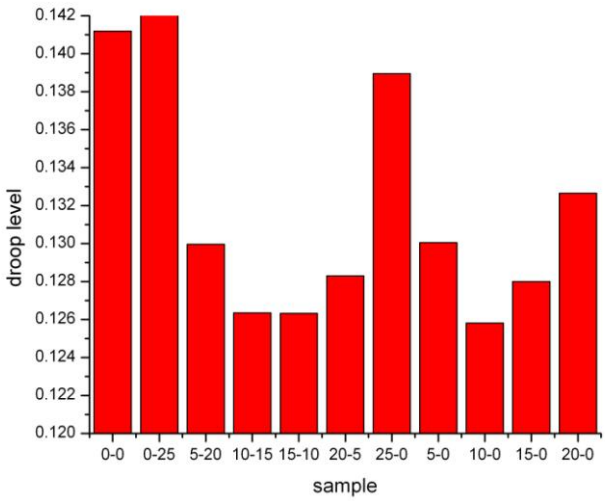

Figure 6. 3 Droop levels of the structures simulated. 10-0 is the best performing structure.

As seen in Figure 6.3, there is an optimal MQW to EBL thickness of about 10 nm. For the 0-0 case, which is conventionally applied in novel EBL studies, the droop level is about 2% indicating that distance optimization helps further reduce droop level. To understand the physics of these samples' performance, we examined electron and hole concentrations at 400 A/cm^2 throughout some of the structures: 25-0, 10-0 (best performing) and 0-0 (conventional), which are given in Figure 6.4 and 6.5, respectively.

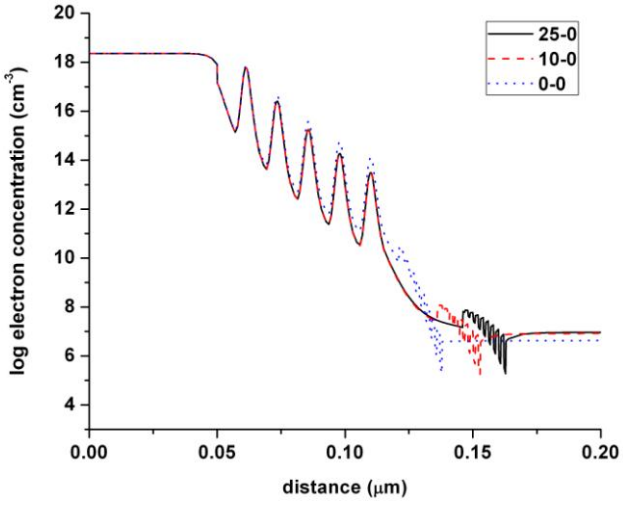

Figure 6. 4 Electron concentrations throughout the active regions for a selected combination of d_1-d_2.

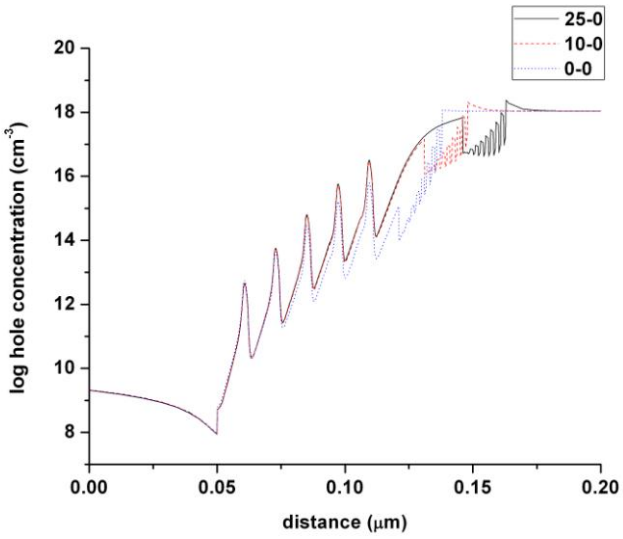

Figure 6. 5 Hole concentrations throughout the active regions for a selected combination of d_1-d_2.

To explain the outperformance of the optimal structure, we looked at the electron leakage, hole incorporation and electron incorporation levels for these structures given in Figures 6.6, 6.7 and 6.8, respectively.

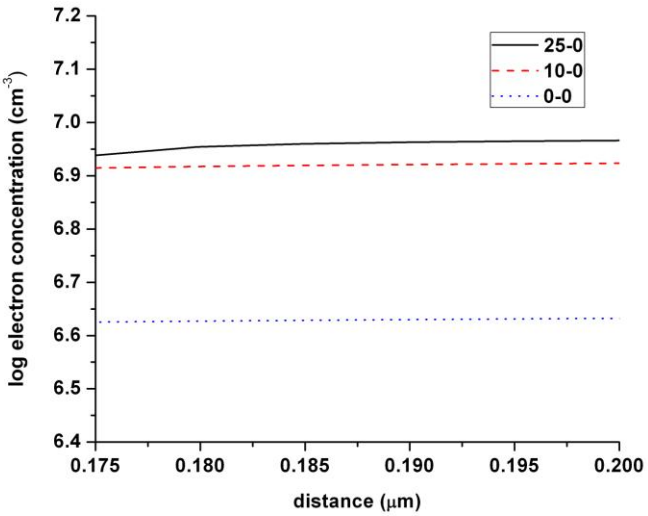

Figure 6. 6 Electron leakage levels of the samples for the indicated of d_1-d_2 combinations.

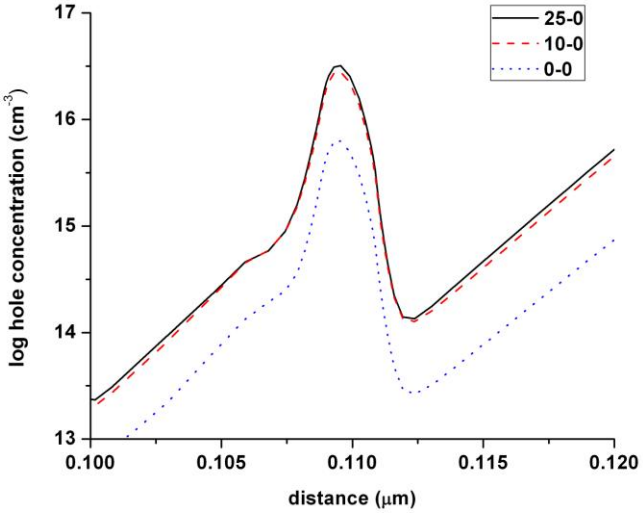

Figure 6. 7 Hole concentration in the last quantum well layer for the given of d_1-d_2 combinations.

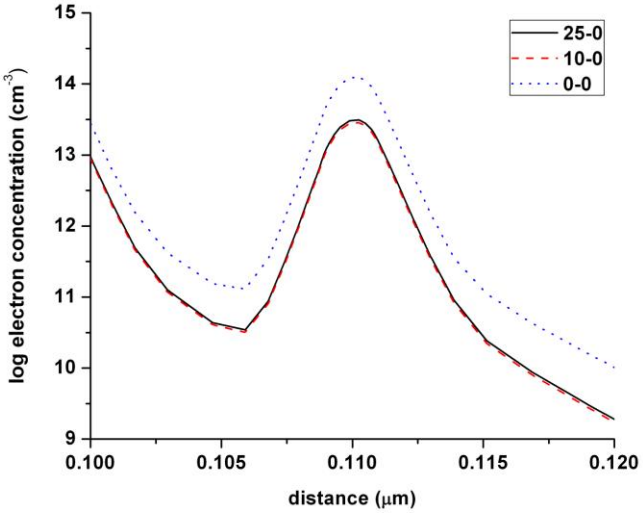

Figure 6. 8 Electron concentration in the last quantum well layer for the given of d_1-d_2 combinations.

Our results indicate that the sample with no spacer has the lowest level of hole incorporation in the last quantum well layer and the samples with 10 and 25 nm spacers have a very close amount of hole incorporation. On the other hand, the situation is the opposite for electron incorporation. Moreover, in terms of electron

leakage, the sample with 10 nm spacer has the lowest level of electron leakage compared to the sample with 25 nm spacer, explaining its superior performance.

6.3 Summary

In this work, we showed that droop reduction is possible by the distance optimization of EBL to MQW. By designing a special electron blocking layer, we demonstrated that there exists an optimal MQW-to-EBL distance. By comparing the optimal structure's performance and physical properties (electron leakage and hole incorporation) with a conventional structure (0 nm distance) and a test structure (25 nm distance), we explained superior performance of the optimal distance structure.

Chapter 7

Conclusions

In this thesis work, we presented our research work on the optoelectronics of InGaN/GaN quantum structures. We started with background information on the properties of III-Nitrides, optoelectronic device physics, and InGaN/GaN based optoelectronic device demonstrations from the literature, including our previous work on the electroabsorption modulators.

We continued with dislocation density dependent electroabsorption in the epitaxial lateral overgrown (ELOG) InGaN/GaN quantum structures. Our experimental results deduced from PL, time-resolved PL, and electroabsorption characterization follow a similar trend with the dislocation density (by etch pit formation). More interestingly, we found out that electroabsorption performance is much more sensitive to the dislocation densities and the amount of residual strain released in ELOG coalescence walls, compared to the PL performance.

We then moved on to our studies on comparative study of three electroabsorption modulators based on c-plane grown polar structures, tuned by MQW structural parameters. The EA performance of our modulator with the lowest built-in electrostatic field inside the well layers was superior compared to the other two.

We presented our results on the electroabsorption of polar vs. nonpolar InGaN/GaN quantum structures through electroabsorption measurements. With the blue- and red-shifting absorption profiles of polar and nonpolar structures, respectively, in response to increasing electric field, the two structures showed an opposite behavior.

We studied external electric field dependent radiative lifetimes in polar InGaN/GaN quantum structures. Our results and analyses showed that carrier lifetimes and quantum efficiencies decrease with increasing electric field. Through the definition of quantum efficiency, we obtained the electric field dependence of radiative recombination lifetimes, which also decrease with increasing electric field. This is in consistency with Fermi's golden rule, which relates radiative recombination lifetimes to electron and hole wavefunction overlaps (oscillator strength).

In the next part, we presented our work on the external electric field dependent carrier dynamics of polar and nonpolar InGaN/GaN quantum structures. Through time-resolved photoluminescence measurements and subsequent analyses, we observed that carrier lifetimes decrease with increasing electric field in polar structures and they increase with increasing electric field in nonpolar structures. This opposite behavior stems from the polarization-induced electrostatic fields and related physical phenomenon, including Fermi's golden rule.

In the last part, we presented our design work on the electron blocking layers of blue LEDs where we showed that MQW-to-EBL distance can be optimized to reduce droop effect. We examined the electron and hole concentrations throughout our structures to improve electron and hole incorporation in the active layers, and decrease electron leakage out of the active layer for the improved device performance and reduced droop.

We believe that the scientific contributions of this thesis to III-Nitride device platform will help improve the optoelectronic device performance and open up possibilities to be utilized in new and unprecedented applications.

Scientific Contributions

Journal Papers

1. E. Sari, L. W. Jang, J. H. Baek, I.-H. Lee, X. W. Sun, and H. V. Demir, 'Dislocation density dependent electroabsorption in epitaxial lateral overgrown InGaN/GaN quantum structures', *Opt. Express, in press*, 2012.
2. E. Sari, S. Nizamoglu, J.-H. Choi, S.-J. Lee, K.-H. Baik, I.-H. Lee, J.-H. Baek, S.-M. Hwang, and H. V. Demir, 'Opposite carrier dynamics and optical absorption characteristics under external electric field in nonpolar vs. polar InGaN/GaN based quantum heterostructures', *Opt. Express*, vol. 19, no. 6, pp. 5442–5450, Mar. 2011.
3. H. V. Demir, U. O. S. Seker, G. Zengin, E. Mutlugun, E. Sari, C. Tamerler, and M. Sarikaya, 'Spatially Selective Assembly of Quantum Dot Light Emitters in an LED Using Engineered Peptides', ACS Nano, vol. 5, no. 4, pp. 2735–2741, Apr. 2011.
4. S. Nizamoglu, E. Sari, J.-H. Baek, I.-H. Lee, and H. V. Demir, 'Nonradiative resonance energy transfer directed from colloidal CdSe/ZnS quantum dots to epitaxial InGaN/GaN quantum wells for solar cells', *physica status solidi (RRL) – Rapid Research Letters*, vol. 4, no. 7, pp. 178–180, 2010.
5. E. Sari, S. Nizamoglu, I.-H. Lee, J.-H. Baek, and H. V. Demir, 'Electric field dependent radiative decay kinetics of polar InGaN/GaN quantum heterostructures at low fields', *Applied Physics Letters*, vol. 94, no. 21, pp. 211107–211107–3, May 2009.
6. E. Sari, T. Ozel, A. Koc, J.-W. Ju, H.-K. Ahn, I.-H. Lee, J.-H. Baek, and H. V. Demir, 'Comparative study of electroabsorption in InGaN/GaN quantum zigzag heterostructures with polarization-induced electric fields', *Applied Physics Letters*, vol. 92, no. 20, pp. 201105–201105–3, May 2008.

7. E. Sari, S. Nizamoglu, T. Ozel, and H. V. Demir, ‘Blue quantum electroabsorption modulators based on reversed quantum confined Stark effect with blueshift’, *Applied Physics Letters*, vol. 90, no. 1, pp. 011101–011101–3, Jan. 2007.
8. S. Nizamoglu, T. Ozel, E. Sari, and H. V. Demir, ‘White light generation using CdSe/ZnS core–shell nanocrystals hybridized with InGaN/GaN light emitting diodes’, *Nanotechnology*, vol. 18, no. 6, p. 065709, Feb. 2007.
9. T. Ozel, E. Sari, S. Nizamoglu, and H. V. Demir, ‘Violet to deep-ultraviolet InGaN/GaN and GaN/AlGaN quantum structures for UV electroabsorption modulators’, Journal of Applied Physics, vol. 102, no. 11, pp. 113101–113101–5, Dec. 2007.
10. H. V. Demir, S. Nizamoglu, T. Ozel, E. Mutlugun, I. Ozge Huyal, E. Sari, E. Holder, and N. Tian, ‘White light generation tuned by dual hybridization of nanocrystals and conjugated polymers’, New Journal of Physics, vol. 9, no. 10, pp. 362–362, Oct. 2007.

Refereed International Conference papers

11. E. Sari, S. Nizamoğlu, S.J. Lee, K.H. Baik, J.H. Baek and H. V. Demir, "Polar vs. nonpolar InGaN/GaN quantum heterostructures: opposite quantum confined electroabsorption and carrier dynamics behavior," IEEE Photonics Global Conference, Singapore, December 14-16, 2010.
12. E. Sari, O.Akyuz, E.G. Choi, I.H. Lee, J. H. Baek and H. V. Demir, "Controlled growth and characterization of epitaxially-laterally-overgrown InGaN/GaN quantum heterostructures," Proceedings of 23rd IEEE Annual Photonics Society Meeting, Denver, CO, USA (7-11 November 2010). Session: TuX: Novel Integrated Devices. Paper: TuX 4.
13. E. Sari,S. Nizamoğlu, I.-H. Lee, J.-H. Baek and H. V. Demir, "Electric field dependence of radiative recombination lifetimes in polar InGaN/GaN quantum heterostructures" Proceedings of IEEE Photonics

Society 2009 Annual Meeting (LEOS 2009), Belek, Antalya, Turkey (4-8 October 2009). Session: WX: High Power Lasers. Paper WX5.

14. S. Nizamoğlu, E. Sari, J. H. Baek, I. H. Lee and H. V. Demir, "Nanocrystal integrated light emitting diodes based on radiative and nonradiative energy transfer for the green gap" Proceedings of IEEE Photonics Society 2009 Annual Meeting (LEOS 2009), Antalya, Turkey (4 - 8 October 2009). Session: MI: Advanced Display Technologies. Paper MI 4.
15. E. Sari, T. Ozel, A. Koc, J.-W. Ju, H.-K. Ahn, I.-H. Lee, J. H. Baek, and H. V. Demir, "Experimental and computational analyses of electroabsorption in polar InGaN/GaN quantum zigzag heterostructures," Proceedings of IEEE Lasers and Electro-Optics Society 2008 Annual Meeting (LEOS 2008), Newport Beach, CA (9-13 November 2008). Session: WC: Optical Properties of Nanostructures. Paper WC5.
16. G. Zengin, U. O. S. Seker, A. Koc, E. Mutlugün, O. Akyuz, E. Sari, M. Sarikaya, C. Tamerler, and H. V. Demir, "Multi-material specific, targeted self-assembly of nanocrystal emitters using genetically engineered peptides on optoelectronic microchips," Proceedings of IEEE Lasers and Electro-Optics Society 2008 Annual Meeting (LEOS 2008), Newport Beach, CA (9 - 13 November 2008). Session: TuL: Biophotonics IV: Novel Approaches in Nano-Biophotonics. Paper TuL4.
17. E. Sari, S. Nizamoğlu, T. Ozel, and H. V. Demir, "Blue InGaN/GaN-based quantum electroabsorption modulators," Proceedings of IEEE Conference on Optoelectronic and Microelectronic Materials and Devices (COMMAD 2006), Perth, Australia (6-7 December 2006). Paper WO-A4.
18. E. Sari, S. Nizamoğlu, T. Ozel, H. V. Demir, A. Inal, E. Ulker, E. Ozbay, Y. Dikme and M. Heuken, "InGaN/GaN based LEDs with electroluminescence in violet, blue, and green tuned by epitaxial growth temperature," Proceedings of IEEE Lasers and Electro-Optics Society

2006 Annual Meeting (LEOS 2006), Montreal, QC, Canada (29 October-2 November 2006). Paper MC3.

19. S. Nizamoğlu, T. Ozel, E. Sari, and H. V. Demir, "White lght generation with CdSe/ZnS core-shell nanocrystals and InGaN/GaN light emitting diodes," Proceedings of IEEE Conference on Optoelectronic and Microelectronic Materials and Devices (COMMAD 2006), Perth, Australia (6-7 December 2006). Paper WO-A5.

BIBLIOGRAPHY

[1] S. Nakamura, G. Fasol, and S. J. Pearton, *The Blue Laser Diode: The Complete Story*, 2nd updated and extended ed. Springer, 2000.

[2] S. T. Tan, X. W. Sun, H. V. Demir, and S. P. DenBaars, 'Advances in the LED Materials and Architectures for Energy-Saving Solid-State Lighting Toward "Lighting Revolution", *IEEE Photonics Journal*, vol. 4, no. 2, pp. 613 –619, Apr. 2012.

[3] Cree sets new R&D white-light LED luminous-efficacy record of 254 lumens per watt, Laser Focus World, [online], 2012, www.laserfocusworld.com/articles/2012/04/cree-sets-new-white-light-led-luminous-efficacy-record-of-254-lumens-per-watt.html, (Accessed 10 November 2012).

[4] Packaged LED Market, Yole Developpement, [online] 2012, http://www.yole.fr/2012_press_releases.aspx (Accessed: 11 November 2012).

[5] S. Nizamoglu, T. Ozel, E. Sari, and H. V. Demir, 'White light generation using CdSe/ZnS core–shell nanocrystals hybridized with InGaN/GaN light emitting diodes', *Nanotechnology*, vol. 18, no. 6, p. 065709, Feb. 2007.

[6] H. V. Demir, S. Nizamoglu, T. Ozel, E. Mutlugun, I. Ozge Huyal, E. Sari, E. Holder, and N. Tian, 'White light generation tuned by dual hybridization of nanocrystals and conjugated polymers', *New Journal of Physics*, vol. 9, no. 10, pp. 362–362, Oct. 2007.

[7] S. Nizamoglu, E. Sari, J.-H. Baek, I.-H. Lee, and H. V. Demir, 'Nonradiative resonance energy transfer directed from colloidal CdSe/ZnS quantum dots to epitaxial InGaN/GaN quantum wells for solar cells',

physica status solidi (RRL) – Rapid Research Letters, vol. 4, no. 7, pp. 178–180, 2010.

[8] H. V. Demir, U. O. S. Seker, G. Zengin, E. Mutlugun, E. Sari, C. Tamerler, and M. Sarikaya, 'Spatially Selective Assembly of Quantum Dot Light Emitters in an LED Using Engineered Peptides', *ACS Nano*, vol. 5, no. 4, pp. 2735–2741, Apr. 2011.

[9] S. Nizamoglu, E. Sari, J.-H. Baek, I.-H. Lee, and H. Volkan Demir, 'Green/Yellow Solid-State Lighting via Radiative and Nonradiative Energy Transfer Involving Colloidal Semiconductor Nanocrystals', *IEEE Journal of Selected Topics in Quantum Electronics*, vol. 15, no. 4, pp. 1163 –1170, Aug. 2009.

[10] S. Nakamura, T. Mukai, and M. Senoh, 'Candela-class high-brightness InGaN/AlGaN double-heterostructure blue-light-emitting diodes', *Applied Physics Letters*, vol. 64, no. 13, pp. 1687–1689, Mar. 1994.

[11] H. Amano, N. Sawaki, I. Akasaki, and Y. Toyoda, 'Metalorganic vapor phase epitaxial growth of a high quality GaN film using an AlN buffer layer', *Applied Physics Letters*, vol. 48, no. 5, pp. 353–355, Feb. 1986.

[12] S. Nakamura, Y. Harada, and M. Seno, 'Novel metalorganic chemical vapor deposition system for GaN growth', *Applied Physics Letters*, vol. 58, no. 18, pp. 2021–2023, May 1991.

[13] J. Neugebauer and C. G. Van de Walle, 'Atomic geometry and electronic structure of native defects in GaN', *Phys. Rev. B*, vol. 50, no. 11, pp. 8067–8070, Eylül 1994.

[14] M. Heuken, 'Mass production of optoelectronic devices for Solid State Lighting (SSL) by MOCVD', in *Optical Fiber Communication Optoelectronic Exposition Conference, 2008. AOE 2008. Asia*, 2008, pp. 1 – 3.

[15] S. Strite and H. Morkoc, 'GaN, AlN, and InN: A review', *Journal of Vacuum Science & Technology B: Microelectronics and Nanometer Structures*, vol. 10, no. 4, pp. 1237–1266, 1992.

[16] T. Hanada, ‘Basic Properties of ZnO, GaN, and Related Materials’, in *Oxide and Nitride Semiconductors*, vol. 12, T. Yao and S.-K. Hong, Eds. Berlin, Heidelberg: Springer Berlin Heidelberg, 2009, pp. 1–19.

[17] D. A. B. Miller, *Quantum Mechanics for Scientists and Engineers*. Cambridge University Press, 2008.

[18] V. Fiorentini, F. Bernardini, F. Della Sala, A. Di Carlo, and P. Lugli, ‘Effects of macroscopic polarization in III-V nitride multiple quantum wells’, *Phys. Rev. B*, vol. 60, no. 12, pp. 8849–8858, Sep. 1999.

[19] E. Sari, T. Ozel, A. Koc, J.-W. Ju, H.-K. Ahn, I.-H. Lee, J.-H. Baek, and H. V. Demir, ‘Comparative study of electroabsorption in InGaN/GaN quantum zigzag heterostructures with polarization-induced electric fields’, *Applied Physics Letters*, vol. 92, no. 20, pp. 201105–201105–3, May 2008.

[20] F. Scholz, ‘Semipolar GaN grown on foreign substrates: a review’, *Semiconductor Science and Technology*, vol. 27, no. 2, p. 024002, Feb. 2012.

[21] P. Waltereit, O. Brandt, M. Ramsteiner, R. Uecker, P. Reiche, and K. . Ploog, ‘Growth of M-plane GaN(1 1̄ 0 0) on γ-LiAlO2(1 0 0)’, *Journal of Crystal Growth*, vol. 218, no. 2–4, pp. 143–147, Sep. 2000.

[22] M. D. Craven, S. H. Lim, F. Wu, J. S. Speck, and S. P. DenBaars, ‘Threading dislocation reduction via laterally overgrown nonpolar (110) a-plane GaN’, *Applied Physics Letters*, vol. 81, no. 7, pp. 1201–1203, Aug. 2002.

[23] M. D. Craven, A. Chakraborty, B. Imer, F. Wu, S. Keller, U. K. Mishra, J. S. Speck, and S. P. DenBaars, ‘Structural and electrical characterization of a-plane GaN grown on a-plane SiC’, *physica status solidi (c)*, vol. 0, no. 7, pp. 2132–2135, 2003.

[24] A. Chitnis, C. Chen, V. Adivarahan, M. Shatalov, E. Kuokstis, V. Mandavilli, J. Yang, and M. A. Khan, ‘Visible light-emitting diodes using a-plane GaN–InGaN multiple quantum wells over r-plane sapphire’, *Applied Physics Letters*, vol. 84, no. 18, pp. 3663–3665, Apr. 2004.

[25] B. A. Haskell, F. Wu, M. D. Craven, S. Matsuda, P. T. Fini, T. Fujii, K. Fujito, S. P. DenBaars, J. S. Speck, and S. Nakamura, ‘Defect reduction in (110) a-plane gallium nitride via lateral epitaxial overgrowth by hydride vapor-phase epitaxy’, *Applied Physics Letters*, vol. 83, no. 4, pp. 644–646, Jul. 2003.

[26] S.-M. Hwang, Y. G. Seo, K. H. Baik, I.-S. Cho, J. H. Baek, S. Jung, T. G. Kim, and M. Cho, ‘Demonstration of nonpolar a-plane InGaN/GaN light emitting diode on r-plane sapphire substrate’, *Applied Physics Letters*, vol. 95, no. 7, pp. 071101–071101–3, Aug. 2009.

[27] H. Masui, S. Nakamura, S. P. DenBaars, and U. K. Mishra, ‘Nonpolar and Semipolar III-Nitride Light-Emitting Diodes: Achievements and Challenges’, *IEEE Transactions on Electron Devices*, vol. 57, no. 1, pp. 88 –100, Jan. 2010.

[28] R. Sharma, P. M. Pattison, H. Masui, R. M. Farrell, T. J. Baker, B. A. Haskell, F. Wu, S. P. DenBaars, J. S. Speck, and S. Nakamura, ‘Demonstration of a semipolar (10) InGaN/GaN green light emitting diode’, *Applied Physics Letters*, vol. 87, no. 23, pp. 231110–231110–3, Nov. 2005.

[29] H. Zhong, A. Tyagi, N. N. Fellows, F. Wu, R. B. Chung, M. Saito, K. Fujito, J. S. Speck, S. P. DenBaars, and S. Nakamura, ‘High power and high efficiency blue light emitting diode on freestanding semipolar (10) bulk GaN substrate’, *Applied Physics Letters*, vol. 90, no. 23, pp. 233504–233504–3, Jun. 2007.

[30] A. Tyagi, H. Zhong, R. B. Chung, D. F. Feezell, M. Saito, K. Fujito, J. S. Speck, S. P. DenBaars, and S. Nakamura, ‘Semipolar $(10\bar{1}\bar{1})$ InGaN/GaN Laser Diodes on Bulk GaN Substrates’, *Japanese Journal of Applied Physics*, vol. 46, no. No. 19, pp. L444–L445, May 2007.

[31] R. Dwiliński, R. Doradziński, J. Garczyński, L. P. Sierzputowski, A. Puchalski, Y. Kanbara, K. Yagi, H. Minakuchi, and H. Hayashi, ‘Excellent crystallinity of truly bulk ammonothermal GaN’, *Journal of Crystal Growth*, vol. 310, no. 17, pp. 3911–3916, Ağustos 2008.

[32] G. B. Stringfellow, *Organometallic Vapor-Phase Epitaxy, Second Edition: Theory and Practice*, 2nd ed. Academic Press, 1998.

[33] B. M. Imer, 'Improved Quality III-Nitride Heteroepitaxial Films and Devices', University of California, Santa Barbara, 2006.

[34] S. P. DenBaars, 'Gallium Nitride Materials Technology', 1998.

[35] H. Heinke, V. Kirchner, S. Einfeldt, and D. Hommel, 'X-ray diffraction analysis of the defect structure in epitaxial GaN', *Applied Physics Letters*, vol. 77, no. 14, pp. 2145–2147, Oct. 2000.

[36] S. R. Lee, A. M. West, A. A. Allerman, K. E. Waldrip, D. M. Follstaedt, P. P. Provencio, D. D. Koleske, and C. R. Abernathy, 'Effect of threading dislocations on the Bragg peakwidths of GaN, AlGaN, and AlN heterolayers', *Applied Physics Letters*, vol. 86, no. 24, pp. 241904–241904–3, Jun. 2005.

[37] B. E. A. Saleh and M. C. Teich, *Fundamentals of Photonics*, 2nd ed. Wiley-Interscience, 2007.

[38] E. F. Schubert, *Light-Emitting Diodes*. Cambridge University Press, 2003.

[39] S. L. Chuang, *Physics of Photonic Devices*. John Wiley & Sons, 2009.

[40] W. Franz, 'Einfluß eines elektrischen Feldes auf eine optische Absorptionskante', *Zeitschrift Naturforschung Teil A*, vol. 13, p. 484, Haziran 1958.

[41] L. V. Keldysh, 'Behavior of Non-metallic Crystals in Strong Electric Fields', *Soviet Journal of Experimental and Theoretical Physics*, vol. 6, p. 763, 1958.

[42] D. A. B. Miller, D. S. Chemla, T. C. Damen, A. C. Gossard, W. Wiegmann, T. H. Wood, and C. A. Burrus, 'Electric field dependence of optical absorption near the band gap of quantum-well structures', *Phys. Rev. B*, vol. 32, no. 2, pp. 1043–1060, Jul. 1985.

[43] K. W. Goossen, J. A. Walker, L. A. D'Asaro, S. P. Hui, B. Tseng, R. Leibenguth, D. Kossives, D. D. Bacon, D. Dahringer, L. M. F. Chirovsky, A. L. Lentine, and D. A. B. Miller, 'GaAs MQW modulators integrated with

silicon CMOS', *IEEE Photonics Technology Letters*, vol. 7, no. 4, pp. 360 – 362, Apr. 1995.

[44] D. A. B. Miller, 'Optics for low-energy communication inside digital processors: quantum detectors, sources, and modulators as efficient impedance converters', *Opt. Lett.*, vol. 14, no. 2, pp. 146–148, Jan. 1989.

[45] H. Demir, V. Sabnis, O. Fidaner, J. Harris Jr, D. Miller, and J.-F. Zheng, 'Dual-diode quantum-well modulator for C-band wavelength conversion and broadcasting', *Opt Express*, vol. 12, no. 2, pp. 310–316, Jan. 2004.

[46] Y.-H. Kuo, Y. K. Lee, Y. Ge, S. Ren, J. E. Roth, T. I. Kamins, D. A. B. Miller, and J. S. Harris, 'Strong quantum-confined Stark effect in germanium quantum-well structures on silicon', *Nature*, vol. 437, no. 7063, pp. 1334–1336, Oct. 2005.

[47] S. Nakamura, M. Senoh, N. Iwasa, and S. Nagahama, 'High-power InGaN single-quantum-well-structure blue and violet light-emitting diodes', *Applied Physics Letters*, vol. 67, no. 13, pp. 1868–1870, Sep. 1995.

[48] S. Nakamura, M. Senoh, N. Iwasa, and S. Nagahama, 'High-Brightness InGaN Blue, Green and Yellow Light-Emitting Diodes with Quantum Well Structures', *Japanese Journal of Applied Physics*, vol. 34, no. Part 2, No. 7A, pp. L797–L799, 1995.

[49] J. Piprek, 'Efficiency droop in nitride-based light-emitting diodes', *physica status solidi (a)*, vol. 207, no. 10, pp. 2217–2225, 2010.

[50] E. Kioupakis, P. Rinke, K. T. Delaney, and C. G. Van de Walle, 'Indirect Auger recombination as a cause of efficiency droop in nitride light-emitting diodes', *Applied Physics Letters*, vol. 98, no. 16, pp. 161107–161107–3, Apr. 2011.

[51] M.-H. Kim, M. F. Schubert, Q. Dai, J. K. Kim, E. F. Schubert, J. Piprek, and Y. Park, 'Origin of efficiency droop in GaN-based light-emitting diodes', *Applied Physics Letters*, vol. 91, no. 18, pp. 183507–183507–3, Oct. 2007.

[52] M. F. Schubert, J. Xu, J. K. Kim, E. F. Schubert, M. H. Kim, S. Yoon, S. M. Lee, C. Sone, T. Sakong, and Y. Park, 'Polarization-matched

GaInN/AlGaInN multi-quantum-well light-emitting diodes with reduced efficiency droop', *Applied Physics Letters*, vol. 93, no. 4, pp. 041102–041102–3, Jul. 2008.

[53] D. Zhu, M. F. Schubert, J. Cho, E. F. Schubert, M. H. Crawford, D. D. Koleske, H. Shim, and C. Sone, 'Genetic Algorithm for Innovative Device Designs in High-Efficiency III–V Nitride Light-Emitting Diodes', *Applied Physics Express*, vol. 5, no. 1, p. 012102, 2012.

[54] J. Xie, X. Ni, Q. Fan, R. Shimada, Ü. Özgür, and H. Morkoç, 'On the efficiency droop in InGaN multiple quantum well blue light emitting diodes and its reduction with p-doped quantum well barriers', *Applied Physics Letters*, vol. 93, no. 12, pp. 121107–121107–3, Sep. 2008.

[55] L. Zhang, X. C. Wei, N. X. Liu, H. X. Lu, J. P. Zeng, J. X. Wang, Y. P. Zeng, and J. M. Li, 'Improvement of efficiency of GaN-based polarization-doped light-emitting diodes grown by metalorganic chemical vapor deposition', *Applied Physics Letters*, vol. 98, no. 24, pp. 241111–241111–3, Jun. 2011.

[56] Y. Yan Zhang and Y. An Yin, 'Performance enhancement of blue light-emitting diodes with a special designed AlGaN/GaN superlattice electron-blocking layer', *Applied Physics Letters*, vol. 99, no. 22, pp. 221103–221103–3, Nov. 2011.

[57] E. Sari, S. Nizamoglu, T. Ozel, and H. V. Demir, 'Blue quantum electroabsorption modulators based on reversed quantum confined Stark effect with blueshift', *Applied Physics Letters*, vol. 90, no. 1, pp. 011101–011101–3, Jan. 2007.

[58] A. Bhatnagar, S. Latif, C. Debaes, and D. A. B. Miller, 'Pump-probe measurements of CMOS detector rise time in the blue', *Journal of Lightwave Technology*, vol. 22, no. 9, pp. 2213 – 2217, Sep. 2004.

[59] S. Nakamura, 'The Roles of Structural Imperfections in InGaN-Based Blue Light-Emitting Diodes and Laser Diodes', *Science*, vol. 281, no. 5379, pp. 956–961, Aug. 1998.

[60] P. Gibart, ‘Metal organic vapour phase epitaxy of GaN and lateral overgrowth’, *Reports on Progress in Physics*, vol. 67, no. 5, pp. 667–715, May 2004.

[61] C. Bayram, J. L. Pau, R. McClintock, and M. Razeghi, ‘Comprehensive study of blue and green multi-quantum-well light-emitting diodes grown on conventional and lateral epitaxial overgrowth GaN’, *Applied Physics B*, vol. 95, no. 2, pp. 307–314, Nov. 2008.

[62] S. Nakamura, M. Senoh, S. Nagahama, N. Iwasa, T. Yamada, T. Matsushita, H. Kiyoku, Y. Sugimoto, T. Kozaki, H. Umemoto, M. Sano, and K. Chocho, ‘InGaN/GaN/AlGaN-based laser diodes with modulation-doped strained-layer superlattices grown on an epitaxially laterally overgrown GaN substrate’, *Applied Physics Letters*, vol. 72, no. 2, pp. 211–213, Jan. 1998.

[63] A. Usui, H. Sunakawa, A. Sakai, and A. A. Yamaguchi, ‘Thick GaN Epitaxial Growth with Low Dislocation Density by Hydride Vapor Phase Epitaxy’, *Japanese Journal of Applied Physics*, vol. 36, no. Part 2, No. 7B, pp. L899–L902, 1997.

[64] C. F. Johnston, M. A. Moram, M. J. Kappers, and C. J. Humphreys, ‘Defect reduction in (112) semipolar GaN grown on m-plane sapphire using ScN interlayers’, *Applied Physics Letters*, vol. 94, no. 16, pp. 161109–161109–3, Apr. 2009.

[65] B. M. Imer, F. Wu, S. P. DenBaars, and J. S. Speck, ‘Improved quality (110) a-plane GaN with sidewall lateral epitaxial overgrowth’, *Applied Physics Letters*, vol. 88, no. 6, pp. 061908–061908–3, Feb. 2006.

[66] C.-Y. Huang, H.-M. Ku, C.-Z. Liao, and S. Chao, ‘MQWs InGaN/GaN LED with embedded micro-mirror array in the epitaxial-lateral-overgrowth gallium nitride for light extraction enhancement’, *Opt. Express*, vol. 18, no. 10, pp. 10674–10684, May 2010.

[67] H. V. Demir, V. A. Sabnis, O. Fidaner, J.-F. Zheng, J. Harris, J.S., and D. A. B. Miller, ‘Multifunctional integrated photonic switches’, *IEEE Journal of Selected Topics in Quantum Electronics*, vol. 11, no. 1, pp. 86 – 96, Feb. 2005.

[68] T. Ozel, E. Sari, S. Nizamoglu, and H. V. Demir, ‘Violet to deep-ultraviolet InGaN/GaN and GaN/AlGaN quantum structures for UV electroabsorption modulators’, *Journal of Applied Physics*, vol. 102, no. 11, pp. 113101–113101–5, Dec. 2007.

[69] Z. Xu, H. Ding, B. M. Sadler, and G. Chen, ‘Analytical performance study of solar blind non-line-of-sight ultraviolet short-range communication links’, *Optics Letters*, vol. 33, no. 16, p. 1860, Aug. 2008.

[70] E. Sari, L. W. Jang, J. H. Baek, I.-H. Lee, X. W. Sun, and H. V. Demir, ‘Dislocation density dependent electroabsorption in epitaxial lateral overgrown InGaN/GaN quantum structures’, *Opt. Express, in press*, 2012.

[71] I.-L. Lu, Y.-R. Wu, and J. Singh, ‘A study of the role of dislocation density, indium composition on the radiative efficiency in InGaN/GaN polar and nonpolar light-emitting diodes using drift-diffusion coupled with a Monte Carlo method’, *Journal of Applied Physics*, vol. 108, no. 12, pp. 124508–124508–6, Dec. 2010.

[72] M. F. Schubert, S. Chhajed, J. K. Kim, E. F. Schubert, D. D. Koleske, M. H. Crawford, S. R. Lee, A. J. Fischer, G. Thaler, and M. A. Banas, ‘Effect of dislocation density on efficiency droop in GaInN/GaN light-emitting diodes’, *Applied Physics Letters*, vol. 91, no. 23, pp. 231114–231114–3, Dec. 2007.

[73] E. Sari, S. Nizamoglu, I.-H. Lee, J.-H. Baek, and H. V. Demir, ‘Electric field dependent radiative decay kinetics of polar InGaN/GaN quantum heterostructures at low fields’, *Applied Physics Letters*, vol. 94, no. 21, pp. 211107–211107–3, May 2009.

[74] S.-J. Tu, J.-K. Sheu, M.-L. Lee, C.-C. Yang, K.-H. Chang, Y.-H. Yeh, F.-W. Huang, and W.-C. Lai, ‘Enhanced output power of GaN-based LEDs with embedded AlGaN pyramidal shells’, *Opt. Express*, vol. 19, no. 13, pp. 12719–12726, Haziran 2011.

[75] L.-Y. Chen, H.-H. Huang, C.-H. Chang, Y.-Y. Huang, Y.-R. Wu, and J. Huang, ‘Investigation of the strain induced optical transition energy shift of

the GaN nanorod light emitting diode arrays', *Opt Express*, vol. 19 Suppl 4, pp. A900–907, Jul. 2011.

[76] K. Okamoto, J. Kashiwagi, T. Tanaka, and M. Kubota, 'Nonpolar m-plane InGaN multiple quantum well laser diodes with a lasing wavelength of 499.8 nm', *Applied Physics Letters*, vol. 94, no. 7, p. 071105, 2009.

[77] K. M. Kelchner, Y.-D. Lin, M. T. Hardy, C. Y. Huang, P. S. Hsu, R. M. Farrell, D. A. Haeger, H. C. Kuo, F. Wu, K. Fujito, D. A. Cohen, A. Chakraborty, H. Ohta, J. S. Speck, S. Nakamura, and S. P. DenBaars, 'Nonpolar AlGaN-Cladding-Free Blue Laser Diodes with InGaN Waveguiding', *Applied Physics Express*, vol. 2, no. 7, p. 071003, 2009.

[78] R. M. Farrell, P. S. Hsu, D. A. Haeger, K. Fujito, S. P. Denbaars, J. S. Speck, and S. Nakamura, 'Low-threshold-current-density AlGaN-cladding-free m-plane InGaN/GaN laser diodes', *Applied Physics Letters*, vol. 96, p. 1113, Jun. 2010.

[79] E. Sari, S. Nizamoglu, J.-H. Choi, S.-J. Lee, K.-H. Baik, I.-H. Lee, J.-H. Baek, S.-M. Hwang, and H. V. Demir, 'Opposite carrier dynamics and optical absorption characteristics under external electric field in nonpolar vs. polar InGaN/GaN based quantum heterostructures', *Opt. Express*, vol. 19, no. 6, pp. 5442–5450, Mar. 2011.

[80] Y. D. Jho, J. S. Yahng, E. Oh, and D. S. Kim, 'Field-dependent carrier decay dynamics in strained In_{x}Ga_{1-x}N/GaN quantum wells', *Phys. Rev. B*, vol. 66, no. 3, p. 035334, Jul. 2002.

[81] G. A. Garrett, H. Shen, M. Wraback, A. Tyagi, M. C. Schmidt, J. S. Speck, S. P. DenBaars, and S. Nakamaura, 'Comparison of time-resolved photoluminescence from InGaN single quantum wells grown on nonpolar and semipolar bulk GaN substrates', *physica status solidi (c)*, vol. 6, no. S2, pp. S800–S803, 2009.

[82] M. Häberlen, T. J. Badcock, M. A. Moram, J. L. Hollander, M. J. Kappers, P. Dawson, C. J. Humphreys, and R. A. Oliver, 'Low temperature photoluminescence and cathodoluminescence studies of nonpolar GaN

grown using epitaxial lateral overgrowth', *Journal of Applied Physics*, vol. 108, no. 3, pp. 033523–033523–7, Aug. 2010.

[83] E. Lioudakis, A. Othonos, E. Dimakis, E. Iliopoulos, and A. Georgakilas, 'Ultrafast carrier dynamics in InxGa1−xN (0001) epilayers: Effects of high fluence excitation', *Applied Physics Letters*, vol. 88, no. 12, pp. 121128–121128–3, Mar. 2006.

[84] Y.-L. Li, Y.-R. Huang, and Y.-H. Lai, 'Efficiency droop behaviors of InGaN/GaN multiple-quantum-well light-emitting diodes with varying quantum well thickness', *Applied Physics Letters*, vol. 91, no. 18, pp. 181113–181113–3, Oct. 2007.

[85] S. Choi, H. J. Kim, S.-S. Kim, J. Liu, J. Kim, J.-H. Ryou, R. D. Dupuis, A. M. Fischer, and F. A. Ponce, 'Improvement of peak quantum efficiency and efficiency droop in III-nitride visible light-emitting diodes with an InAlN electron-blocking layer', *Applied Physics Letters*, vol. 96, no. 22, pp. 221105–221105–3, Jun. 2010.

[86] C. H. Wang, C. C. Ke, C. Y. Lee, S. P. Chang, W. T. Chang, J. C. Li, Z. Y. Li, H. C. Yang, H. C. Kuo, T. C. Lu, and S. C. Wang, 'Hole injection and efficiency droop improvement in InGaN/GaN light-emitting diodes by band-engineered electron blocking layer', *Applied Physics Letters*, vol. 97, no. 26, p. 261103, 2010.

[87] L. Zhang, K. Ding, N. X. Liu, T. B. Wei, X. L. Ji, P. Ma, J. C. Yan, J. X. Wang, Y. P. Zeng, and J. M. Li, 'Theoretical study of polarization-doped GaN-based light-emitting diodes', *Applied Physics Letters*, vol. 98, no. 10, pp. 101110–101110–3, Mar. 2011.

[88] Y.-Y. Zhang, G.-H. Fan, and T. Zhang, 'Performance Enhancement of Blue Light-Emitting Diodes Without an Electron-Blocking Layer by Using p-Type Doped Barriers and a Hole-Blocking Layer of Low Al Mole Fraction', *IEEE Journal of Quantum Electronics*, vol. 48, no. 2, pp. 169 – 174, Feb. 2012.